UC San Diego

UC San Diego Electronic Theses and Dissertations

Title

Multiscale Dynamics of Wind-Driven Motions in the Ocean: From Near-Inertial Oscillations to Turbulence

Permalink

https://escholarship.org/uc/item/06c8r09k

ISBN

9798171606794

Author

Bergentz, Kerstin

Publication Date

2026-10-19

Peer reviewed|Thesis/dissertation

eScholarship.org Powered by the California Digital Library
University of California

UNIVERSITY OF CALIFORNIA SAN DIEGO

Multiscale Dynamics of Wind-Driven Motions in the Ocean: From Near-Inertial Oscillations to Turbulence

A Dissertation submitted in partial satisfaction of the
requirements for the degree Doctor of Philosophy

in

Oceanography

by

Kerstin Astrid Bergentz

Committee in charge:

Jennifer MacKinnon, Co-Chair
Luca Centurioni, Co-Chair
Andrew Lucas
Pierre-Marie Poulain
Sutanu Sarkar
Harper Simmons

2026

Copyright

Kerstin Astrid Bergentz, 2026

All rights reserved.

The Dissertation of Kerstin Astrid Bergentz is approved, and it is acceptable in quality and form for publication on microfilm and electronically.

University of California San Diego

2026

DEDICATION

To my parents. For letting me test my sails and find my own way while always providing a safe harbor to return to. I could not have asked for anything more than getting to be your daughter. Älskar er mest.

EPIGRAPH

If we knew what we were doing,
it wouldn't be called research, would it?

Albert Einstein

One's destination is not a place,
but a new way of seeing things.

Henry Miller

Man har inte roligare än man gör sig.

Mom

TABLE OF CONTENTS

Dissertation Approval Page iii

Dedication iv

Epigraph v

Table of Contents vi

List of Figures viii

List of Tables x

Acknowledgements xi

Vita xiv

Abstract of the Dissertation xv

Introduction 1

Chapter 1 Fast Times at Lofoten High – Interactions Between Near-Inertial Oscillations and a Strong Mesoscale Eddy 5
1.1 Introduction 6
1.2 Sampling region and data collection 10
1.2.1 The Lofoten Basin Eddy 10
1.2.2 Surface drifters 11
1.2.3 Auxilliary data 11
1.3 Methods 12
1.3.1 Data processing and inertial filtering 12
1.3.2 Multivariate Wavelet Ridge Analysis 14
1.3.3 Kinematics from Lagrangian assets 14
1.3.4 Slab models 15
1.3.5 Cyclogeostrophy 20
1.4 Results 21
1.4.1 Wind forcing 21
1.4.2 Kinematic properties of the LBE 21
1.4.3 Near-inertial energy patterns 24
1.5 Discussion 26
1.5.1 Cyclogeostrophy 26
1.5.2 Slab model output and wind work 29
1.5.3 Eddy-NIO pumping: a forced damped oscillator 32
1.5.4 Limitations and speculations 38
1.6 Conclusion 43

Chapter 2 Sub-Inertial Trapping and Sub-Eddy Vorticity in an Anticyclone: A Multi-Method Drifter-Based Analysis of the Lofoten Basin Eddy 49
2.1 Introduction 50
2.2 Data 52
2.2.1 Surface drifters 52
2.2.2 Auxiliary data 54
2.3 Methods 54
2.3.1 Kinematics from Lagrangian drifter triplets 54
2.3.2 Decomposition of drifter trajectories using a gridded stream function 56
2.3.3 Gaussian Process Regression 59
2.4 Results 62
2.4.1 Forcing and energy patterns 62
2.4.2 Triplet statistics 62
2.4.3 Decomposition and instantaneous frequency 64
2.4.4 Gaussian Process Regression 67
2.5 Discussion 69
2.5.1 Fine-scale vorticity structures 69
2.5.2 Near-inertial trapping 71
2.5.3 Patterns of near-inertial kinetic energy 74
2.5.4 Limitations and future work 76
2.6 Conclusion 77
2.7 Appendix A: Choice of decomposition model 78
2.8 Appendix B: Gaussian Process Regression evaluation 79
2.9 Appendix C: Choice of wavelet center frequency 81

Chapter 3 Stratified and stormy in the Bay of Bengal - internal waves and turbulence before and after cyclone Remal 85
3.1 Introduction 86
3.2 Methods 89
3.2.1 Instruments and data 89
3.2.2 WKB scaling and spectral decomposition 92
3.2.3 Wave characteristics and ray tracing 94
3.2.4 Microstructure data analysis and stratification relative coordinates 95
3.3 Results 99
3.3.1 Internal waves and ray tracing 99
3.3.2 Turbulence environment and mixing efficiency 101
3.4 Discussion 106
3.4.1 The origin of internal waves in the Bay of Bengal 107
3.4.2 Dissipation environment before and after Remal 109
3.5 Conclusion 112

Bibliography 116

LIST OF FIGURES

Figure 1.1. Map of the Lofoten Basin and Jan Mayen 9

Figure 1.2. Multi Wavelet Ridge Analysis spectrogram of MiniMet wind and drifter velocity 13

Figure 1.3. Inertial kinetic energy, wind speed, vorticity and distance from eddy center 22

Figure 1.4. Radially binned root mean square azimuthal and inertial velocities and terms in the cyclogeostrophic balance 24

Figure 1.5. Time series of cyclogeostrophic terms for each drifter pair 27

Figure 1.6. Slab model outputs for event one and two 30

Figure 1.7. Energy tendency of the system 32

Figure 1.8. Energy center movement and energy transfer 39

Figure 1.9. Satellite altimetry comparisons 41

Figure 1.10. Identification of boost factors applied to altimetry 45

Figure 1.11. Eddy center variability 48

Figure 2.1. Map overview of drifter tracks and eddy center location 2022 53

Figure 2.2. Kinematics in the LBE estimated by drifter triplets 63

Figure 2.3. Gridded stream function decomposition using the drifter array 65

Figure 2.4. Instantaneous frequency from drifters and submesoscale decomposition . . 66

Figure 2.5. Gaussian Process Regression 68

Figure 2.6. Comparison of three methods 70

Figure 2.7. Statistics of sub-eddy vorticity patches 71

Figure 2.8. Gridded stream function model selection 79

Figure 2.9. verification of the Gaussian Process Regression 80

Figure 2.10. Instantaneous frequency wavelet filter description 82

Figure 3.1. Process figure for the EKAMSAT project 88

Figure 3.2. Map of the Bay of Bengal and sampling tracks 90

Figure 3.3. Wind and internal wave shear at the Seaglide rand DBASIS locations 94

Figure 3.4. Seaglider ray tracing 101

Figure 3.5. Epsilometer and shipboard ADCP section plots 103

Figure 3.6. Statistical overview of bulk properties of turbulence before and after Remal 104

Figure 3.7. Statistical overview of bulk properties of mixing efficiency before and after Remal 106

Figure 3.8. Low passed zonal and meridional Seaglider velocities 108

Figure 3.9. Raw zonal and meridional shear from the Seaglider and DBASIS 114

Figure 3.10. Frequency and wavenumber spectra from the Seaglider 115

LIST OF TABLES

Table 2.1. Mesoscale model-selection sweep under the unconstrained fit. 83

Table 2.2. Mesoscale model-selection sweep under the unconstrained fit - continued . 84

ACKNOWLEDGEMENTS

First and foremost I would like to thank my advisors Jen MacKinnon and Luca Centurioni for taking a chance on me as a novice ocean scientist you had only met as a tiny little square on Zoom during the COVID-19 pandemic. Thank you for being so generous with your time and resources and for letting me do this PhD, including my many side quests. It is a true privilege to have two advisors where the inevitable response to you telling someone who you work with is "wow, you're so lucky, they are both such wonderful people!" I could not agree more. You embody the kind of scientist I want to be: great at doing the science, but even better at being a good person. Thank you to the rest of my committee, Harper Simmons, Drew Lucas, Pierre Poulain and Sutanu Sarkar for their time and insightful conversations. A special shout out to my honorary committee member Fiamma Straneo, I think I have you to thank for getting into grad school in the first place. Another huge thank you to everyone in the the Multiscale Ocean Dynamics Lab and the Lagrangian Drifter Lab for help with instrumentation and data questions. Being at sea with many of you has been some of the best times of my grad school career.

Tuning in to remote classes from Sweden (with a 9 hour time difference) during the start of the Covid19 pandemic, and not moving to the US until halfway through my second year, was not the start to graduate school I had imagined. I owe huge thanks to many people in San Diego for making me feel so welcome once I eventually made it over here, including the rest of "the lost cohort" (PO 2020 - we can do anything!). A special shutout to Tanumoy without whom I would not have made it through the first year math classes, and with whom I've shared many long conversations about life. I am a better person for it. Thank you to Noel for both challenging and inspiring me always. I feel incredibly fortunate to have many sisters in science, including Kaylie, Eva, Oc, Ella, Aurora, Athena, Laura, Ailin, Leticia, Rebecca and Kjersti who have made everything in grad school so much better. A special thanks to Eva who has literally been there since day one doing SIO210 homework together over Zoom from our respective childhood bedrooms in Barcelona and Lund. The unwavering love and support, the pep talks, the celebrations, the adventures... I'm not kidding when I say I wouldn't be here without you.

Being the daughter, sister, cousin, niece and friend who moves 6000 miles and nine time zones away has not always been easy, and there are many people across the pond who I want to thank for keeping me sane through these past few years. To my dear friends Francesca, Ronni, Felix and Chiara, thank you for always making it feel like no time at all has passed when we meet and for reminding me of what really matters at the end of the day: love and friendship.

Thank you to my family. Words could never capture the depth of my love for you all. Thank you Mom and Dad for raising me and my siblings to know the value of love, kindness and curiosity. You inspire me every day and I hope I'm as cool as you two are in 30 years. To my brother and sister, Kalle and Matilda: getting to be your older sister is truly the greatest privilege of my life and I am so, so proud of the kind, funny, authentic and adventurous humans you have grown into, and I hope you know I'd literally do anything for you two.

Last but not least, thank you to Sho, and Umi, who stumbled into my life on the third attempt and brought so much love, adventure and joyful chaos that my world will never be the same again. You inspire me to be the best version of myself every day. Love and appreciation.

Chapter 1, in full, has been accepted for publication as it may appear in Journal of Physical Oceanography, 2026, *Fast Times at Lofoten High – Interactions Between Near-Inertial Oscillations and a Strong Mesoscale Eddy*. Bergentz, Kerstin A.; Centurioni, Luca R.; MacKinnon, Jennifer A. The dissertation author was the primary investigator and author of this paper.

Chapter 2, in part is currently being prepared for publication of the material. *Sub-Inertial Trapping and Sub-Eddy Vorticity in an Anticyclone: A Multi-Method Drifter Analysis of the Lofoten Basin Eddy*. Bergentz, Kerstin A.; Early, Jeffrey, MacKinnon, Jennifer A., Centurioni, Luca R. The dissertation author was the primary investigator and author of this material.

Chapter 3, in full, is currently being prepared for submission of the material as it may appear in Journal of Geophysical Research: Oceans, *Stratified and stormy in the Bay of Bengal - internal waves and turbulence before and after cyclone Remal*. Bergentz, Kerstin; MacKinnon, Jennifer; Lucas, Andrew J.; Rainville, Luc; Kannad, Ankitha; Pereira, Filipe; Alford, Matthew

H.; Le Boyer, Arnaud. The dissertation author was the primary investigator and author of this paper.

VITA

2017	Bachelor of Science, Chalmers University of Technology, Gothenburg, Sweden
2020	Bachelor of Science, Lund University, Lund, Sweden
2021	Master of Science, Scripps Institution of Oceanography at UC San Diego
2026	Doctor of Philosophy, Scripps Institution of Oceanography at UC San Diego

PUBLICATIONS

Bergentz, K., Centurioni, L., MacKinnon, J. 2026, Fast Times at Lofoten High – Interactions Between Near-Inertial Oscillations and a Strong Mesoscale Eddy, Journal of Physical Oceanography, **(accepted)**

Rodriguez-Marin, A., **Bergentz, K.**, Kannad, A., Bellerjeau, C., Dias Luko, C., Zhang, H., MacKinnon, J., Alford, M., Couto, N., McConnell, B., LeBoyer, A. Ocean Turbulence and Mixing Course: Student-Led Instruction and At-Sea Experimentation, Oceanography, **(in review)**

Hilditch, J. P., **Bergentz, K.**, Northcott, D., Luko, C. D., Cohanim, K., Schlichting, D., Sanchez-Rios, A., Weiss, K., Hetland, R., MacKinnon, J., Nash, J., Shearman, R.K., Thomas, L. N. (2025). Observations of subduction, downward heat flux and dense filament collapse in the northern Gulf of Mexico. Journal of Geophysical Research: Oceans, 130, e2025JC022570. https://doi.org/10.1029/2025JC022570

ABSTRACT OF THE DISSERTATION

Multiscale Dynamics of Wind-Driven Motions in the Ocean: From Near-Inertial Oscillations to Turbulence

by

Kerstin Astrid Bergentz

Doctor of Philosophy in Oceanography

University of California San Diego, 2026

Jennifer MacKinnon, Co-Chair
Luca Centurioni, Co-Chair

Wind-driven motions in the upper ocean represent one of the largest inputs of mechanical energy the ocean receives, but where that energy goes is harder to say. Some stays in the mixed layer, some radiates downward as near-inertial internal waves, and some is traded with the eddies these motions pass through. The exchanges that decide between these outcomes occur at scales smaller than most models resolve and are rarely linear, making the fate of wind-driven energy an inherently multiscale problem. This dissertation follows wind-driven energy from mixed-layer near-inertial oscillations, to the internal waves they radiate, to the turbulence that dissipates them, using observations from the North Atlantic and the Indian Ocean. Chapter 1 analyzes data from

ten Lagrangian surface drifters deployed in the Lofoten Basin Eddy (LBE), a semi-permanent Norwegian Sea anticyclone, combined with sea-surface height altimetry and reanalysis winds. A Lagrangian slab model including eddy pressure-gradient terms reproduces the observed inertial response, while a wind-forced-only model does not, showing that not all near-inertial energy near the eddy core is wind-driven. A mechanism is proposed whereby correlations between near-inertial velocities and eddy pressure gradients, modulated by a near-inertial oscillation of the eddy center, transfer energy into the inertial band. Chapter 2 resolves the sub-eddy scale in the LBE with a denser 28-drifter array deployed the following year and using three different analysis methods: drifter-triplet kinematics, a gridded stream-function decomposition, and Gaussian Process Regression reconstruction. The eddy is not a smoothly rotating axisymmetric vortex but is permeated by intense, short-lived vorticity patches with cyclonic filaments encircling the anticyclonic core. Near-inertial motions oscillate below the local inertial frequency throughout the interior, tracking the coherent, time-integrated eddy rather than instantaneous local vorticity. Chapter 3 follows the energy to dissipation using microstructure and velocity profiles collected in the Bay of Bengal before and after severe cyclonic storm Remal. Ray tracing indicates most pre-storm near-inertial packets are not wind-generated, and the storm reorganized turbulence into fewer, thinner shear-driven layers while reducing mixing efficiency, reshaping the geometry of mixing more than its magnitude.

Introduction

The ocean and atmosphere are two integral components of Earth's climate system working in tandem to regulate both global climate patterns and local weather phenomena. The interactions between them, like the exchange of heat and energy, are some of the most fundamental processes driving climate and directly influence the large and small-scale ocean circulation (e.g. Yu et al. (2018); Zippel et al. (2022); Bigg et al. (2003); Schmitt (2018)). The focus of this dissertation is on one particular aspect of this exchange, namely the input of energy from the atmosphere to the ocean through wind, and follows this wind-driven energy down the cascade: from near-inertial oscillations (NIOs) in the mixed layer, to the near-inertial internal waves (NIWs) they radiate as they propagate downward, to the centimeter-scale chaotic fluid motions we call "turbulence" that ultimately dissipates it.

Much remains to be understood about the flow of energy between the atmosphere and ocean. For example, estimates diverge substantially on the amount of work done by atmospheric winds on the ocean mixed layer inertial motions (0.3-1.3 TW) (Alford, 2020), as well as on how much of this work is transferred below the mixed layer with estimates varying from 11-30% below the mixed layer (Rimac et al., 2016; Olbers et al., 2020; Raja et al., 2022a; Von Storch and Lüschow, 2023) to 6-33% at different depths from 110-800 m (Furuichi et al., 2008; Alford et al., 2012; Cuypers et al., 2012). Part of the discrepancy can be attributed to varying temporal and lateral resolution of the wind products used Jiang et al. (2005), as well as the way the wind stress is estimated (Liu et al., 2019) or which mixed layer model is used (Alford, 2020). The inherently intermittent nature of wind forcing compounds this uncertainty: much of the near-inertial energy is delivered in short, episodic bursts by moving storm systems, with the

strongest fluxes concentrated in the 30-60° latitude storm-track bands during winter (D'Asaro, 1995; Alford, 2003; Liu et al., 2019). Quantifying not only the magnitude but the eventual fate of this energy - how much remains in the mixed layer, how much radiates out of the mixed layer as NIWs and how much is exchanged with the surrounding balanced flow - remains an open problem.

The presence of background vorticity, like mesoscale eddies, shapes the path of near-inertial energy. Internal gravity waves are confined by a dispersion relation to frequencies between the inertial or Coriolis (f) and buoyancy (N) frequencies $f^2 < \omega^2 < N^2$, where $f = 2\Omega \sin\phi$ with Ω being the rotation rate of the Earth and ϕ the latitude, and $N^2 = -(g/\rho_0)(\partial\rho/\partial z)$ with g being the local gravitational acceleration and the density $\rho_0 = 1025\text{kg/m}^3$. In the presence of background vorticity however, the lower bound shifts to an effective Coriolis frequency $f_{\text{eff}} = f + \zeta/2$ (Kunze, 1985). In anticyclonic vorticity where $\zeta < 0$ this lowers the floor of the internal wave band, trapping near-inertial energy and funneling it downward toward dissipation, making anticyclonic eddies hot spots for near-inertial energy (Kunze et al., 1995; Lee and Niiler, 1998; Yu et al., 2022; Thomas et al., 2024). In addition to this refractive rearrangement, eddies can also exchange energy with the near-inertial field directly: a laterally sheared geostrophic flow can transfer energy to or from near-inertial motions through lateral shear production (Whitt and Thomas, 2015), and a growing body of theory, models and observations shows that nonlinear eddy-wave coupling plays a leading order role in shaping the wave field (Shakespeare, 2023; Xie and Vanneste, 2015; Barkan et al., 2017; Savage et al., 2025). Yet the smaller spatial and temporal scales over which this exchange occurs, such as the sub-eddy scales where curvature, pressure gradients and filamented vorticity introduce variability in the force balance, remain poorly resolved and poorly understood.

Once injected at large scales, the energy does not remain there, instead it is redistributed across a broad range of spatial scales through a cascade of interactions that ultimately delivers a portion of it to the small scales where mixing occurs (Ferrari and Wunsch, 2009; MacKinnon et al., 2017). At this stage the energy is either lost to viscous friction and heat, or used to do

work against density gradients and irreversibly mix the water column. This diapycnal mixing is what erodes stratification and moves heat, nutrients, and carbon across density surfaces. How efficiently turbulent energy accomplishes this mixing is captured by the mixing efficiency Γ. In energetic, nearly isotropic turbulence Γ is often treated as a constant, but in strongly stratified, weakly turbulent regimes buoyancy suppresses turbulent overturns before they can fully develop, so that Γ instead depends on how energetic the turbulence is relative to the stratification it works against (Caulfield, 2021; Gregg et al., 2018; Pham et al., 2023). Because this turbulent mixing occurs at scales far below the grid of any climate model, its effect on the resolved circulation must be represented through parameterizations (MacKinnon et al., 2017). But these closures are only as reliable as the physics they encode (MacKinnon et al., 2017; Cimoli et al., 2026), and they typically assume energy input pathways - such as direct wind forcing of near-inertial waves - that observations increasingly suggest are incomplete (Waterhouse et al., 2022).

These parameterizations are capable of reproducing large-scale circulation and its leading order trends, but the residual uncertainty matters, especially as Earth's climate changes and the balance of the underlying physics might shift. Nowhere is this clearer than in regions where ocean mixing directly modulates climate: in the strongly stratified Bay of Bengal, for instance, subsurface turbulent heat flux helps set the sea surface temperatures that govern the Indian summer monsoon on which nearly two billion people depend (Shroyer et al., 2016; Cherian et al., 2020).

Reducing this uncertainty is ultimately a problem of physical understanding: parameterizations can only improve to the level of our grasp of the processes they are meant to represent, and that understanding in turn rests on observations that are able to spatially and temporally resolve where wind-driven energy is stored and transferred. The work presented here draws on Lagrangian surface drifters that move with the flow to capture energy exchange at eddy and sub-eddy scales, and on microstructure profiling that reaches the centimeter scales at which that energy is finally dissipated. Across three chapters, these observations are used to examine how wind-driven energy is organized, exchanged, and ultimately dissipated as it moves through the

ocean.

Chapter 1 uses an array of Lagrangian surface drifters deployed in the Lofoten Basin Eddy, a semi-permanent anticyclone in the Norwegian Sea, to examine how near-inertial oscillations interact with a strong mesoscale eddy. A Lagrangian slab model that includes the eddy's sea-surface height pressure gradients reproduces the observed wind work where a wind-forced only model fails, revealing that not all near-inertial energy near the eddy core is wind-driven. We also propose a new mechanism whereby correlations between near-inertial motions and eddy pressure gradients can transfer energy into the inertial band.

Chapter 2 zooms into the sub-eddy scale, using a denser 28-drifter array deployed in the same eddy the subsequent year and applies three complementary methods: drifter-triplet kinematics, a gridded stream function decomposition and a Gaussian Process Regression. Together they reveal that the eddy interior is far from a smoothly rotating axisymmetric vortex, hinting at a filamented fine-scale vorticity structure and its imprint on the organization of near-inertial kinetic energy.

Chapter 3 follows the energy to its dissipative end, using microstructure and velocity observations from the Bay of Bengal before and after cyclone Remal. It shows the presence of a rich internal wave field that most likely stems from mesoscale and submesoscale flows rather than wind forcing, and that the storm reorganized the turbulence into fewer, thinner, shear-driven layers reshaping the geometry of mixing in addition to its magnitude.

Chapter 1

Fast Times at Lofoten High – Interactions Between Near-Inertial Oscillations and a Strong Mesoscale Eddy

1.1 Introduction

Surface-generated near-inertial oscillations (NIOs) are often observed as the ocean's local response to forcing from wind. They owe their existence to Earth rotating around its own axis, and their frequency is determined by the local Coriolis (inertial) frequency (Plueddemann and Farrar, 2006; Alford et al., 2016). Part of the energy in inertial motions can be transmitted to downward-propagating near-inertial internal waves (NIWs) through repeated convergence and divergence at the surface (Thomas and Zhai, 2021). Downward-propagating NIWs are associated with strong vertical shear, which is why they are thought to make a significant contribution to ocean mixing via shear instabilities (Alford et al., 2016; Whalen et al., 2018) and climate models have been shown to be quite sensitive to this near-inertial internal wave-driven mixing (Jochum et al., 2013; MacKinnon et al., 2017). Internal gravity waves are governed by a dispersion relation that limits their frequency between the inertial (f) and buoyancy (N) frequencies, such that $f^2 < \omega^2 < N^2$. In the presence of background vorticity the inertial frequency $f = 2\Omega \sin\phi$ shifts to the effective inertial frequency $f_{\text{eff}} = f + \zeta/2$ where Ω is the rotation rate of the Earth, ϕ is the latitude and $\zeta = \partial v/\partial x - \partial u/\partial y$ is the relative vorticity of the mesoscale field (Kunze, 1985). Hence NIWs excited in a region of anticyclonic (negative) relative vorticity can have frequencies below f, trapping them and funneling them downwards towards dissipation (Kunze et al., 1995; Lee and Niiler, 1998; Yu et al., 2022).

Quantifying the net energy input to the ocean from wind via NIOs has been the focus of much research to date (e.g. Ferrari and Wunsch, 2009; Rimac et al., 2013; Watanabe and Hibiya, 2002). The total amount of near-inertial wind work globally is generally reported to be in the range of 0.3 to 1.5 TW (1 TW = 10^{12}W), the spread being mainly attributable to the different wind stress products used and differences in assumptions about how much near-inertial energy escapes the mixed layer (Rimac et al., 2013; Alford, 2020). Most of the inertial wind work on the ocean is thought to be a result of the time-varying wind stress associated with moving storm systems (D'Asaro, 1985; Alford, 2003), with the strongest energy flux occurring in the 30–60°

latitude band during the winter season (Liu et al., 2019).

The storm track latitudes are also home to strong mesoscale eddy activity. Wind-generated NIOs and NIWs are known to interact with mesoscale eddy shear, strain and vorticity in a wide variety of ways. It has been known for many decades that the presence of a mesoscale vorticity field can distort near-surface NIOs through changes in their frequency, polarization, and trajectories (Weller, 1982), despite the fact that the initial horizontal scales of NIOs at the surface generated by atmospheric forcing are typically much larger than the scales of mesoscale eddies. Subsequent theoretical and numerical studies have developed a variety of frameworks to showcase how the presence of mesoscale strain and vorticity can impose a characteristic lateral (horizontal) length scale on near-inertial motions, thereby influencing both their generation and their vertical propagation into the ocean interior (Young and Jelloul, 1997; Klein et al., 2004; Asselin and Young, 2020; Raja et al., 2022b). Such scale modification is observed in both satellite (Elipot et al., 2010) and in situ (Thomas et al., 2020) data.

In addition to refraction and related linear processes that rearrange the near-inertial wave field without directly transferring energy, there are also a host of ways that nonlinear energy exchange between the mesoscale eddy field and NIW can play leading-order role in shaping the near-inertial wave field (Xie and Vanneste, 2015; Barkan et al., 2017; Whalen et al., 2018; Barkan et al., 2024; Savage et al., 2025). For example, Whitt and Thomas (2015) consider the wind-generation process in the context of a simple laterally sheared geostrophic flow and find that there can be a net transfer of energy between the geostrophic and near-inertial motions through a lateral shear production term. Despite the fact that in the upper ocean NIWs account for roughly half of the total energy contained in the internal wave spectra (Ferrari and Wunsch, 2009), it remains unclear whether this energy input arises directly from atmospheric forcing alone, or whether energy exchange with balanced, geostrophic motions such as mesoscale eddies represents a comparably important contribution to the near-inertial energy budget. Curiously, Waterhouse et al. (2022) find that even in the upper ocean (above 600 meters) approximately 40% of near-inertial shear has up-going energy, inconsistent with direct surface generation.

Significant questions remain regarding the generation and evolution of NIOs in the upper ocean. In particular, little is known about the smaller spatial and temporal scales over which energy exchange occurs in mesoscale eddies where curvature, pressure gradients and vorticity can introduce spatial variability in the force balance. Although recent studies have begun to quantify energy transfer between mesoscale eddies and near-inertial motions, see for example (Zhang et al., 2025; Savage et al., 2025), the detailed mechanisms and scale dependence of these interactions and sub-eddy scales remain poorly understood.

Surface drifters provide a uniquely Lagrangian view of near-inertial oscillations and offer sufficient temporal and spatial resolution to resolve the small-scale variability experienced by water parcels as they move through mesoscale flow fields (Tarry et al., 2022). During the Office of Naval Research NORSE (Northern Ocean Rapid Surface Evolution) project field campaigns in 2021-2023 multiple sets of drifters were deployed in a small but energetic mesoscale anticyclonic eddy in the North Atlantic. In this paper we argue that the data from the 2021 drifter array reveal interactions between NIOs and the surrounding vorticity and pressure-gradient field that pump energy into NIOs.

At high latitudes ($\sim$70° N) the distinction between mesoscale variability - generally characterized by horizontal scales of $\mathcal{O}$ 10–100 km and temporal scales of days to months - and submesoscale variability - typically associated with horizontal scales of $\mathcal{O}$ 0.1–10 km and temporal scales of hours to days - is less clear-cut than at lower latitudes. This reduced scale separation arises from the large Coriolis parameter and relatively weak stratification, which shift mesoscale features to smaller horizontal scales and reduce the scale separation between regimes. In this context, the eddy itself has a characteristic mesoscale radius of 20 km, while the variability experienced along drifter trajectories occurs on sub-eddy scales (by definition submesoscale) of order 1–10 km. The order one Rossby number shown below also puts the eddy dynamically somewhat in between mesoscale and submesoscale regimes. We emphasize that these scales need not imply a separate submesoscale dynamical regime, but they do reflect the spatial scales over which inertial motions displace parcels within the pressure field of the eddy.

This paper is structured as follows: in section 1.2 we present the sampling region and data collected and in section 1.3 we introduce the methods used in the analysis, including a Lagrangian slab model. Results are presented in section 1.4 and discussed in section 1.5. Section 1.6 summarizes the conclusions.

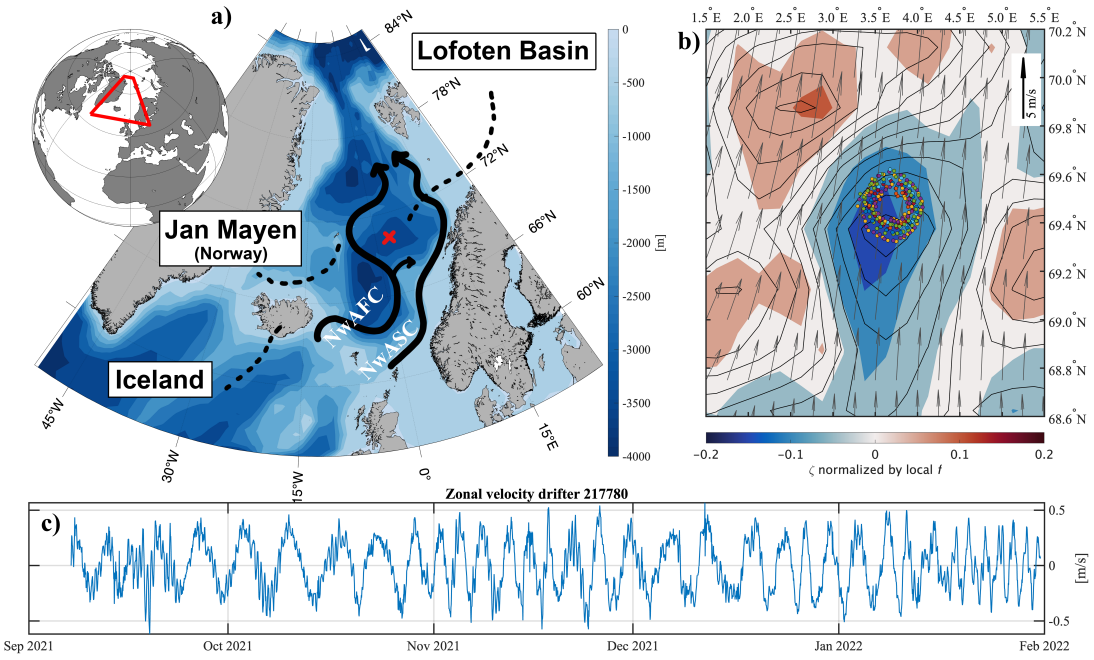


Figure 1.1. a) Map of the Lofoten Basin and Jan Mayen with color-coded bathymetry and directions of the regional currents surrounding it, the Norwegian Atlantic Front Current (NwAFC) and Norwegian Atlantic Slope Current (NwASC). The average location of the Lofoten Basin Eddy is marked with a red x. b) Drifter locations the first 48 hours of deployment. Background colors show the mean geostrophic vertical vorticity and contour lines show the mean sea surface height, both derived from satellite altimetry, averaged over the first 48 hours of deployment September 4th 09:00 to September 6th 09:00 2021. Arrows show the mean ERA5 reanalysis winds averaged over the same time period. c) Time series of zonal velocity of one drifter in the array.

1.2 Sampling region and data collection

1.2.1 The Lofoten Basin Eddy

The Lofoten Basin is a dynamic region of the Nordic Seas with a maximum depth of 3200 m, known for large variability of mesoscale vorticity and temperature variations (spatial and temporal) associated with the advection and stirring of contrasting Atlantic and Arctic water masses. The Lofoten Basin Eddy (LBE, also known as "The Lofoten Vortex") is a semipermanent anticyclonic eddy found at about 70° N and 3° E, see Figure 1.1a. It was first discovered in Russian oceanographic surveys in the 1970s and 1980s (Volkov et al., 2015). Since then, the eddy has been extensively studied with both satellite altimetry, models, and subsurface in-situ measurements (e.g Köhl, 2007; Søiland and Rossby, 2013; Bashmachnikov et al., 2017).

The LBE is typically taken to have a radius of 20-25 km (30-35 km in altimetry) with maximum speeds on the order of 80 cm/s at 950 m and a subsurface vorticity of -0.5f, reaching -0.7f at 6 km radius and 840 m depth (Fer et al., 2018). Some studies report a smaller radius of 18 ± 4 km, a maximum azimuthal velocity of 0.5–0.7 m/s at depths between 700 and 900 m, and relative vorticity close to negative local f, with a Rossby number varying between -0.4 and -0.8. According to Yu et al. (2017), geostrophy, on average, contributes 44% to the cyclogeostrophic balance, supporting the idea that LBE is non-linear.

To survive as a semipermanent eddy structure, the LBE is regenerated through both wintertime convection and vortex merging, where the latter is believed to be more important (Trodahl et al., 2020). Merger events are thought to happen about 1-4 times per year (Bosse et al., 2019). The bowl-shaped topography of the Lofoten Basin helps confine circulation and enhances vorticity retention resulting in a rich eddy field, which provides the opportunity for mergers (De Marez et al., 2021). The eddy has also been observed to move cyclonically around the basin due to topographic β-effects with the continental shelf on the east acting as the main steering feature (Trodahl et al., 2020).

1.2.2 Surface drifters

During the NORSE pilot cruise at the beginning of September 2021, a square grid 10-piece surface drifter array was deployed slightly off-center in the LBE. Figure 1.1b shows the first 48 h of drifting, and Figure 1.2d show about 35 days of drift tracks. The array consisted of 9 Surface Velocity Program (SVP) drifters and one MiniMet drifter (Centurioni, 2018), all drogued at 15 m and made by the Lagrangian Drifter Lab at Scripps Institution of Oceanography. SVP drifters record their position with an accuracy of about 2.5 m root mean squared (RMS) and measure sea surface temperature with an accuracy of ±0.05 K. MiniMet drifters, in addition, measure sea level pressure (±0.4 hPa RMS accuracy) and are equipped with Gill sonic anemometers that measure wind speeds up to 60 m/s with a 2% accuracy FS at about 30 cm above the surface. The wind direction is measured with an internal compass and has a direction accuracy of ±2.5° after calibration. SVP drifters fitted with drogues centered at 15 m depth are designed to minimize slippage by wind and waves acting on the surface buoy. Studies have shown that the drifter wind slippage in surface winds of up to 10 m/s is on the order of 1 cm/s or less (Niiler et al., 1995). During the first month of deployment the near-surface wind velocity as measured by the MiniMet only consistently exceeds 10 m/s for 24 h during a storm, as discussed in section 1.4.1, and thus we believe slippage effects to be minimal.

All 10 drifters stayed in the eddy for a minimum of two weeks, 6 drifters stayed for at least a month, and one drifter was still in the eddy almost 5 months after deployment (see Figure 1.1c), suggesting that the LBE was relatively stable during the experiment.

1.2.3 Auxilliary data

Satellite altimetry and reanalysis winds were used to augment the analysis and interpretation of the drifter data. The altimetry data provided by the Copernicus Marine Environment Monitoring Service (CMEMS) is an L4 global product of once-daily observations estimated by optimal interpolation (merging multiple altimeter missions) and gridded to $0.25° \times 0.25°$ (Service,

2024). At latitude 70° N that is equivalent to roughly 9 km × 27 km. We have used absolute dynamic topography (ADT, sea surface height relative the geoid) for our computations. The wind reanalysis product of zonal and meridional winds at 10 m, ERA5 (Copernicus Climate Change Service, Climate Data Store, 2023), is provided by the European Centre for Medium-Range Weather Forecasts (ECMWF) and is also on a 0.25° × 0.25° grid but with an hourly resolution (Hersbach et al., 2025).

1.3 Methods

1.3.1 Data processing and inertial filtering

The SVP and MiniMet drifter GPS and wind data were subsampled from 30 min to 1 h and velocities were calculated as centered differences. Spurious drifter GPS fixes were removed through visual inspection and linearly interpolated over. At latitude 70° N the period of the semidiurnal tide, 12.42 hours, is very close to that of the local inertial frequency f, 12.81 hours. Thus, when bandpassing the drifter velocities it is difficult to separate the tidal and the near-inertial signals. However, barotropic numerical simulations indicate that tidal currents in the Lofoten Basin are negligible (on the order of 1-2 cm/s compared to geostrophic velocities of 40 cm/s (Padman and Erofeeva, 2004)). Similarly baroclinic tides in the area have been estimated to be on the order of 4-5 cm/s (Poulain and Centurioni, 2015), thus we choose to ignore the contribution of tides in our analysis, however the potential for tidal aliasing is further commented on in section 1.5.4. The inertial bandpassing was carried out with a Bartlett window of width 0.6-1.4f at latitude 69.6° N, the average latitude of the LBE center. The width was chosen based on spectral analysis to capture the full range of near-inertial motions. We also use a low pass filter with a cutoff of $f/4$, where f is the Coriolis frequency at the average latitude of the LBE center of 69.5° N, to identify the low-frequency signal in the drifter motion that is associated with the eddy. This low passed time series is used to estimate the vorticity of the eddy using methods described in section 1.3.3.

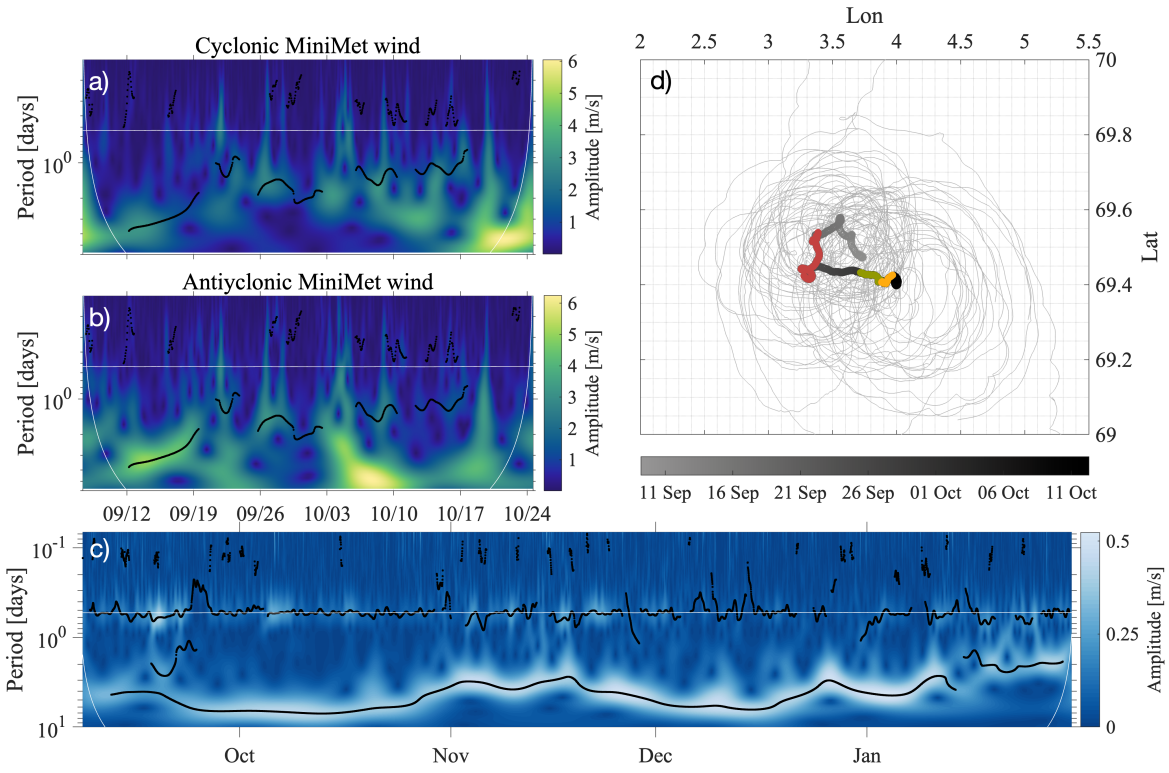


Figure 1.2. a-b) MWRA spectrogram of the MiniMet wind, and c) the anticyclonic velocities of drifter 66217780. Overlaid black lines are the output of the MWRA analysis to identify ridge points in the velocity time series and white line is the local Coriolis frequency f. d) Location of eddy center in time based on MWRA of all drifters over 35 days of drifter tracks which are shown in grey. The colored sections of the eddy center track correspond to the kinetic energy events described in section 1.4.

1.3.2 Multivariate Wavelet Ridge Analysis

The drifter data was analyzed using a multivariate wavelet ridge analysis (MWRA) script that is part of jLab (Lilly, 2021). MWRA is based on identifying loops in the tracks of Lagrangian particles, to infer if/when the particles are inside coherent vortices. If a drifter makes loops following the circular currents of an eddy, that is visible as an oscillating signal in the time series of both its location and velocity. Performing a wavelet transformation on the time series of the particle, the jLab MWRA routine picks up on so-called "ridge points", which, simplified, are maxima in the wavelet spectrogram where the wavelet of the time series aligns well with a model wavelet (the default is a Morse family wavelet). Persistent oscillations in the time series will result in a string of adjacent points that connect to a ridge, indicating that the Lagrangian particle is looping inside a vortex. In addition to the wavelet transformation providing information about the location of the ridge (vortex) in frequency space, where the drifters are in physical space at the time of the identified ridges can be used to infer the eddy center location. For a more thorough description of the jLab MWRA routine see Lilly and Olhede (2009), (2012) and Lilly and Pérez-Brunius (2021). For an example of wavelet analysis used on drifters in a Mediterranean eddy, see Poulain et al. (2023). In this work, MWRA was used to confirm if a drifter had left the LBE (see Figure 1.2c for the MWRA analysis of the drifter shown in Figure 1.1c) and to identify the eddy center (see further discussion in Appendix 1.6). Figure 1.2d shows the movement of the eddy center and drifter tracks for the first month of deployment. We also performed MWRA on the in situ wind measured by the MiniMet to rule out persistent oscillatory wind forcing, Figure 1.2a and b.

1.3.3 Kinematics from Lagrangian assets

Clusters of a minimum of three drifters can be used to estimate properties such as vorticity and strain rates in eddies (Molinari and Kirwan, 1975; Essink et al., 2022; Zeiden et al., 2022). Essink et al. (2022) evaluated three different methods to estimate kinematic properties from

clustered surface drifters and the findings suggest that a least-squares (LS) method, using a minimum of three, optimally six, drifters in a cluster, as proposed by Molinari and Kirwan (1975) and Okubo and Ebbesmeyer (1976), provides the most robust results. Here we have followed the process outlined in Molinari and Kirwan (1975) to estimate the vorticity of the LBE using a cluster of drifters. Attention needs to be paid to the length scales of the cluster relative to the scales of the flow, as well as the cluster shape. Kinematic properties can only be estimated accurately if the clusters have length scales that are smaller or approximately equal to the scale of the flow. The aspect ratio of the cluster also affects the accuracy of the velocity gradient estimates, though this effect is secondary to cluster size, which more directly controls whether the linearity assumption remains valid over the cluster domain. If the cluster is elongated perpendicular to the velocity gradient the computations of gradients become unreliable, however, the relative orientation between the main axis of the cluster and the background flow can be difficult to determine in observations due to inaccuracy in positioning, interpolation and error propagation during the calculations (Essink et al., 2022). Here we are using either the full drifter array as one cluster, or non-collinear drifter triplets as described in Berta et al. (2020) or Esposito et al. (2021) to estimate the vorticity of the LBE using the drifter locations and low passed drifter velocities. When a drifter exits the eddy (determined by visual inspection of drifter tracks and MWRA outputs) it is excluded from the computation.

1.3.4 Slab models

A slab model of the surface mixed layer of the ocean can be used to estimate the energy input into the ocean from the wind, and can be implemented in coupled ocean-atmosphere models as a low computational power option to a dynamical ocean model (Dommenget, 2010; Wang et al., 2023). A slab model is essentially a zero-dimensional model of the medium (e.g., ocean or atmosphere) where the properties at each point in space are computed and predicted, with the assumption of zero interaction between neighboring points, and where properties such as heat and momentum are immediately distributed in depth over the mixed layer. Originally proposed

by Pollard and Millard (1970) as a way to investigate the ocean's inertial response to wind stress, the typical ocean surface mixed layer slab model is constructed as a set of ordinary differential equations (ODEs) taking in wind stress, the mixed layer depth and an empirical damping constant, and outputting the near-inertial currents. Despite its limitations, it has become a standard tool for examining energy input into the ocean from wind (D'Asaro, 1985; Plueddemann and Farrar, 2006; Alford, 2001). Treating the mixed layer as a homogeneous slab through which momentum and other properties are assumed to be distributed instantaneously is of course a striking simplification, and yet, for deep enough mixed layers, this simple model captures the near-inertial response comparably to more comprehensive models that include shear, turbulent motions and a changing mixed layer depth (Alford, 2020; Flexas et al., 2019).

Crucially for our work, the typical use and interpretation of slab models is in an *Eulerian* reference frame, at a single point in space, forced by wind stress at that location. Surface drifters provide a direct *Lagrangian* measurement of the acceleration. We thus use a Lagrangian slab model formulated with the Lagrangian equations of motion for water parcels moving in a slab mixed layer (D'Asaro, 1995). We decompose the total mixed-layer velocity into a slowly varying mesoscale eddy component (u_e, v_e) and a near-inertial component (u_i, v_i), such that $U = u_e + u_i$ and $V = v_e + v_i$:

$$\begin{aligned} \frac{DU}{Dt} &= fV + \frac{\tau_x}{\rho_0 H} - g\eta_x - r_M u_e - r_I u_i \\ \frac{DV}{Dt} &= -fU + \frac{\tau_y}{\rho_0 H} - g\eta_y - r_M v_e - r_I v_i \end{aligned} \tag{1.1}$$

where $\tau = (\tau_x, \tau_y)$ is the wind stress, H is the mixed layer depth, and f is the local Coriolis parameter. Here, $\eta_x \equiv \partial\eta/\partial x$ and $\eta_y \equiv \partial\eta/\partial y$ are the zonal and meridional sea surface height gradients, respectively, such that $P_x/\rho_0 = g\eta_x$ and $P_y/\rho_0 = g\eta_y$. f is the Coriolis parameter, as defined above, for latitude 69.5° N. Throughout the rest of this work we adopt an f-plane approximation and take f to be constant since the change in f between 69° N and 70° N

(the full span of the southernmost to northernmost drifter observations used here) is less than 1%. r_I is the damping coefficient for near-inertial motions, representing energy loss primarily through downward radiation of near-inertial waves into the thermocline, and r_M is a separate damping coefficient for the slowly varying eddy flow, representing viscous and frictional decay. As long as these two damping contributions enter linearly and additively, which is satisfied by construction, the slowly varying eddy velocity (u_e, v_e) does not project onto the near-inertial band and therefore does not influence the near-inertial energy budget (equation 1.3), regardless of the value of r_M. In the numerical implementation we therefore set $r_I = r$, estimated empirically from the e-folding decay timescale of the inertially band-passed drifter velocities ($r = 0.11f$), and neglect the contribution of r_M to the near-inertial energy tendency.

Here the left-hand size material derivatives ($D\phi/Dt = d\phi/dt + \vec{u} \cdot \nabla\phi$ where ϕ is any vector or scalar field) are the acceleration directly measured by the drifters. The right hand side (rhs) includes the usual Coriolis, wind stress and linear damping terms, but also a pressure gradient term. With linearized Eulerian slab models, velocity can be linearly decomposed into geostrophic and non-geostrophic components; hence the pressure terms can be removed from the rhs if one is interested in looking at the evolution of the near-inertial motions only. However in a Lagrangian slab model, all rhs terms must be evaluated at the location of the drifter, so there is at least the potential that the time-evolving pressure term (evaluated as the drifter moves around an eddy) could have a component that projects onto the inertial frequency. It is that possibility which is explored and emphasized in this paper.

The wind stress used for the slab model was computed as $\tau = \rho_a C_d |\mathbf{u}_a - \mathbf{u}_s|(\mathbf{u}_a - \mathbf{u}_s)$ where ρ_a is the surface air density and C_d is the drag coefficient here assumed to be nonlinear following Large and Pond (1981) and corrected for low winds according to Trenberth et al. (1989). $\mathbf{u}_a$ is the 10 m wind and $\mathbf{u}_s$ is the surface currents of the ocean as measured by the drifters. The inclusion of ocean currents in the wind stress equation has been proven to be important in wind-forced models (Xu and Scott, 2008). This can be done in many ways, for example through the use of a wind stress surface current correction term using a coupling coefficient s_τ

as proposed by Renault et al. (2020). We computed s_τ but found it to consistently be 5-10% or less of τ and lacking any spatial pattern suggesting it would be relevant to the total wind stress on the LBE or comparison between different drifters. Hence we have here opted to simply use the relative ocean and atmosphere velocities $(\mathbf{u}_a - \mathbf{u}_s)$ when computing the wind stress. The spatially and temporally varying wind stress was interpolated onto the location of each drifter at every time step as forcing for the Lagrangian slab model associated with that individual drifter trajectory.

To explore the effect of the presence of the LBE pressure gradients on near-inertial motions two different slab models were set up, including and excluding the rhs pressure terms in (1.1). Both were forced using the the Coriolis parameter as $f = 2\Omega \sin\phi$, where Ω is the rotation rate of the Earth and ϕ is the latitude, as well as a linear damping term (r). The horizontal pressure-gradient forcing is derived from satellite altimetry with the terms η_x and η_y, the gradients of the sea surface height of the LBE, evaluated along the Lagrangian drifter trajectory, and g is the acceleration due to gravity at latitude 69.5°N, the mean latitude of the LBE center. Since the available gridded satellite altimetry under-resolves many features, both in shape and magnitude (Ballarotta et al., 2019), 'scaling factors' of 1.6 and 2.1 were applied to the zonal and meridional gradients respectively (see details in Appendix 1.6). H is the mixed layer depth, ρ_0 is the density of seawater which we assume to be constant at a value of 1025 kg/m^3. The mixed layer depth was set at a constant 52 m based on mixed layer climatology (Holte et al., 2017) which was determined to agree well with the in situ data from a shipboard CTD transect performed just before the drifters were deployed. The damping coefficient r was empirically determined from the e-folding decay time scale of the near-inertial amplitude in the inertially band-passed velocity time series and estimated to be $0.11f$ during the first month of deployment.

Following methodology described in e.g. D'Asaro (1985) or Alford (2001) equations (1.1) can be solved using a numerical ODE solver. The near-inertial wind-work rate was calculated as

the dot product of the wind stress and the inertially band-passed slab-model velocity,

$$W_I = \tau_x u_i + \tau_y v_i, \tag{1.2}$$

which represents the instantaneous rate of wind energy input to the near-inertial mixed-layer motion per unit area.

After solving the slab model, we band-pass filter the output into near-inertial and slowly varying eddy components using the same filters applied to the drifter velocities as described in section 1.3a. We define the horizontal near-inertial and eddy velocity vectors as $\vec{z}_i \equiv (u_i, v_i)$ and $\vec{z}_e \equiv (u_e, v_e)$, respectively. The total horizontal velocity is therefore $\vec{U} \equiv (U,V) = \vec{z}_e + \vec{z}_i$. Substituting this decomposition and $\rho_0^{-1}\nabla P = g\nabla\eta$ into equations 1.1, multiplying the zonal and meridional equations by u_i and v_i, respectively, and summing gives the following near-inertial kinetic-energy tendency:

$$\frac{D}{Dt}\left(\frac{u_i^2+v_i^2}{2}\right) = -u_i\frac{Du_e}{Dt} - v_i\frac{Dv_e}{Dt} + fu_iv_e - fv_iu_e + \frac{\vec{z}_i\cdot\vec{\tau}}{\rho_0 H} - g\vec{z}_i\cdot\nabla\eta - r_I(u_i^2+v_i^2) - r_M(u_iu_e+v_iv_e) \tag{1.3}$$

Here all terms are evaluated at the location of each drifter. The drag term applied to the eddy velocity alone $r_M(u_e^2+v_e^2)$ is neglected, as the eddy velocity extends hundreds of meters below the mixed layer depth H. The cross-term $r_M(u_iu_e+v_iv_e)$ is likewise negligible since u_i and u_e oscillate on very different timescales, their product averages close to zero over an inertial period, and we therefore drop this term from the analysis. The damping in the near-inertial energy budget thus reduces to $-r_I(u_i^2+v_i^2)$, consistent with r_I being estimated from the decay of near-inertial amplitude alone. The various cross terms on the right-hand side of equation 1.3 are the result of the addition of an extra term to the slab model and will be explored further

in section 1.5.2. We further note that, because this pressure-gradient term is formed from the dot product with the near-inertial velocity $\vec{z}_i$, only the component of $\nabla\eta$ that projects onto the near-inertial band contributes to the near-inertial energy budget; that is, $\vec{z}_i \cdot \nabla\eta = \vec{z}_i \cdot (\nabla\eta)_I$ in the inertial band average, where $(\nabla\eta)_I$ is the inertially band-passed sea surface height gradient. The full (unfiltered) gradient $\nabla\eta$ is nonetheless retained in the momentum equations (1.1), as it represents the total local pressure gradient force experienced by the drifter.

Previous studies have analogously used a modified form of the Eulerian slab model framework to include the influence of background geostrophic flow, for example through shear production terms arising from nonlinear advection (e.g. Whitt and Thomas (2015); Jing et al. (2017)). The Lagrangian slab model provides an alternative way of examining a related problem: in the Lagrangian framework, the nonlinear advection terms are implicitly represented within the material derivative on the left-hand side of equation 1.3, which is directly sampled by the drifters. Instead, the explicit forcing term appears as the covariance (or correlation) of the time-varying mesoscale pressure terms experienced in a Lagrangian frame of reference.

1.3.5 Cyclogeostrophy

The cyclogeostrophic balance is defined as

$$fV_a - \frac{1}{\rho_0}\frac{dP}{dr} - \frac{V_a^2}{r} = 0 \tag{1.4}$$

where the first term is the Coriolis term, the second the pressure term and the third is the centrifugal acceleration term (Vallis, 2006; Shakespeare, 2016). The azimuthal velocity V_a can be computed as $V_a = \mathrm{Re}[(u+iv)e^{i(\pi/2-\theta)}]$ where θ is the angle between the center of the eddy and the drifter position and $u+iv$ is band-passed around the eddy rotation frequency f_{LBE} corresponding to a period of 3.5 days. We use a filter of 0.7-1.7f_{LBE} and choose to band-pass to limit the inclusion of the translation of the eddy. The relative vorticity is then $\zeta = r^{-1}d(rV_a)/dr$. The pressure term dP/dr was estimated from the same scaled sea surface height gradient field

used in the slab model using the trigonometric relationship $\frac{dP}{dr} = \frac{dP}{dx}\cos(\theta) + \frac{dP}{dy}\sin(\theta)$ where θ is the angle between the eddy center and drifter location at each time step.

1.4 Results

1.4.1 Wind forcing

During the first month of deployment when there were at least six drifters in the eddy, two storm systems passed through the area (low sea level pressure and high winds, see Figure 1.3b). The first and stronger one took place around September 22nd and the second, smaller one, took place around October 4th. The MiniMet that was deployed with the SVP array stayed in the eddy for 47 days and recorded maximum sustained wind speeds of about 25 m/s and a minimum sea level pressure of 972 hPa. Figure 1.2a and b shows the two sides of the spectrogram of the wind from the MiniMet highlighting that there is a broad range of frequencies in the wind forcing during the first month of deployment. Here we have opted to use reanalysis winds interpolated onto the drifter locations as a conservative estimate of wind work rates, see further discussion in section 1.5.4.

1.4.2 Kinematic properties of the LBE

Satellite altimetry suggests that for the first two months of deployment, the LBE is identifiable as a sea surface height maximum centered around 69.5° N and 3.5° E with a radius of about 40 km (identified as the outer edge of closed sea surface height contours). Based on satellite-derived velocities, the geostrophic vorticity in the LBE center is on average 0.1-0.2f during the first month of deployment. This is in agreement with previous altimetry and model studies (e.g. Bashmachnikov et al., 2017;Volkov et al., 2015).

The unfiltered velocity time series shown in Figure 1.1c suggests that the drifter motion consists of two primary superimposed signals. There is a low-frequency motion of the drifters going around the eddy with a period of about 3-4 days. There are also energetic near-inertial

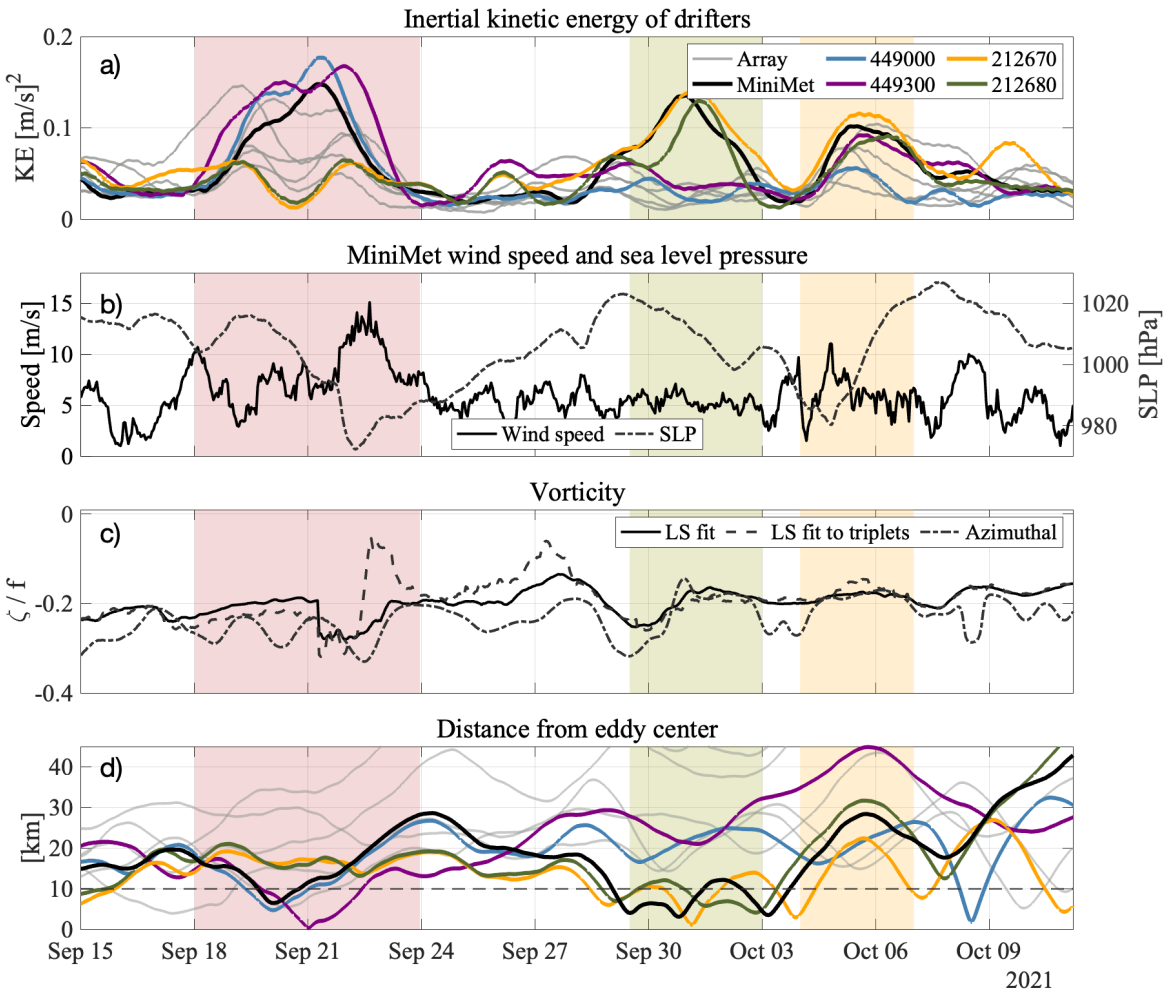


Figure 1.3. a) Drifter near-inertial kinetic energy with the two pairs and MiniMet highlighted in color. b) *In situ* wind speed at 30 cm above the sea surface and sea level pressure from the MiniMet. c) Vorticity of the LBE computed three ways: least squares fitting to the full array, to triplets of drifters and then averaged, and from the azimuthal velocity (rotation rate around the eddy). d) Drifter distance from the MWRA identified eddy center. The dashed horizontal line marks the approximately 10 km radial distance of the eddy core.

motions with a period of about 12.5 h. On occasion, this period is larger(red-shifted). Figure 1.2c shows the anticyclonic (clockwise) MWRA spectrogram of the same drifter whose time series is shown in Figure 1.1c, which also is the drifter that stayed in the eddy the longest. The (high frequency) near-inertial motions can be seen as the line of ridge points with slightly varying frequency and intensity centered around the local Coriolis period of about 12.5 h. The (low frequency) rotation around the eddy, can be identified as the set of ridge points stringing together a ridge with a period of about 3-4 days, taken to be an estimate of the eddy period. The MWRA-derived eddy center location will be used as the reference eddy center going forward. The estimated distance of each drifter to the center can be seen in Figure 1.3d.

Figure 1.3a shows the near-inertial kinetic energy of the drifters and Figure 1.3b the wind and sea level pressure as measured by the MiniMet. If the low-passed drifter velocities are assumed to represent eddy velocities we can estimate various kinematic properties of the LBE. Figure 1.3c shows the vorticity of the eddy estimated by least-squares fits using (1) the full drifter array and (2) the average of all possible combinations of three drifters in the eddy, as well as the average relative vorticity computed from the estimated azimuthal velocities as described in section 1.3c. The average eddy vorticity is -0.3f to -0.2f in the first month of deployment, which is slightly less than previous subsurface in situ estimates (e.g. Fer et al., 2018). Where the drifters are in the eddy at each time of the near-inertial kinetic energy time series can be found in an animation in the supplemental material.

Figure 1.4a shows the 2 km bin averaged root mean square velocity of all the drifters with respect to the eddy center in the first 3 months of deployment. The drifters display increasing azimuthal velocities up to about 10 km suggestive of this being the core of the LBE. Previous *in situ* studies using shipboard ADCP and RAFOS floats suggest the core of the LBE to be 7-8 km radius (Søiland and Rossby, 2013), or, using gliders, to be about 5 km radius (Yu et al., 2017). Between 10-20 km radius, the drifters move with approximately the same azimuthal velocity (larger absolute speed as they move away from the center), and beyond

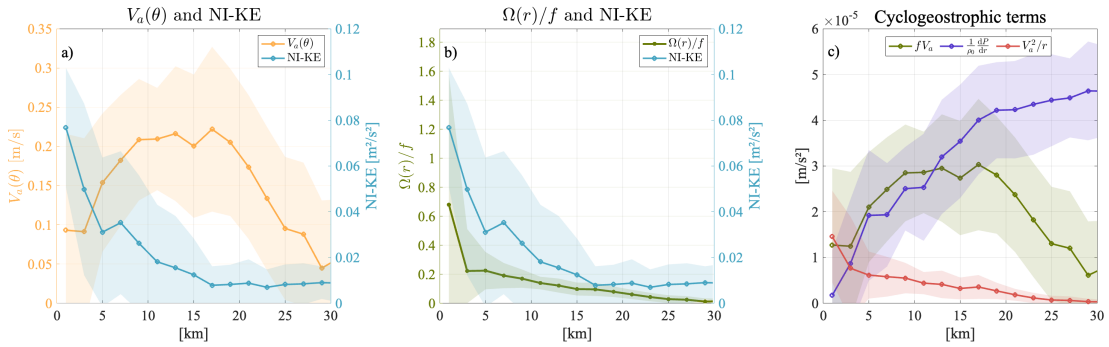


Figure 1.4. a) Root mean square velocities, both near-inertial and azimuthal, averaged from all drifters over 3 months of deployment versus radial distance from the eddy center divided into 2 km bins starting at 1.5 km. b) Rotation rate as a function of radius and near-inertial rms velocity with the same binning. c) Absolute values of the terms of the cyclogeostrophic balance with the same binning. Shaded areas show $\pm\sigma$, one standard deviation range from the mean.

that, the azimuthal velocity starts declining, indicating the outer edge of the eddy. Figure 1.4b shows the rotation rate as a function of distance from the eddy center. Had the eddy been in perfect solid body rotation this rate would have been constant with radius, instead it peaks near the center and drops from 0.1 to 0.2 between 2-15 km suggesting there is some level of radial shear in the eddy. Meanwhile, the rms near-inertial velocity of the drifters is highest in the center, a point that will be revisited in section 1.5. The variability of reported size and strength of the LBE between satellite altimetry and in situ data is seen in previous literature (e.g Köhl, 2007; Søiland and Rossby, 2013; Bashmachnikov et al., 2017; Fer et al., 2018). The 2 km bin averaged cyclogeostrophic terms seen in Figure 1.4b will be discussed further in section 1.5.1.

1.4.3 Near-inertial energy patterns

A key result of this work is that different drifters all located inside the LBE display different amounts of near-inertial kinetic energy at different times, despite being subjected to equivalent wind forcing from the same storm (see also animation in Supplemental Material). In Figure 1.3a we see that discrepancies between drifter near-inertial kinetic energy happen at least three times in the first month of deployment. Hereafter these are referred to as “near-inertial

kinetic energy events“, which are further described below and marked in Figures 1.3-1.8 colored, red, green and yellow respectively. During these events, particularly event one and two, drifters near the center of the LBE display higher values of near-inertial kinetic energy, as seen in Figure 1.3a and d, than drifters further away. This is also supported by Figure 1.4b, where on average near-inertial kinetic energy is higher closer to the center of the LBE as discussed in the previous section.

To explore this behavior further, we note that in the band-passed near-inertial kinetic energy (Figure 1.3a), four drifters stand out as being in two opposite pairs behaving very differently for the first two near-inertial events, represented by blue/purple and green/yellow lines. The blue/purple drifter pair display high near-inertial kinetic energy and are close to the center during event one, whereas the second pair, green/yellow, are further away from the center and don't display the same increase in energy. For the second event the roles are reversed. We will compare and contrast these two pairs of drifters to illustrate the dynamics we believe are at play. At the time of each of the pairs peaking in near-inertial kinetic energy near the center of the eddy, they are also accompanied by the MiniMet drifter (black line in Figure 1.3a, d) which provides ground truth for the ERA5 reanalysis winds used.

The first near-inertial kinetic energy event on September 18th-24th is coincident with a moderate wind burst on September 18th (Figure 1.3b). During this event, the blue/purple pair of drifters initially move northward with the northward blowing wind on the western side of the eddy (see animation in Supplementary Material). As the drifter pair circles around the northern edge of the eddy, they slowly move closer to and then into the eddy center and develop strong near-inertial oscillations. About 4 days after the initial wind burst there is a large low-pressure system with strong winds moving through the region on September 22nd. During this wind event, the near-inertial energy decreases for both drifters. The drifters in the other pair (green/yellow) initially move perpendicular to the first wind burst on September 18th, then travel against the wind as they head southward along the eastern side of the eddy. They do not develop any

appreciable near-inertial kinetic energy during this event.

About 9 days later at the time of the second near-inertial event on September 29th - October 3rd, the pairs have switched places in the eddy and the green/yellow pair is now inside the solid body rotation core. At this time the green/yellow pair develop energetic near-inertial oscillations. There is no wind burst at the start of or during this period (Figure 1.3b), but this does seem to be a time when the eddy exhibits a relatively stronger negative vorticity (Figure 1.3c).

The third near-inertial kinetic energy event on October 4th-7th is the smallest in magnitude. All four drifters in both pairs show a modest increase in near-inertial kinetic energy at this time. The amount of near-inertial energy is approximately inversely proportional to distance from the eddy center (more/less near-inertial kinetic energy closer to/further away from the eddy center). All drifters are within a 20-40 km radial distance from the eddy center during this time, but none are as close as during event one and two.

1.5 Discussion

To explore the role that the eddy itself plays in the variability of the upper ocean response to wind forcing and the near-inertial energy bursts described above, we first evaluate the dynamical balance of the LBE in the framework of cyclogeostrophy (section 1.5.1). After that we evaluate outputs from slab models and look at the energy tendency of the system (section 1.5.2). In section 1.5.3 we discuss a proposed mechanism for eddy-NIO pumping. Lastly we discuss high-resolution satellite altimetry data and the limitations of this work in section 1.5.4.

1.5.1 Cyclogeostrophy

In an idealized anticyclonic eddy, the outward pressure gradient and centrifugal acceleration together balance the inward Coriolis acceleration, all terms are linearly proportional to the radius and vanish at the center of the eddy. However, evaluation of the terms in the cyclogeostrophic balance in the LBE points to this system not always being in equilibrium.

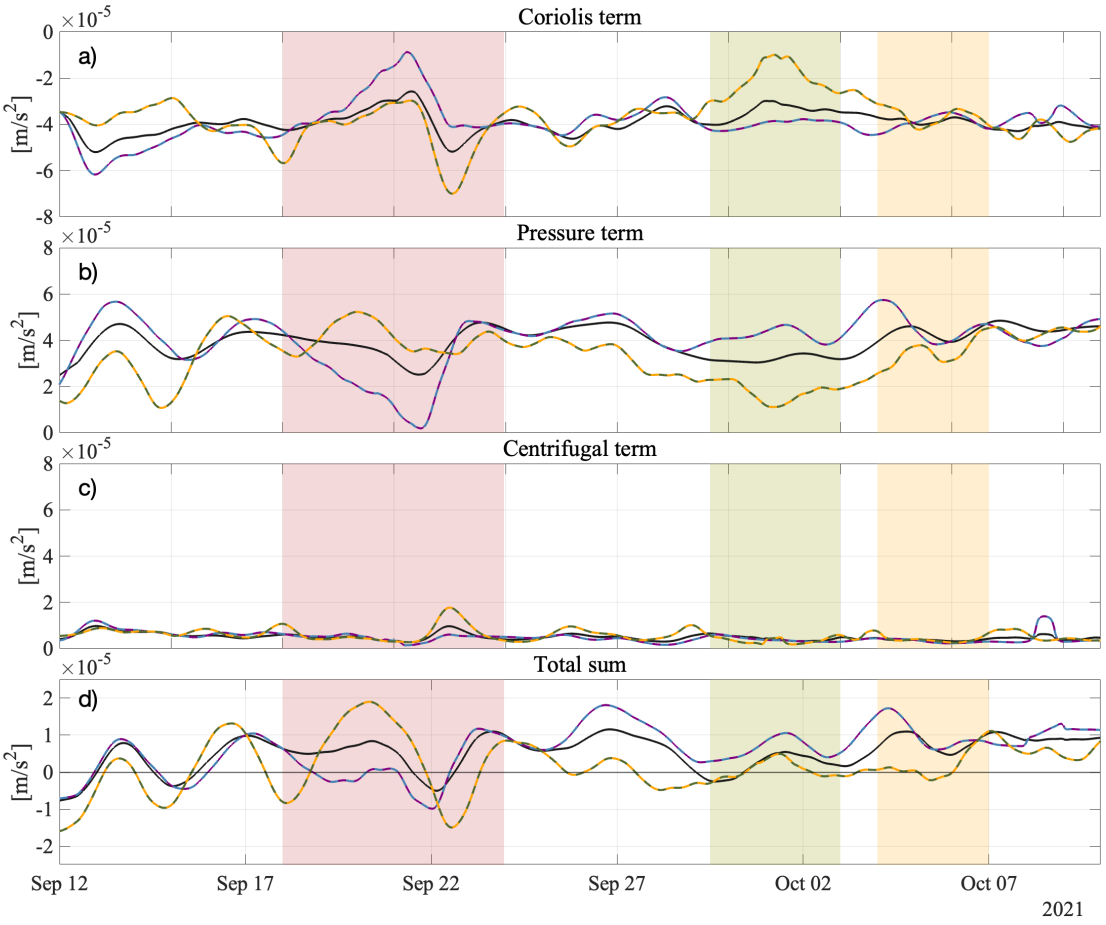


Figure 1.5. a-c) show the respective terms of the cyclogeostrophic balance equation 1.4, and d) the total sum. The multicolored lines represent the two drifter pairs and their individual averages, black line represents the average of the other drifters in the array. Note the reverse y-axis in panel a).

Figure 1.4b shows the bin averaged terms of equation 1.4 versus radius, and Figure 1.5 shows the time series of each of the terms for the two pairs (blue/purple and green/yellow) as well as the average of the 6 other drifters in the array (black line). As seen in Figure 1.5d, the total sum of the cyclogeostrophic terms do not add up to be near zero most of the time, with the exception of the yellow and green pair between September 27th and October 5th which is near zero. The greatest variability in the total sum of the balance, occurs around the time of the first energy event, suggestive of the strong storm on September 22nd having imparted energy to the system and disrupted the balance. Given the jostling between the LBE and its neighbors reported in previous literature (Trodahl et al., 2020; Bosse et al., 2019), we expect that some of the deviation from balance is related to this eddy-eddy interaction as well.

In Figure 1.4c, the Coriolis term is a function of the azimuthal velocity and displays the same behavior as V_a in Figure 1.4a. If we assume the eddy can be approximated as a Rankine vortex, that is, as a disc-shaped region with constant vorticity for radius $0 < r < R_{max}$ and where the flow is irrotational for $r > R_{max}$ (Batchelor, 1967), then a cross-section of sea surface height through the eddy would approximate a parabola so that the pressure gradient term would also be linearly proportional to r and smaller near the center. Figure 1.5a and b show the drifter pair-averaged Coriolis and pressure terms being smaller when the drifters are near the center, as expected, and these two terms are also of similar magnitude. Note that the Coriolis term in Figure 1.4c does not drop off as quickly near the center as the pressure term, nor does it reach zero. The centrifugal term is about four times smaller than the other terms and does not display linear behavior with increasing radius as expected in an idealized scenario. Instead the centrifugal term is largest near the center and decays outwards. We believe all of these deviations from the idealized scenario are related to the observed increase in near-inertial kinetic energy seen near the center of the eddy in Figure 1.4a and will discuss this further in the next sections. We however recognize that the estimation of this balance is subject to several sources of uncertainty (including the estimate of the eddy center location and the resolution of the sea surface height product used to estimate the pressure gradient), and consequently these results

should be regarded as indicative rather than definitive.

Eddies such as the LBE that are episodically perturbed from cyclogeostrophic balance may respond with near-inertial oscillations of their own. Translational modes of a compact rotating vortex oscillate at exactly f (Young, 1986; Cushman-Roisin, 1987), while analytical solutions for elliptic warm-core vortices admit inertial pulsation modes (the so-called pulsrodon) in which the eddy boundary expands and contracts periodically (Rogers, 1989). Laboratory and numerical evidence confirms that such inertial pulsing occurs in warm-core eddies (Rubino and Brandt, 2003; Rubino et al., 2007), though direct observations of these modes in the open ocean remain scarce. Grisolía and Martínez-Marrero (2026) observe eddy pulsation at lower latitudes on longer time scales. Using the MWRA technique applied to independent drifter subsets, we observe near-inertial oscillations of the LBE center position that are coherent across subsets, suggesting genuine vortex center motion rather than a tracking artifact (see Appendix B). This oscillation forms a key component of the inertial pumping mechanism developed in section 1.5.3, to which we turn after first presenting the slab model results.

1.5.2 Slab model output and wind work

To evaluate the source of energy for the observed near-inertial events in Figure 1.3, estimates of the wind work done on the LBE were carried out for both a standard slab model and the version including a pressure gradient term. The null hypothesis here, consistent with previous work, is that the wind stress term alone (the standard slab model) would explain the bursts of near-inertial energy seen. That is not the case.

Figure 1.6 shows the zonal velocity, wind work rate and summed work (equivalent to energy) as well as the near-inertial kinetic energy from the drifter and slab models for the blue drifter for event one, and the yellow drifter for event two. These are arbitrarily chosen as representatives of each pair to evaluate the slab models and compare and contrast near-inertial kinetic energy events. In each case of Figure 1.6a-l the band-passed (inertially) filtered drifter

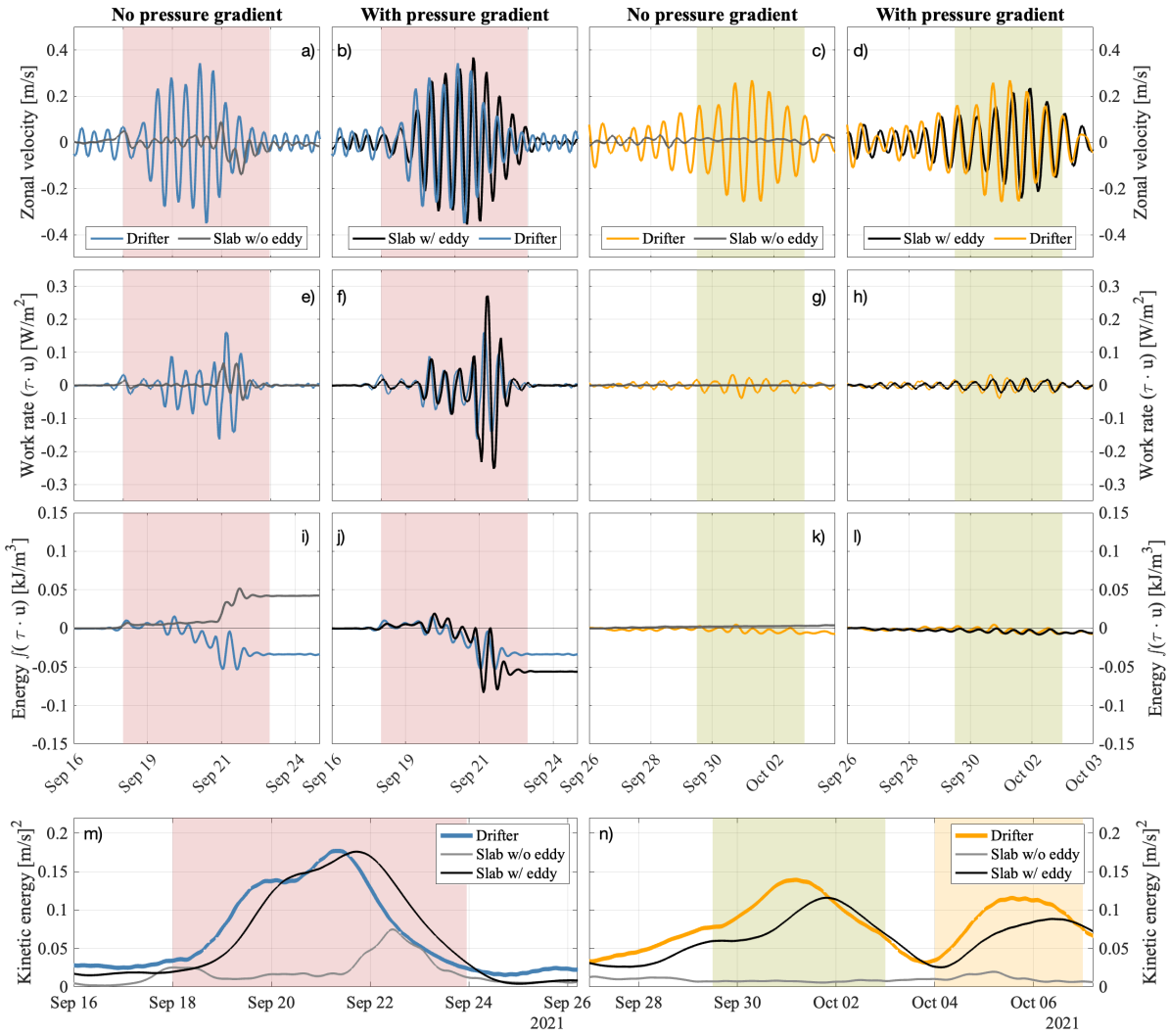


Figure 1.6. Slab model outputs for the blue and yellow drifter during event one and event two. The top row shows zonal velocity, the middle row shows wind work rate W_i and the bottom row shows summed wind work rate $\int(\tau \cdot u)$ (total energy input per unit area). Panels a,e,i) are for the blue drifter during event one with the inertially filtered velocity and output from the slab model without a pressure gradient term, and b,f,j) the inertially filtered velocity and inertially filtered output from the slab model with a pressure gradient term. Panels c,g,k) and d,h,l) are the equivalent for the yellow drifter and event two. The summation of the wind work to arrive at the total energy input panels i,j,k,l) begins at the start of the x-axis in question, September 16th and 26th respectively. Panel m) shows, for event one, the near-inertial energy of the drifter (colored line), as predicted by the unmodified slab model (grey), and by the modified slab model (black) that has been band-pass filtered the same way as the drifter data. Panel n) is the equivalent for event two.

velocity is being compared with the wind work only slab model output and the inertially filtered output of the slab model with an added pressure gradient term. Figure 1.6 panels m and n show the near-inertial energy as captured by the drifter and each of the versions of the slab model.

A major result of this work is that the simple slab model with only wind forcing does not replicate the timing or strength of the observed bursts of near-inertial energy. Figure 1.6a and b show the two slab model outputs for event one. The modified slab model with the added pressure terms predicts an inertial response of approximately the right magnitude and timing for event one (Figure 1.6m). The simple slab model, with energy provided only by wind, fails to replicate the observed near-inertial energy peaks in both magnitude and timing. For the first event, the simple slab model underestimates the near-inertial energy and predicts it to peak later than what was observed and further predicts the net wind work is positive and not negative (Figure 1.6 sub-panels e and i).

For the second event on September 30th-October 3rd, the modified slab model similarly reports wind work and total energy input more aligned with that of the actual drifter than what the simple slab model does (Figure 1.6l). While the near-inertial velocities for event one and two are similar, Figure 1.6a and c, the suggested amounts of wind work are not, Figure 1.6 sub-panels e and g. This point will be revisited below in section 1.5.4.

The difference in performance between the two versions of the slab models, and the success of the second slab model in more accurately reproducing the observed timing of near-inertial energy bursts in the drifter data means that the addition of the pressure gradient terms must in some way be key in the near-inertial energy bursts (equation 1.3).

To further investigate the source of energy for the observed near-inertial events, we evaluate each term in equation 1.3 for the blue and yellow drifters, again as arbitrary representatives of each pair. The term that contributes most strongly to the near-inertial energy tendency at the time of peak inertial kinetic energy is the pressure-gradient term involving the sea surface height, $g\vec{z}_i \cdot \nabla\eta$ (dashed colored lines in Figure 1.7a,b). This dominance is evident for both event one and event two. During the first inertial event, the pressure-gradient contribution for the blue

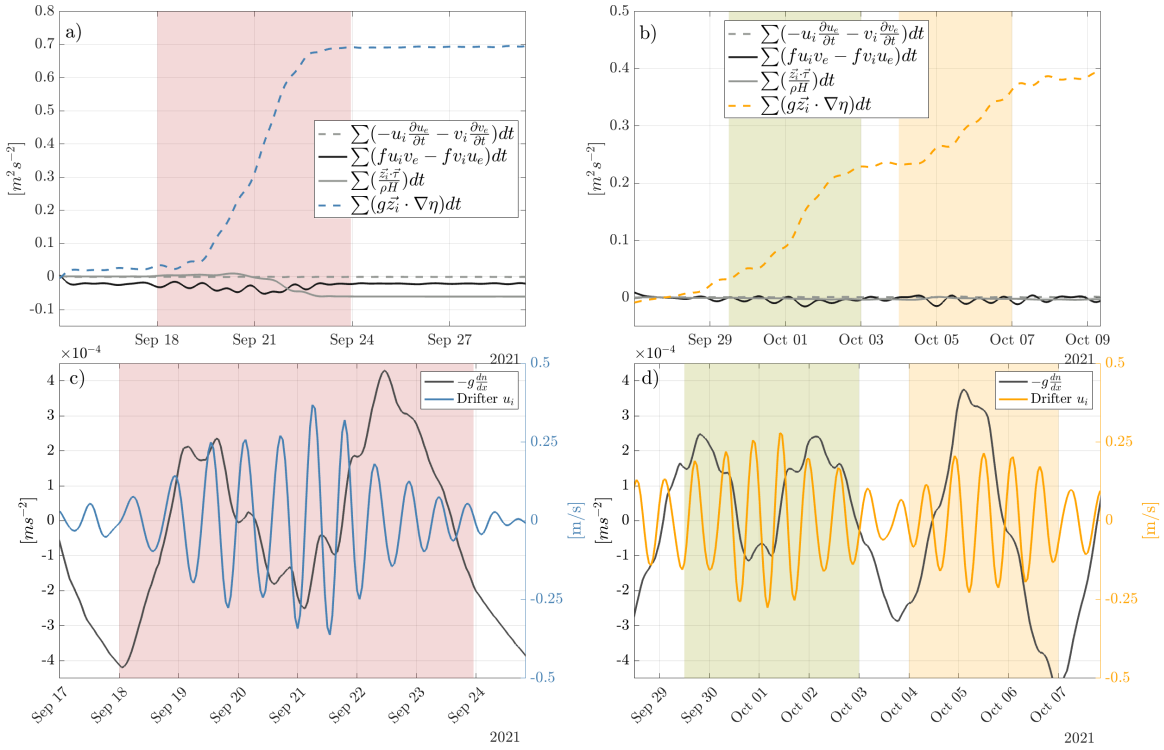


Figure 1.7. Energy tendency of the system. Subpanels a-b) show the individual terms of equation 1.3 for the purple drifter in event one and the yellow drifter in event two. Subpanels c-d) show the drifters' respective near-inertial zonal velocities and the sea surface height gradients they sample for the same events (this is the pressure gradient forcing term used in the modified slab model).

drifter increases by approximately 600% (Figure 1.7a), while for the yellow drifter it increases by roughly 400% during event two and an additional 50% during event three (Figure 1.7b). No other term in equation 1.3 exhibits comparable growth during these periods. At the same time, Figure 1.7c,d show variability in the pressure gradient term on time scales similar to the inertial velocities which we will discuss next.

1.5.3 Eddy-NIO pumping: a forced damped oscillator

The observations presented above suggest that energy is going into near-inertial motions near the eddy center due to a *pressure-work* term. What produces this term? We begin again

with the Lagrangian form of the slab model momentum equations (D'Asaro, 1985)

$$\frac{Du}{Dt} = fv \quad -g\eta_x - ru \tag{1.5}$$

$$\frac{Dv}{Dt} = -fu \quad -g\eta_y - rv \tag{1.6}$$

The pressure gradient term (represented by sea surface height $\nabla\eta$) is a function of where the drifter is with respect to the eddy center, as it moves in the eddy pressure field. Let the location of the eddy center be given by (x_c, y_c). For an eddy in perfect cyclogeostrophic solid body rotation, the pressure field is parabolic, with gradients given by

$$\begin{aligned} \frac{d\eta}{dx} &= \frac{f\alpha}{g}\left(1+\frac{\alpha}{f}\right)(x-x_c) \\ \frac{d\eta}{dy} &= \frac{f\alpha}{g}\left(1+\frac{\alpha}{f}\right)(y-y_c) \end{aligned} \tag{1.7}$$

where α is the rotation rate of the eddy such that the azimuthal velocity is $u_\theta = \alpha r$. For our anticyclonic eddy $\alpha < 0$. We make a complex form of these equations by adding the first one and i times the second, defining $z_c \equiv x_c + iy_c$ is the complex eddy center, $z \equiv x + iy$ is the drifter location, $\dot{z}$ is the complex drifter velocity, and $Ro \equiv \alpha/f$ is a non-dimensional Rossby number:

$$\frac{D\dot{z}}{Dt} + if\dot{z} = -Rof^2(1+Ro)(z-z_c) - r\dot{z} \tag{1.8}$$

This is a *forced damped oscillator*. The $(1+Ro)$ rhs term explicitly shows the dependence on the degree of nonlinearity of the eddy. To get an energy tendency equation we multiply by the complex conjugate of drifter velocity, $\dot{z}^*$ and define $\beta \equiv Rof^2(1+Ro)$ to get

$$\frac{D}{Dt}\left(\frac{1}{2}|\dot{z}|^2\right) = -\beta\dot{z}^*(z-z_c) - r|\dot{z}|^2 \tag{1.9}$$

Rearranging again gives

$$\begin{aligned} \frac{D}{Dt}\left[\frac{1}{2}|\dot{z}|^2+\frac{1}{2}\beta|z|^2\right] &= \Pi - r|\dot{z}|^2 \\ \Pi &\equiv \beta \dot{z}^* z_c \end{aligned} \tag{1.10}$$

We interpret the lhs by noting that the first term in the brackets is the kinetic energy of the drifter. To interpret the second term in the brackets we note that in cylindrical coordinates the parabolic pressure field can be written as

$$\begin{aligned} g\frac{d\eta}{dr} &= \beta r \\ g\eta &= \eta_0 + \frac{\beta r^2}{2} \end{aligned} \tag{1.11}$$

Recall from our definition of β that it is still signed, so for an anticyclonic eddy $\beta < 0$. Another way to phrase this formulation is that β is the potential field of the eddy. Thus we loosely interpret the second term in the brackets on the lhs of (1.10) as the movement of the drifter in the potential field of the eddy. So the total lhs of (1.10) can be thought of as the rate of change of energy of the drifter, or rather of the water parcel the drifter is tracking.

The rhs of (1.10) tells us that the total water parcel/drifter energy changes due to a negative definite drag term, and and energy transfer term Π. This Π term is the rate of pressure work done by the *drifter and eddy, with its whole eddy pressure field, both moving with respect to each other*. The key to a positive energy transfer is both the relative frequencies of the eddy center and drifter oscillation, and their relative phasing. To make that relationship clearer lets say the drifter moves with a complex velocity

$$\dot{z} = u_d e^{-i[f_d t + \phi_d]} \tag{1.12}$$

where u_d is a positive definite amplitude of the drifter velocity and f_d is a near-inertial frequency.

Let's say the eddy center moves with a velocity

$$\dot{z_c} = u_c e^{-i[f_c t + \phi_C]} \tag{1.13}$$

where f_c is the frequency at which it is oscillating where u_c is a positive definite velocity scale. In an idealized symmetric eddy, translational modes produce center-of-mass displacement at exactly f (Young, 1986; Cushman-Roisin, 1987), while pulsation modes produce radial breathing without net center displacement (Rogers, 1989; Rubino and Brandt, 2003; Rubino et al., 2007). In the real, asymmetric LBE with $Ro \sim \mathcal{O}(1)$, nonlinear mode coupling and asymmetric forcing are expected to entangle these modes, such that the observed near-inertial oscillation of the eddy center position likely reflects contributions from both. In Figure 1.8c we observe spectral peaks near both f and f_{eff}. While we cannot fully exclude aliasing of drifter near-inertial oscillations into the MWRA center estimate, the coherence of the inertial center oscillation across independent MWRA runs using drifter subsets with differing radial positions provides evidence that the signal reflects genuine eddy center motion rather than a pure tracking artifact (see Appendix B). Regardless of the precise modal decomposition, the energy transfer mechanism described by Π requires only that z_c oscillates near-inertially.

The position of the eddy center is given by integrating to get

$$z_c = \frac{i u_c}{f_c} e^{-i[f_c t + \phi_C]} = \frac{u_c}{f_c} e^{-i[f_c t + \phi_C + \pi/2]} \tag{1.14}$$

The energy transfer term Π is then given by

$$\Pi = \frac{\beta u_d u_c}{f_c} e^{i[f_d - f_c]} e^{i[\phi_d - \phi_c + \pi/2]} \tag{1.15}$$

Recall that for an anticyclonic eddy, $\beta < 0$, so positive energy transfer to near-inertial motions requires the rest of the rhs of (1.15) to also be negative. The magnitude of the energy transfer depends on the velocity of both the eddy center and the drifter, as well as the strength

of the eddy itself through β. But the key to whether that energy transfer is positive depends on the two exponential terms in (1.15). The first of those terms tells us that if they are exactly the same frequency ($f_c = f_d$) then transfer is maximized. When they are not quite the same, the energy transfer is modulated at the beat frequency $|f_d - f_c|$ when $f_c \neq f_d$. For the observed sub-inertial peak of eddy center movement (Figure 1.8c) this beating from the difference frequency is expected to produce a slow modulation in energy transfer on the order of a week, consistent with the observed spacing of near-inertial kinetic energy events.

The last term in (1.15) tells us about the phasing required for positive energy transfer; specifically it tells us that the eddy center velocity and drifter velocity should be in quadrature, or that the eddy center velocity and the drifter *position* should be in phase. The maximum positive energy transfer happens when $\phi_d - \phi_c + pi/2 = \pi$.Physically, consider a drifter doing inertial circles on the eastern side of an eddy, as the center also oscillated. The drifter gains energy when it is going downhill, and loses energy when it goes uphill. If the eddy center were not moving, these gains and losses would be symmetric. But consider the phasing that maximizes positive Π. If we choose $\phi_d = 0$, without loss of generality, then we get the maximum positive phasing when $\phi_c = -\pi/2$. So if the drifter is moving with velocity $\cos(ft)$ then the *position* of the eddy center goes as $-\cos(ft)$. During the time period when the drifter is moving downhill and gaining energy, the eddy center position has moved away, so the pressure gradient is larger because the drifter is further from the center, meaning the energy gain by the drifter is larger. During the time period when the drifter is moving uphill, losing energy, the eddy center has moved closer, so the 'hill' it has to climb back up is smaller and hence the energy loss is smaller. The actual movement of the eddy center towards or away from the drifter occurs when the drifter is moving perpendicularly, resulting in no work. The net result is a "two steps forward, one step back" energy transfer that is positive when integrated over an inertial period.

The dominance of the pressure work term in adding inertial energy shown in Figure 1.7 is one strong piece of evidence for this proposed mechanism. We can also more directly test the theory described here by calculating Π from (1.10) using the observed movement of the eddy

center and each drifter, see sub-panels d-g in Figure 1.8. The result shows strong resonant energy transfers at the times the drifters are observed to gain near-inertial kinetic energy.

There are a few more points to make about this mechanism. First, the specific phasing required by the last term of (1.15) may seem unlikely to occur by accident. However as with any type of linear instability analysis, the idea is that there may be infinitesimally small water parcel oscillations all the time, or movements that could Fourier project onto such motions. The phasing of the eddy center movement will pick out which of those are in phase and amplify them until they become themselves order one. Second, we argued that when the eddy center moves towards the drifter, it pushes on the drifter, putting energy into it. By Newton's third law the drifter, or rather the water parcel the drifter is embedded in, which is accelerated by this mechanism, must exert and equal and opposite force on the eddy. However, the effective mass of the 1000 meter deep eddy is so much larger than this mixed layer parcel, that we consider the effect on the eddy itself to be modest at best. It could however point to a chain of events whereby an eddy is jostled by a wind event or its unruly neighbors, starts wobbling at near an inertial frequency, sloughs off that energy to smaller sets of inertial oscillations, and they lose their energy either to dissipation at the base of the surface boundary layer or radiation of downward going near-inertial internal waves.

Third, we come back to the observation that the near-inertial kinetic energy is highest in the core of the eddy (Figure. 1.4a). This is also the part of the eddy where the pressure gradient term (key for this mechanism) is changing with radius most rapidly.

Finally it's worth discussing how the results presented here relate to other recent studies on interaction between near-inertial oscillations and eddies, which has predominantly been carried out in the Eulerian framework. Most work has focused on the role of the lateral shear production term (Whitt and Thomas, 2015) which in Eulerian form is given by

$$LSP = -\overline{u'v'}\frac{\partial u_g}{\partial y} - \overline{u'v'}\frac{\partial v_g}{\partial x} \tag{1.16}$$

where u', v' are the 'perturbation' near-inertial velocities and (u_g, v_g) is the balanced eddy flow. For an eddy in solid body rotation, these terms exactly cancel to zero. Of course as visible in Figure 1.4, the LBE is not exactly in solid body rotation, so this term may also play a role. We end by reminding the reader that the near-inertial kinetic energy defined in the Lagrangian framework used here is not identical to that defined in the Eulerian framework of most previous studies: a fluid parcel executing near-inertial excursions samples the spatially varying mean geostrophic flow, so its Lagrangian near-inertial velocity carries a contribution from advection through the mean shear that is absent from the Eulerian velocity at a fixed point. As a result, the two frameworks partition and exchange near-inertial energy through different terms and the energy reported under each need not be numerically identical, even though they offer complementary views of the same physical process.

1.5.4 Limitations and speculations

There are a few limitations to this study that will be discussed here, along with hypotheses regarding the instigation for the second kinetic energy event.

First, the altimetry used in our estimates of the cyclogeostrophic balance, modified slab model and energy tendency analysis is of low spatial and temporal resolution compared to the drifters. Altimetry at a 0.25° x0.25° resolution was not designed to study submesoscale processes and we further acknowledge that there might be steps taken in the production of the altimetry product that produce a distorted representation of the eddy and we only attempt to compensate for reductions in amplitude by applying our scaling factors. To explore these limitations we looked at more recent imaging of the LBE from the SWOT satellite mission (SWOT, 2024). Figure 1.9 shows the difference in resolution between SWOT and the 0.25° x0.25° CMEMS sea surface height product on April 23rd 2023 (the SWOT satellite was launched in December 2022 and hence there is no concurrent data from the time the NORSE drifters were in the LBE in 2021). Not only does the SWOT data reveal the irregular shape of the LBE (Figure 1.9a), but a transect across the eddy center, chosen as a line through the highest sea surface height value

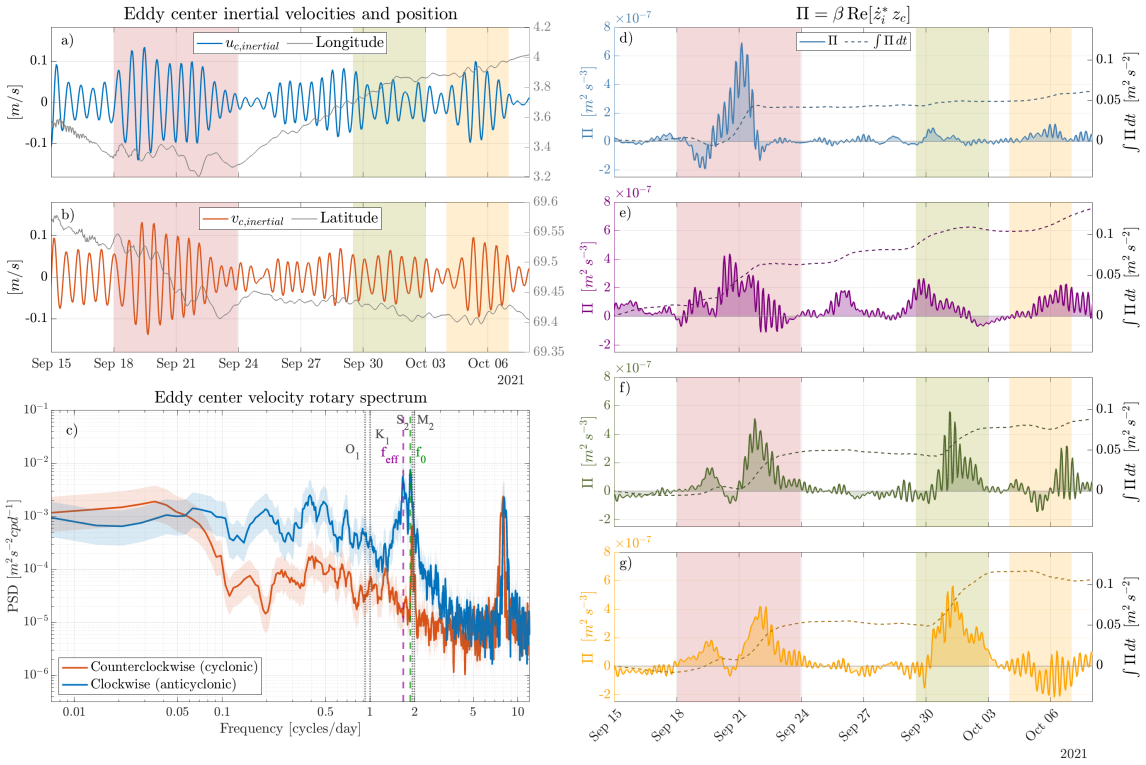


Figure 1.8. a) Inertially filtered eddy center zonal velocity and longitudinal track. b) Inertially filtered eddy center meridional velocity and latitudinal track. c) Rotary spectra of eddy center velocities with vertical lines showing tidal frequencies, inertial frequency f and $f_{effective}$ d-g) The proposed energy transfer term and cumulative sum of the same term for the two drifter pairs.

based on Figure 1.9a, reveals a profile with a core peak of about 5 km radius and considerable variation in the sea surface height gradient. The 0.25° x0.25° gridded sea surface height product cannot capture these steeper slopes and greater detail. Nevertheless,the coarser altimetry we are using here still gets the essential location, shape and crucially movement of the LBE right, as testified to by the close agreement of the comparison in Figure 1.6.

Second, the question was raised whether the varying near-inertial response of the drifters is just a result of small-scale variations in the wind. We have opted to use the ERA5 reanalysis winds to compute the wind stress rather than the in-situ wind from the one MiniMet that was part of the array. Klenz et al. (2022) report that there is generally good agreement between the in-situ data captured by MiniMets, shipboard wind sensors and a reanalysis product such as

ERA5, especially at spatial scales smaller than 25 km, which is on the same order as the size of the LBE. For the 47 days of in situ data from the LBE, the MiniMet and ERA5 wind speeds at 10 m (the MiniMet wind speeds were adjusted to 10 m following Large & Pond (1981)) are in good agreement with the percentage difference between reported wind speeds on average being $\sim$10%. However, Klenz et al. (2022) also report that on the occasion that there are significant discrepancies, the most reasonable explanation is spatial offsets of small-scale storm structures in the reanalysis model, that lead the MiniMet wind work estimates to exceed those of a reanalysis product. Thus, by using ERA5 we have been conservative in our estimations of wind work and we do not believe that spatially varying wind is the main explanation for the differences in drifter near-inertial kinetic energy.

There is also the general question of what makes the eddy start doing inertial oscillations. Before the first event there is a strong wind burst. And though the wind evolution does not resonantly generate inertial oscillations itself, the impulsive work it does on the eddy may produce wobbling of the eddy center. The second inertial event is not preceded by elevated wind; we thus speculate that wobbling of the eddy center in this case may be triggered by interactions with neighboring eddies. One sign of this is in the time series of the estimated relative vorticity of the eddy (Figure 1.3c). Although there is some variability in the different ways of estimating the vorticity of the eddy, there is agreement that just before the second event the vorticity of the eddy strengthens (becomes more negative). The Lofoten Basin Eddy might be the most distinguishable in the Lofoten Basin, however, it is not a lone feature but is surrounded by both cyclones and anticyclones. These neighboring eddies are known to sometimes merge with the LBE (Trodahl et al., 2020; Bosse et al., 2019) and Bosse et al. 2019 also observe changes to the eddy dynamics, like increased translation speed and the ejection of subsurface floats at different depths, after what appear to be a merger. It is possible that these interactions with surrounding vortices can impact the energy balance in the LBE and provide the perturbation needed to trigger a disruption to the inertial motions, and to make a drifter move closer to the center where the

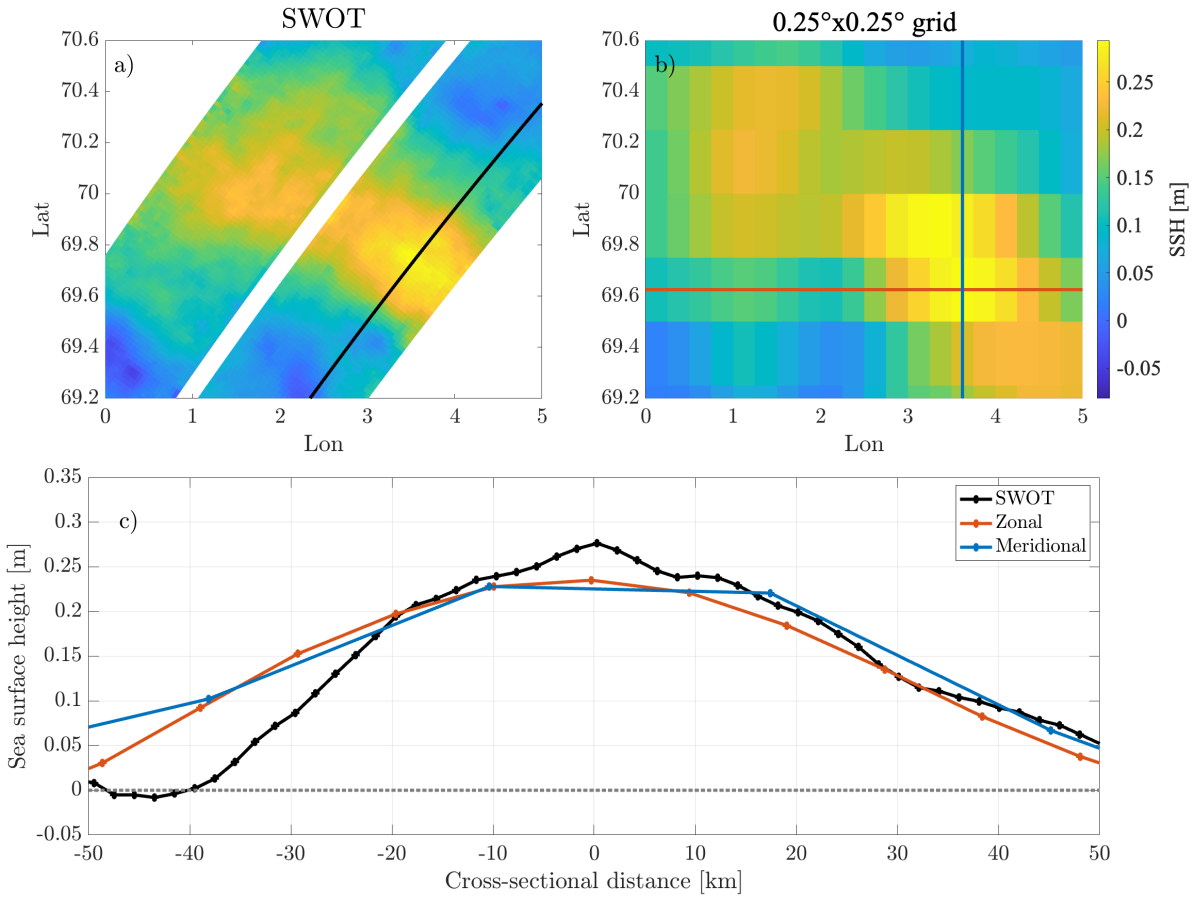


Figure 1.9. Sea surface height field over the Lofoten Basin on April 23rd 2023 as captured by a) SWOT and b) CMEMS 0.25x0.25 degree merged and gridded satellite altimetry product. Panel c) shows the sea surface height profile across the LBE along the lines shown in panels a-b).

oscillations can grow.

A third, even more speculative, hypothesis is that if the near-inertial energy is not coming from wind (above) or is triggered by a neighboring eddy (from the side), could it be possible that it comes from below? Recent work by Thomas et al. (2024) describes seeing near-inertial internal waves being reflected off a strong pycnocline at the base of a North Atlantic anticyclone and reflecting back towards the surface. Initial estimates of the feasibility of the same happening in the LBE suggest that the second energy event happens within a time frame during which a wave generated by the big storm on September 22nd could travel down to the LBE bottom pycnocline at about 1100 m and travel back to the surface in the period between event one and two. These waves might potentially be the cause of a disturbance to the mixed layer, triggering some drifters inertially ringing and moving into the center of the eddy where the inertial oscillations can grow. There is, however, uncertainty around whether the very weakly stratified LBE core can support internal waves, as well as what the initial conditions would be.

Because there is no concurrent sampling beneath the surface layer at the time of the drifters being in the eddy, the fate of the near-inertial energy pictured in these events is unknown, and we can only speculate whether the energy stays in the mixed layer or travels further. This study is also limited to one mesoscale eddy in an active region of the North Atlantic and whether the processes believed to be observed here can be found elsewhere is unknown. However, the advancement of new high-resolution satellite altimetry should help in identifying other eddies where the interactions between sea surface height gradients and NIOs observed here could be taking place.

1.6 Conclusion

Using drifters deployed in a small but energetic mesoscale anticyclone in the North Atlantic, we observed a spatially uneven amplification of near-inertial kinetic energy inside the eddy. Through the use of a Lagrangian slab model we show that the only forcing term that can explain this amplification is the pressure gradient term, which we derive from satellite altimetry. We propose a mechanism for "eddy-NIO pumping" based on the relative phasing of near-inertial motions in the mixed layer and the intrinsic near-inertial oscillations of the eddy center that can result in a net transfer of energy. The first of the observed energy events seems to be at least in part associated with wind forcing, however a later burst of near-inertial energy is observed that similarly draws energy from pressure gradients. In this event there was no wind event to initiate the near-inertial motions of the surface layer; geostrophic adjustment as this eddy interacts with its neighbors is suggested as a possibility. Whether viewed as distinct physical mechanisms or alternative reference-frame perspectives on related processes, we suspect that the interactions described here and by Whitt and Thomas (2015) represent only a subset of the possible ways near-inertial and mesoscale motions can exchange energy.

Acknowledgments

Chapter 1 is in full a reprint of the material it may appear in Journal of Physical Oceanography, 2026, *Fast Times at Lofoten High – Interactions Between Near-Inertial Oscillations and a Strong Mesoscale Eddy*. Bergentz, Kerstin A.; Centurioni, Luca R.; MacKinnon, Jennifer A. The dissertation author was the primary investigator and author of this paper. We acknowlegde funding from NOAA grant NA20OAR4320278 "The Global Drifter Program" and the Office of Naval Research (ONR) grant N00014-21-1-2742 and grant N00014-21-1-2739. We wish to thank the captain and crew aboard R/V Neil Armstrong, everyone participating in the NORSE 2021 cruise under chief scientist Luc Rainville.

Appendix A: Scaling of sea surface height gradients

The gridded altimetry product used here has a standard $0.25° \times 0.25°$ resolution, which under-resolves mesoscale features in both spatial structure and amplitude. Optimal interpolation methods used to bridge sparse satellite tracks act as spatial low-pass filters that smooth gradients (Ballarotta et al., 2019). To compensate for this smoothing, we apply directional scaling factors to the sea surface height gradients, determined empirically from drifter momentum budgets.

For each drifter, we identify time periods when the trajectory exhibits quasi-circular motion at a distance from the eddy center. From the observed drifter velocity, we first subtract wind-driven Ekman currents estimated following Ralph and Niiler (1999). We then band-pass filter the residual velocity and compute its material derivative. The filter passband is $0.7–1.7 f_{LBE}$, where $f_{LBE} = (3.5 \text{ days})^{-1}$ is the characteristic eddy rotation frequency. A band-pass filter is chosen rather than lowpass to exclude any low-frequency signal associated with the eddy's translation (as described in section 1.2). The same temporal filter is applied to all terms in equation 1.17.

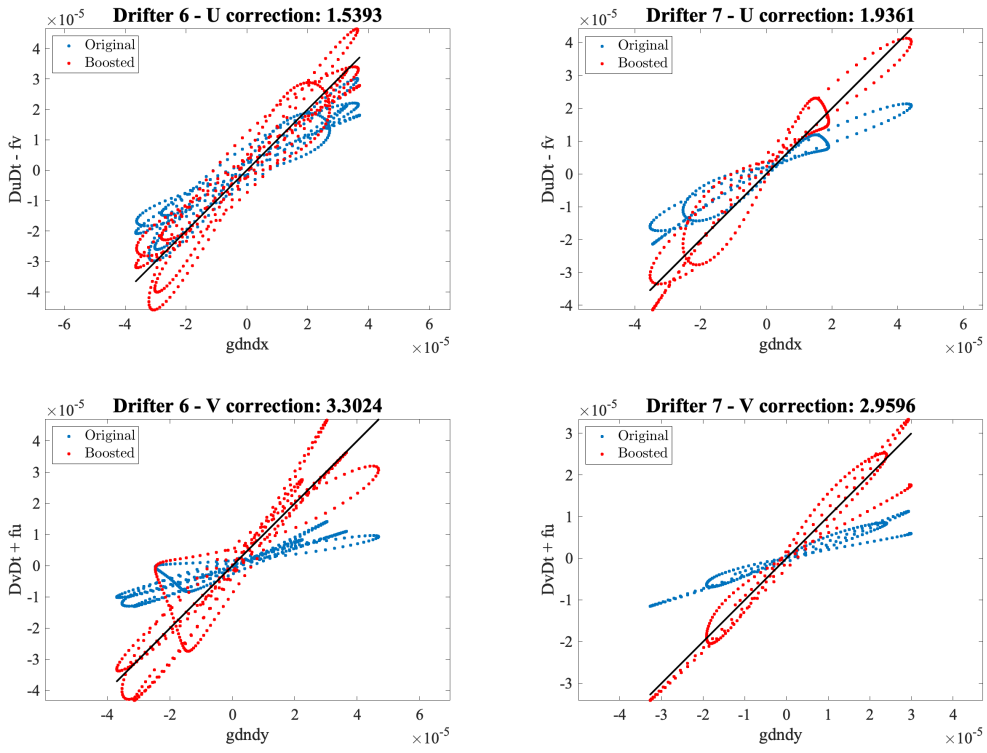


Figure 1.10. Examples of plots to identify scaling factors for the sea surface height gradient based on balancing terms.

$$\begin{aligned} \frac{Du}{Dt} - fv &= -g\eta_x, \\ \frac{Dv}{Dt} + fu &= -g\eta_y, \end{aligned} \tag{1.17}$$

Neglecting wind stress and linear damping over these intervals, we assume that drifters undergoing quasi-circular orbits around the eddy center satisfy the horizontal momentum equations in a rotating reference frame (Equation 1.17), where $\eta_x \equiv \partial\eta/\partial x$ and $\eta_y \equiv \partial\eta/\partial y$. We then perform linear regression of the altimetry-derived pressure gradient acceleration ($-g\eta_x$ or $-g\eta_y$) against the corresponding material-acceleration and Coriolis terms ($Du/Dt - fv$ or $Dv/Dt + fu$). The reciprocal of the regression slope gives the scaling factor required to bring the pressure gradient term into balance with the observed accelerations. Examples of these regression plots for two representative drifters are shown in Figure 1.10.

Across multiple drifters and time periods, we obtain mean scaling factors of 2.1±0.13 (standard deviation) in the meridional direction and 1.6±0.11 (standard deviation) in the zonal direction, with the standard error of the mean (SEM $= \sigma/\sqrt{n}$ where σ is the standard deviation and n is the number of samples) as 0.043 and 0.038 respectively. These directional differences reflect the grid anisotropy at 70°N, where a 0.25° × 0.25° grid corresponds to approximately 27 km (zonal) × 9 km (meridional). Band-pass filtered drifter velocities within the eddy exhibit weak point-by-point Pearson correlation with altimetry-derived geostrophic velocities ($|r_P| \approx 0.2$), but RMS amplitude comparisons indicate that unscaled altimetry gradients underestimate velocity magnitudes by approximately 50–100%. Application of these empirical scaling factors compensates for the spatial smoothing inherent in the gridded product, following established practice for partially resolved mesoscale features (Ballarotta et al., 2019), but this correction adjusts only the amplitude of resolved gradients and does not reconstruct unresolved submesoscale variability.

Appendix B: Eddy center near-inertial oscillations

The eddy center location used throughout this paper is derived from the MWRA applied to all available drifters simultaneously. A potential concern is that near-inertial oscillations of individual drifters at f and f_{eff} could alias into the center estimate, producing apparent center oscillations that are tracking artifacts rather than physical vortex motion (see discussion in section 1.5.3).

To assess the sensitivity of the center estimate to the choice of drifters, we recomputed the MWRA-derived eddy center position using four independent drifter subsets: all drifters 1–9, subset 1–5, subset 6–9, and a subset of drifters 1,3,4,5,7 which are all the drifters that are not part of the two pairs that have distinct peaks in energy. Figure 1.11a-b shows the resulting longitude and latitude time series of the eddy center for each subset over the first month of deployment.

Two features are apparent. First, the absolute center position differs between subsets by up to ∼0.15° in longitude and ∼0.1° in latitude, reflecting the fact that each subset samples

different parts of the eddy and the MWRA centroid is sensitive to the spatial distribution of drifters. This offset is expected and does not affect our proposed mechanism which is based on inertial oscillations of the eddy center rather than its absolute location.

Second, and more significantly, the near-inertial wiggles in the center position time series are coherent across all subsets. The timing, sign, and approximate amplitude of the inertial oscillations align across subsets with very different spatial compositions of drifters. If the inertial center oscillation were a pure artifact of individual drifters near-inertial loops aliasing into the MWRA center estimate, we would expect the artifact to depend strongly on which drifters are included, since drifters at different azimuths and radii are at different phases of their near-inertial oscillations at any given time. The observed coherence across subsets is therefore inconsistent with a pure aliasing artifact and suggests that the near-inertial oscillation of the center position reflects a real property of the eddy.

We note that this test does not constitute definitive proof since drifters within the same eddy share some degree of phase coherence in their near-inertial motions, which could produce spurious coherence in the subset center estimates. A full synthetic validation, in which known near-inertial signals are injected into synthetic drifter trajectories and the MWRA center artifact is quantified, is left for future work. Nevertheless, the subset consistency shown here provides support for treating the observed near-inertial center oscillations as physically meaningful, as assumed in section 1.5.3.

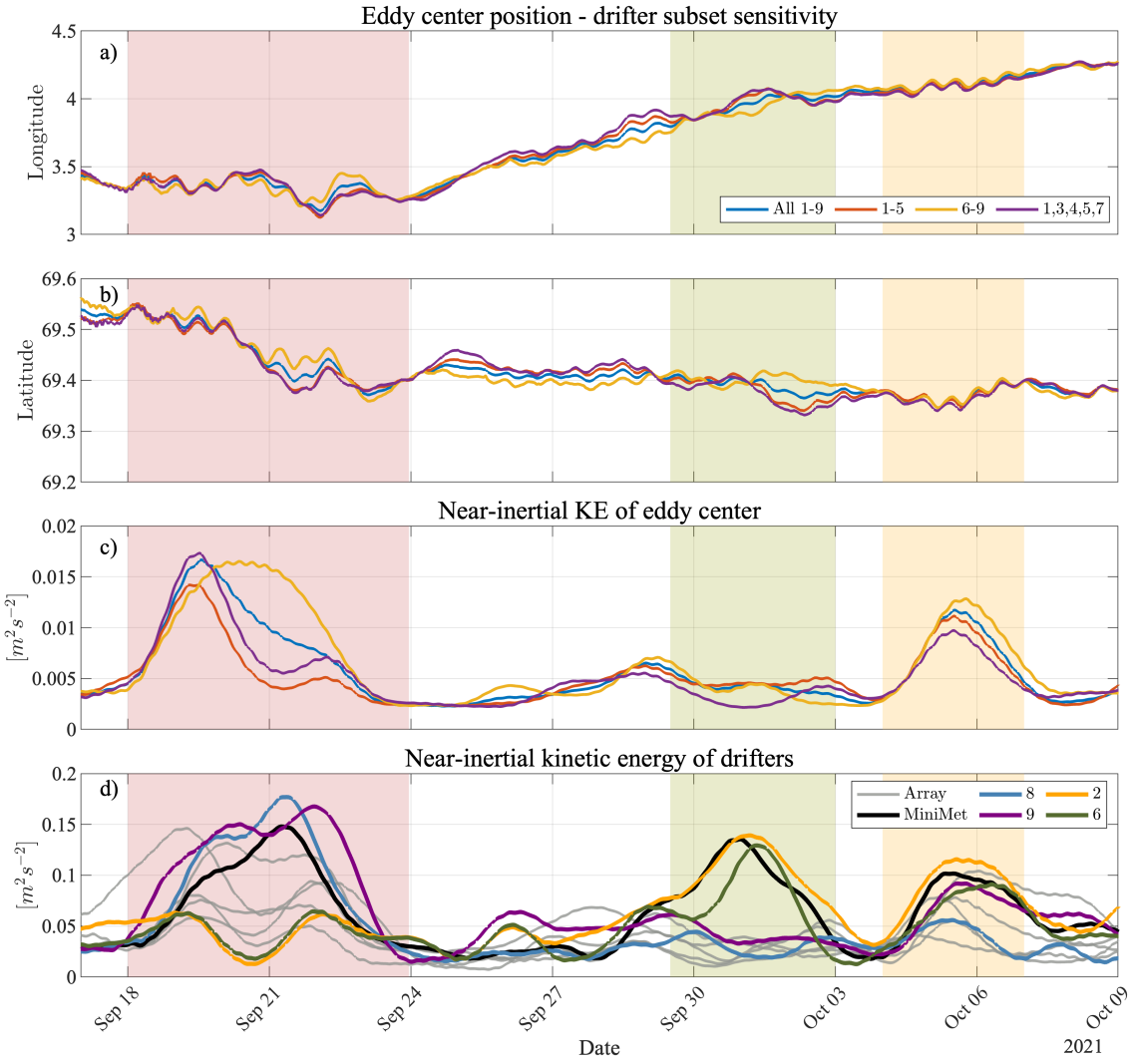


Figure 1.11. a-c) Longitude, latitude and near-inertial kinetic energy of the MWRA derived eddy center for 4 different MWRA runs with different subsets of drifters. d) Drifter near-inertial kinetic energy.

Chapter 2

Sub-Inertial Trapping and Sub-Eddy Vorticity in an Anticyclone: A Multi-Method Drifter-Based Analysis of the Lofoten Basin Eddy

2.1 Introduction

Mesoscale eddies (10–100 km) are ubiquitous features of the ocean, implicated in the general circulation, nutrient and carbon cycles, heat transport, and water mass transformation (Gupta et al., 2022; Bian et al., 2023; Dove and Freilich, 2026; Dong et al., 2025a; Wunsch, 2004). Because they are too small to resolve in most climate models, their effects are typically parameterized as a quasi-homogeneous background turbulence acting on large-scale gradients rather than as coherent vortices (e.g., Gent and Mcwilliams, 1990; Redi, 1982; Hewitt et al., 2020; Marques et al., 2022). Such closures inevitably smooth over the fine-scale energy transfers that are a defining feature of real eddies — not only the eddy–mean flow exchange of energy, momentum, and potential vorticity, but also their interaction with the internal wave field, a pathway that depends on the detailed vorticity structure of individual vortices (Hewitt et al., 2020; Yan et al., 2019; Pearson et al., 2017; Delpech et al., 2024)

It has long been known that mesoscale eddies play a role in shaping the internal wave field. Their local vorticity and strain fields set an effective Coriolis frequency $f_{eff} = f + \zeta/2$ as described by Kunze (1985), where $f = 2\Omega \sin\phi$ is the Coriolis frequency based on Earth's angular velocity Ω and the latitude ϕ, and ζ is the local relative vorticity. In anticyclones, $\zeta < 0$ thus shifts the lower bound of the internal wave band enabling trapping and amplification of energy (Kunze, 1985; Elipot et al., 2010; Conn and Callies, 2026). Numerous observational studies have confirmed that near-inertial oscillations interact sensitively with the mesoscale eddy field, but different analyses emphasize different characteristic vorticity scales - from smoothly varying mesoscale relative vorticity to highly localized submesoscale filaments - raising the question of which scales are actually most relevant for controlling internal wave trapping, phase winding, and dissipation within real mesoscale vortices (Elipot et al., 2010; Park and Watts, 2005; Hilditch et al., 2025; Conn et al., 2024)

Resolving this structure is difficult because eddy scales fall between what ships, moorings, and gliders sample in situ and what satellites capture globally. Altimetry has long tracked eddies

globally (Chelton et al., 2007) but typically only resolves features larger than $\sim$50 km (Ballarotta et al., 2019); even the recent Surface Water and Ocean Topography (SWOT) mission, which sharpens the surface view considerably (Fu et al., 2024; De Marez, 2025), remains surface-limited and temporally sparse. In situ surveys can recover an eddy's three-dimensional structure (Zhang et al., 2024; Thomas et al., 2024; Du et al., 2025), typically using a combination of gliders, moorings and ship based surveys, but are costly and, because eddies typically propagate and deform on the timescale of the observations, demand a Lagrangian approach rather than a static Eulerian one.

This work adopts exactly such a Lagrangian, eddy-following approach, using surface drifters to investigate how near-inertial oscillations interact with the fine-scale vorticity of a long-lived anticyclone, and builds directly on the previous chapter of this dissertation. In Chapter 1, analysis of data from a small 10 piece surface drifter array deployed in the Lofoten Basin Eddy (LBE), a long-lived anticyclone in the Norwegian Sea, established that there were sub-eddy scale variability in near-inertial kinetic energy and that not all the energy observed could be tied to wind forcing. We further proposed a mechanism through which the eddy center undergoing near-inertial oscillations can pump near-inertial energy into the eddy center. What that first, sparser array could only hint at, however, was the spatial structure of that energy within the eddy. This spatial patchiness - together with the strikingly filamented vorticity fields seen in a high-resolution numerical model of the eddy - suggested that the interior of the LBE is far from a smoothly rotating and axisymmetric vortex, and motivated a second, denser drifter deployment designed specifically to resolve sub-eddy scales.

In this chapter we analyze this second array: 28 drifters deployed as six clusters in the LBE during the 2022 Northern Ocean Rapid Surface Evolution (NORSE) cruise. Our aim here is to characterize the fine-scale vorticity structure of the eddy and to determine how its near-inertial field is organized across scales. We approach this with three complementary methods applied to the same drifter data: local velocity gradient estimates from drifter triplets described in section 2.3.1, a gridded stream function decomposition that separates the flow by scale described in 2.3.2,

and a Gaussian Process Regression reconstruction of the eddy-scale vorticity field described in section 2.3.3. We present the results of each of these methods in section 2.4 and in section 2.5 we discuss the presence of fine-scale vorticity structures, evidence of near-inertial wave trapping and patterns of near-inertial kinetic energy as well as the limitations of our study.

2.2 Data

2.2.1 Surface drifters

The data used in this work was collected by an array of Surface Velocity Program (SVP) drifters deployed in the Lofoten Basin Eddy (LBE). The deployment took place during the 2022 cruise of the Northern Ocean Rapid Surface Evolution (NORSE) project funded by the Office of Naval Research (ONR). Figure 2.1a show the location and all drifter sampling points for the first month of deployment. The array consisted of 28 drifters drogued at 15 m sampling at 15 minute intervals. The drifters were all made by the Lagrangian Drifter Lab at Scripps Institution of Oceanography and recorded their position in latitude and longitude as well as the sea surface temperature with an accuracy of about 2.5 m root mean squared (RMS) and ±0.05 K respectively. Two of the drifters were Minimets (Centurioni, 2018; Klenz et al., 2022) that additionally measure wind speed and sea level pressure at about 30 cm above the surface with an accuracy of 2% FS and ±0.4 hPa RMS respectively. The array was deployed as six separate clusters, each containing four to five drifters, in the LBE on November 4^{th} 2022. The approximate center of the LBE was identified with the help of satellite altimetry and shipboard Acoustic Doppler Current Profiler (ADCP) aboard the NRV Nave Alliance (A5345) and the drifter clusters were deployed as separate line arrays with $\sim$200m spacing between individual drifters. One drifter cluster was deployed in the center of the LBE, three clusters were deployed on a 5km radius circle with even azimuthal spacing between clusters, and two clusters were deployed on a 10km radius circle on opposite sides of the eddy. The line arrays were arbitrarily oriented relative to the eddy center based on ship direction.

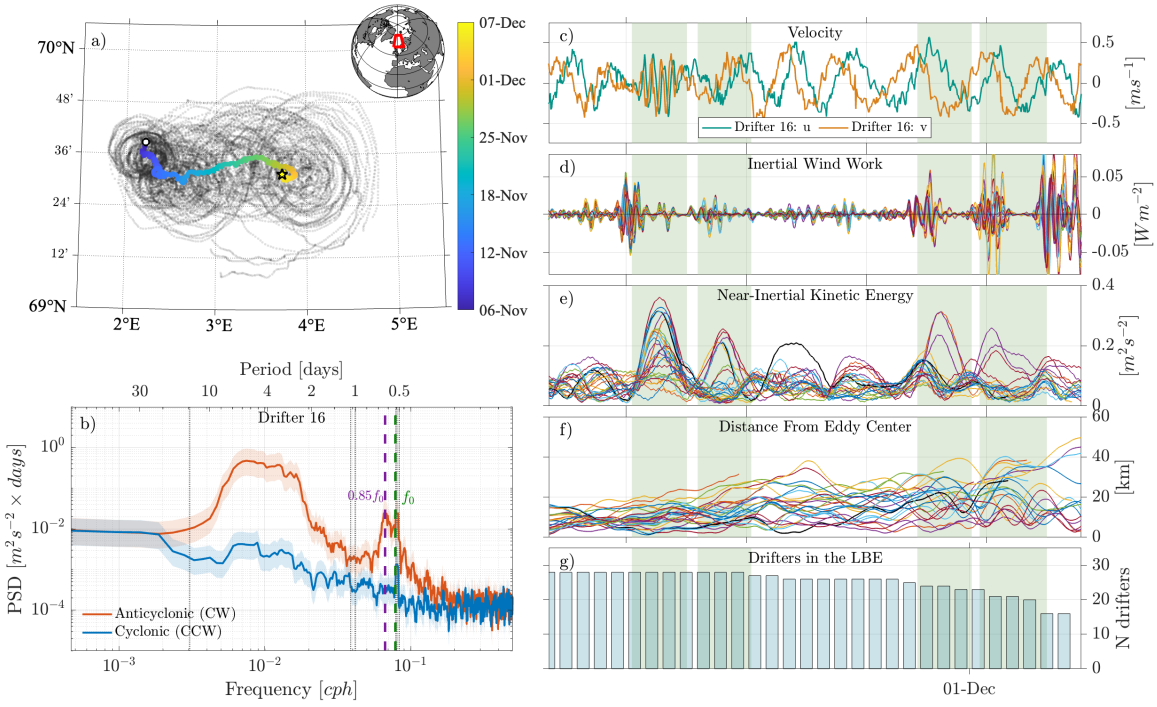


Figure 2.1. a) Map overview of drifter tracks and eddy center location. b) Rotary spectra for drifter 16 with shaded regions being the 95% confidence interval, vertical lines marking tidal frequencies and f and $0.85f$ equivalent to $f_{\text{eff}} = f(1+Ro/2)$ with $Ro \approx -0.3$. c) Time series of zonal and meridional velocity for drifter 16. d) Inertial wind work for all drifters. e) Near-inertial kinetic energy for all drifters. f) Distance from MWRA derived eddy center for all drifters. g) Number of drifters left in the eddy. The shaded background regions indicate "energy events" where at least two drifters display near-inertial kinetic energy higher than 0.2 m^2/s^2.

The drifter data was manually quality controlled by examining each individual drifter trajectory and removing spurious data points due to poor satellite fixes (about 3% of data points in the original 15 minute resolution dataset) which were then linearly interpolated over. Each drifter trajectory was visually examined to identify the time at which the drifter left the eddy by looking at the shape of the trajectory as well as the time series of the velocity. We used a Butterworth filter of 0.7-1.7f_{LBE} where f_{LBE} is an oscillatory frequency corresponding to an eddy period of 4 days, and interpreted a $\sim$4 day oscillatory signal as the drifter still being in the eddy. This was also confirmed using a Multivariate Wavelet Ridge Analysis (MWRA) method that is part of jLab (Lilly, 2024) that also gives an estimate of the eddy center location. This

method is further described in Chapter 1 of this thesis and used in the same way here. We inertially band pass the drifter velocities with a 4th order Butterworth filter of width 0.7-1.2f at latitude 69.5° N, the average latitude of the LBE center. The azimuthal velocity of each drifter can be estimated as $V_a = \mathrm{Re}[(u+iv)e^{i(\pi/2-\theta)}]$ where θ is the angle between the center of the eddy and the drifter position and $u+iv$ is the low passed drifter velocities.

2.2.2 Auxiliary data

Reanalysis winds were used to estimate the wind stress on the LBE. Zonal and meridional winds at 10 m comes from the ERA5 product (Copernicus Climate Change Service, Climate Data Store, 2023) provided by the European Centre for Medium-Range Weather Forecasts (ECMWF) on a 0.25° × 0.25° grid and hourly resolution (Hersbach et al., 2025). We estimate wind stress as $\tau = \rho_a C_d |\mathbf{u}_a - \mathbf{u}_s|(\mathbf{u}_a - \mathbf{u}_s)$ where ρ_a is the surface air density and C_d is the drag coefficient here assumed to be nonlinear following Large and Pond (1981) and corrected for low winds according to Trenberth et al. (1989). $\mathbf{u}_a$ is the 10 m wind and $\mathbf{u}_s$ is the surface currents of the ocean as measured by the drifters. The wind work is then the dot product of the wind stress τ and inertially filtered drifter velocities such that $W = \vec{\tau} \cdot \vec{u}$, which represents the rate of energy input per unit area. We use the in-situ wind from the Minimet drifters to validate the ERA5 and find they agree to within 10% for the month.

2.3 Methods

2.3.1 Kinematics from Lagrangian drifter triplets

Clusters of at least three surface drifters can be used to estimate kinematic properties such as vorticity, divergence, and strain rates in mesoscale eddies (e.g., Molinari and Kirwan, 1975; Okubo and Ebbesmeyer, 1976; Essink et al., 2022; Zeiden et al., 2022). Following Molinari and Kirwan (1975) and Okubo and Ebbesmeyer (1976), we approximate the horizontal velocity field

as locally linear in space and fit it to the observed drifter velocities at each time step using a least squares (LS) estimate. Essink et al. (2022) reports that there is a theoretical increase in accuracy in the estimates of gradient as the number of drifters in a cluster increases but find no functional dependence and report that N = 3, 6 and 9 are only marginally different. In order to maximize the number of observations and the spatial coverage of the LBE we here use drifter triplets, for which the coefficients are exactly determined by the velocity components (six equations for six unknowns). At any given time, the velocity of drifter i is described as

$$u_i = u_0 + a_{xx}(x_i - x_0) + a_{xy}(y_i - y_0), \tag{2.1}$$

$$v_i = v_0 + a_{yx}(x_i - x_0) + a_{yy}(y_i - y_0), \tag{2.2}$$

where (x_i, y_i) are the drifter positions, (u_i, v_i) are the corresponding velocities, and u_0, v_0, a_{xx}, a_{xy}, a_{yx}, a_{yy} are unknown coefficients. The components of the horizontal velocity-gradient tensor are obtained by solving these equations over each non-collinear triplet of drifters at every sampling time. The kinematic properties follow directly:

$$\zeta = a_{yx} - a_{xy}, \tag{2.3}$$

$$\delta = a_{xx} + a_{yy}, \tag{2.4}$$

$$s_n = a_{xx} - a_{yy}, \tag{2.5}$$

$$s_s = a_{xy} + a_{yx}, \tag{2.6}$$

where $\zeta = \partial v/\partial x - \partial u/\partial y$ is the relative vorticity, δ is the horizontal divergence, and s_n and s_s are the normal and shear strain components, respectively, which we use as absolute strain $S = \partial u/\partial y + \partial v/\partial x$.

In principle, with $N = 28$ drifters there are $\binom{28}{3} = 3276$ distinct triplets. However, because the shape and size of drifter clusters strongly affect the quality of kinematic estimates (e.g., Molinari and Kirwan, 1975; Okubo and Ebbesmeyer, 1976; Berta et al., 2016; Essink et al., 2022; Esposito et al., 2021), we limit our analysis to triplets that satisfy geometric quality-control criterion. Specifically, we require (i) a cluster aspect ratio $\lambda = 12\sqrt{3}A/p^2 > 0.7$ where A is the triplet area and p the perimeter following Esposito et al. (2021), and (ii) a maximum separation distance between any two drifters in the triplet of 7.5 km, a limit chosen to represent scales of interest while retaining a sufficient number of triplets. These conditions ensure that cluster length scales remain smaller than or comparable to the local flow scales and that the LS approximation of a locally linear velocity field is appropriate. We thus remove nearly collinear and highly elongated triplets, for which velocity-gradient estimates are poorly conditioned and sensitive to position errors, interpolation uncertainty, and error propagation. For the first month of deployment, from November 6$^{\text{th}}$-December 7$^{\text{th}}$ out of 2,440,620 possible drifter triplets (taking into account when drifters exited the eddy), we retain 16480 triplets (0.7%) that meet the above criteria.

2.3.2 Decomposition of drifter trajectories using a gridded stream function

We attempt to separate out different scale flows in the drifter velocities by fitting a spatio-temporal stream function to the full drifter array, following an approach that generalizes the linear velocity-field decomposition of Oscroft et al. (2020). Whereas their linear method estimates a single, spatially uniform velocity-gradient tensor (strain, vorticity, and divergence) at each time, here the mesoscale is represented by a continuous stream function $\psi(x,y,t)$ that varies smoothly in space and time.

The stream function is expanded on a tensor-product B-spline basis,

$$\psi(x,y,t) = \sum_{i,j,k} c_{ijk} B_i^{(S_q)}(x) B_j^{(S_r)}(y) B_k^{(S_t)}(t), \tag{2.7}$$

where $B^{(S)}$ denotes a B-spline of degree S and $\psi_S = [\,S_q\ S_r\ S_t\,]$ sets the spline degrees in x, y, and t, respectively. The mesoscale velocity is recovered as the curl of the stream function,

$$u_{\text{meso}} = \frac{\partial \psi}{\partial y}, \qquad v_{\text{meso}} = -\frac{\partial \psi}{\partial x}, \tag{2.8}$$

so that the mesoscale flow is non-divergent by construction and continuity is satisfied exactly. The spline coefficients c_{ijk} are estimated by fitting the modeled velocities $(u_{\text{meso}}, v_{\text{meso}})$ jointly to the measured velocities of all drifters simultaneously, with the temporal B-spline (degree S_t) enforcing smooth evolution of the field over the deployment. The total Lagrangian velocity of each drifter is thereby decomposed into three components: a spatially uniform "background" flow $\mathbf{u}_{\text{bg}}(t)$ representing array-wide coherent motion; the mesoscale field $\mathbf{u}_{\text{meso}}(x,y,t)$ of equation 2.7-2.8, evaluated at each drifter's position; and a submesoscale residual $\mathbf{u}_{\text{sm}}$, the remaining spatially differential motion after subtraction of the array coherent and mesoscale components,

$$\mathbf{u}_{\text{sm}}(t) = \mathbf{u}(t) - \mathbf{u}_{\text{bg}}(t) - \mathbf{u}_{\text{meso}}\big(x(t), y(t), t\big). \tag{2.9}$$

The mesoscale field may optionally be constrained with a zero-vorticity and/or a zero-strain condition. For example, under the default (unconstrained) fit the stream function is free to represent rotation; a zero-vorticity constraint instead forces the mesoscale flow to be irrotational (pure strain). Here we use the unconstrained fit (both strain and vorticity) throughout.

The choice of model parameters for ψ_S is non-trivial. Here we use $\psi_S = [\,4\ 4\ 7\,]$, meaning a 4^{th} order spatial fit in x and y and splitting our 30 day time series into 7 temporal segments ($\sim$4 days each). The choice of spatial and temporal orders was made by comparing candidate fits over a range of ψ_S values and the associated mesoscale-submesoscale coherence, at varying degrees of freedom using a bootstrap method. Further details of the model selections can be found in Appendix section 2.7. The ideal model has low coherence between the mesoscale and submesoscale part, indicative of a cleaner separation between the two. Oscroft et al. (2020) also define the diffusivity κ as a measure of spreading caused by the submesoscale component. They

reason that in strain dominated flows the mesoscale component should be responsible for most of the spreading and thus the best model choice also minimizes κ. In the LBE where strain is not dominating we instead focus on keeping the coherence low without letting the degrees of freedom get too high since this is indicative of overfitting. We further check the coherence between the array-coherent and submesoscale components at different frequencies which should also be low for a clean separation. As the mesoscale-submesoscale coherence remained relatively high (0.3-0.5) for all the models we tested we conclude that either our drifter cluster does not have sufficient coverage to map the eddy mesoscale in time, or there is an intrinsic kinematic overlap between the mesoscale and the submesoscale where some level of coherence is to be expected. We cannot clearly separate between these two possibilities with the data we have. For this reason we treat any residual mesoscale signal in the submesoscale component with caution. We do, however, trust that the near-inertial signal in the submesoscale component is real: the coherence between the array-coherent background and the submesoscale is below significance in both the eddy and inertial bands Appendix section 2.7, so the submesoscale near-inertial energy is not simply leakage of the background slab motion. We again note that the moderate mesoscale-submesoscale coherence is specific to the mesoscale-submesoscale pair and discuss in Section 2.5.2 that this may reflect a genuine physical overlap between the two scales rather than a failure of the separation: a near-inertial field embedded within a coherent eddy is not expected to be fully independent of it.

Near-inertial signals were isolated from the horizontal velocity time series using a complex Morse-wavelet ($\gamma = 3$ and $\beta = 25$) at a single scale. Rather than centering the wavelet on the local inertial frequency f, we center it at $0.93f$, the approximate midpoint between the two near-inertial peaks present in the raw drifter spectra: the f peak and the $f_{\text{eff}} \approx 0.85f$ trapping peak (Figure 2.1b). Both lines are of comparable strength in the raw drifter anticyclonic velocities, and a wavelet centered on f noticeably down-weights the f_{eff} line relative to f (Appendix section 2.9); recentering on $0.93f$ balances the passband gain across the two known lines so that the

instantaneous-frequency estimate is not biased toward f by the filter itself. Working on the complex velocity $u+iv$, we retained the clockwise (anticyclonic) rotary component (the near-inertial sense of rotation in the Northern Hemisphere) along with its amplitude envelope. The wavelet transform was applied separately to the raw drifter velocities and the submesoscale velocity decomposition. We then estimate the instantaneous frequency $\omega(t)$ as the time derivative of the phase of the wavelet-filtered analytic signal (the first instantaneous moment; Lilly and Olhede (2010)), smoothed it over one inertial period, and normalized by f to form the dimensionless ratio ω/f, where $\omega/f < 1$ is locally sub-inertial and $\omega/f > 1$ super-inertial. We emphasize that ω/f is an envelope-smoothed instantaneous frequency, not a spectral peak as it tracks the local, time-varying sense of the near-inertial oscillation rather than a shift in the frequency spectrum.

Throughout, we summarize the ω/f distributions as amplitude-squared–weighted conditional densities, binned along the horizontal axis and normalized within each column, to down-weight low-amplitude noise and highlight the frequency of highest near-inertial energy. Binned means are shown with 90% confidence intervals obtained by bootstrapping over the ensemble of drifters (resampling whole trajectories with replacement rather than individual samples), so the uncertainty reflects the effective number of independent realizations rather than the raw sample count.

2.3.3 Gaussian Process Regression

We attempt to reconstruct an Eulerian velocity field from the Lagrangian drifter observations using Gaussian Process Regression (GPR), following the method outlined in Gonçalves et al. (2019), Lodise et al. (2020), and Aravind et al. (2024). GPR is a non-parametric Bayesian interpolation method in which the horizontal velocity components u and v are modeled as Gaussian processes fully specified by a mean function and a covariance function (Rasmussen and Williams, 2006). The u and v components are treated as independent scalar fields; we describe the formulation for u only. Assuming the drifter observations $\mathbf{u}^d$ and the target velocities $\mathbf{u}^t$ are two finite collections of values each following a Gaussian distribution, the multivariate Gaussian

prior distribution is written as

$$\begin{bmatrix} \mathbf{u}^d \\ \mathbf{u}^t \end{bmatrix} \sim \mathcal{N}\left(\begin{bmatrix} \bar{\mathbf{u}}^d \\ \bar{\mathbf{u}}^t \end{bmatrix}, \begin{bmatrix} K^{dd} + \sigma_N^2 \mathbf{I} & K^{dt} \\ (K^{dt})^T & K^{tt} \end{bmatrix} \right), \tag{2.10}$$

where $\bar{\mathbf{u}}^d$ and $\bar{\mathbf{u}}^t$ are the prior mean estimates at the observation and target points, respectively; K^{dd}, K^{tt}, and K^{dt} are the covariance matrices between pairs of observation points, pairs of target points, and observation–target point pairs, respectively; σ_N^2 is the observational noise variance; and $\mathbf{I}$ is the identity matrix. Conditioning this prior on the observations yields the joint Gaussian posterior:

$$\mathbf{u}^t \mid \mathbf{u}^d \sim \mathcal{N}\left(\tilde{\mathbf{u}}^t, \mathrm{cov}(\mathbf{u}^t)\right), \tag{2.11}$$

with posterior mean and covariance

$$\tilde{\mathbf{u}}^t = \bar{\mathbf{u}}^t + (K^{dt})^T \left(K^{dd} + \sigma_N^2 \mathbf{I}\right)^{-1} \left(\mathbf{u}^d - \bar{\mathbf{u}}^d\right), \tag{2.12}$$

$$\mathrm{cov}(\mathbf{u}^t) = K^{tt} - (K^{dt})^T \left(K^{dd} + \sigma_N^2 \mathbf{I}\right)^{-1} K^{dt}. \tag{2.13}$$

As noted by Gonçalves et al. (2019), these expressions are mathematically equivalent to optimal interpolation (Gandin, 1966). The critical distinction is that in GPR the hyperparameters of the covariance function are not prescribed a priori but are determined by maximizing the log marginal likelihood:

$$\log p\left(\mathbf{u}^d \mid \theta\right) = -\frac{1}{2}(\mathbf{u}^d)^T B^{-1} \mathbf{u}^d - \frac{1}{2}\log|B| - \frac{n}{2}\log 2\pi, \tag{2.14}$$

where $B = K^{dd} + \sigma_N^2 \mathbf{I}$, using the L-BFGS-B optimization algorithm (Byrd et al., 1995) implemented in Python using GPy (GPy, 2012). Both the prior means $\bar{\mathbf{u}}^d$ and $\bar{\mathbf{u}}^t$ are set to zero, so the reconstructed field is determined entirely by the covariance function and the regression.

The covariance function was defined as a sum of two anisotropic squared-exponential (RBF) kernels in the space-time coordinate (t, y, x), with independent length scales in each dimension, yielding nine hyperparameters per velocity component following Gonçalves et al. (2019); Lodise et al. (2020).

The GPR was run on three separate time periods November 6-18$^{\text{th}}$, November 18-26$^{\text{th}}$ and November 26 - December 7$^{\text{th}}$ to facilitate the use of an eddy-centered frame despite the approximately 2° (about 70km) eastward translation of the LBE during this time as seen in Figure 2.1a. Drifter positions and velocities were first converted to eddy-relative Cartesian coordinates (x, y) in kilometers by projecting onto a local tangent plane centered on the time-period-mean eddy position. The reconstruction was performed on a regular grid with 1 km spatial resolution and 1 h temporal resolution. From the reconstructed velocity field, the vertical component of relative vorticity was computed as $\zeta = \partial v/\partial x - \partial u/\partial y$ using second-order centered finite differences. The reconstruction performance was assessed against a 25% withheld subset of randomly chosen observations not used in fitting.

Cross-validation against the withheld observations ($N = 4261$ points) yields near-zero bias (≤ 0.5 mm s^{-1} in both u and v), root-mean-square errors of 0.028 m/s (u) and 0.033 m/s (v), correlations of 0.99, and skill scores of 0.98 (see Appendix section 2.8 for definition of skill scores and the full verification process). To restrict the analysis to well-observed regions, we mask grid cells where the GPR posterior standard deviation σ exceeds 0.075 m/s. This is a spatial coverage criterion rather than an accuracy tolerance: because σ grows with distance from the drifters, the mask delimits the approximate core of the eddy where drifter density is higher, and the validated Root Mean Square Error RMSE is less than half the masking value. Verification statistics are insensitive to the precise threshold (skill > 0.97 over 0.01-0.15), so the reconstruction accuracy within the observed core is robust to this choice.

Lastly, to statistically describe the GPR reconstruction we attempt to track the individual vorticity features through time. At each time step we identify contiguous patches whose normalized vorticity (either anticyclonic or cyclonic) exceeds the local mean field strength and identify

the strongest 20% by absolute magnitude. We apply a size filter and only retain features spanning at least four grid cells (4 km^2) that fall inside the $\sigma_{u,v} = 0.075$ m/s trusted region, and follow them frame to frame by spatial overlap. Based on comparison with the other methodologies employed here we impose a minimum patch lifetime of 3 h ($\approx 0.25, T_i$, where $T_i = 12.7$ h is the inertial period at 69.5°N). This yields 180 anticyclonic and 52 cyclonic patches over the record.

2.4 Results

2.4.1 Forcing and energy patterns

Figure 2.1 shows the predominantly eastward translation of the LBE during the month of observation as well as hints at the multiple scales of motions present in the drifter velocity time series. In the rotary decomposed velocity spectra in Figure 2.1b there is a clear anticyclonic spectral peak representing the eddy, as well as a bimodal near-inertial peak at f and $0.85f$ equivalent to $f_{\text{eff}} = f + \zeta/2$ Kunze (1985) with Rossby number $\text{Ro} = \zeta/f = -0.3$. The M2 tidal peak in the cyclonic velocities is very close to f but about one order of magnitude smaller than the anticyclonic (inertial) peak, and thus we attempt no further filtering to remove tides from the drifter velocities. In Figure 2.1c-g we note that there are several times where drifters display elevated levels of near-inertial kinetic energy (as indicated by shaded regions in Figure 2.1) but that the apparent amount of wind work associated with each "energy event" varies. More importantly, in each of these events different drifters have very different levels of near-inertial kinetic energy.

2.4.2 Triplet statistics

The triplet fits provide a statistical view of the eddy. Figure 2.2a show the relationship between near-inertial kinetic energy and relative vorticity where the majority of points fall near $\zeta/f \approx -0.3$ which we take to be the signature of the LBE. We note that there is a wide spread in the level of near-inertial kinetic energy associated with triplet centroids that are within $\sim$15-

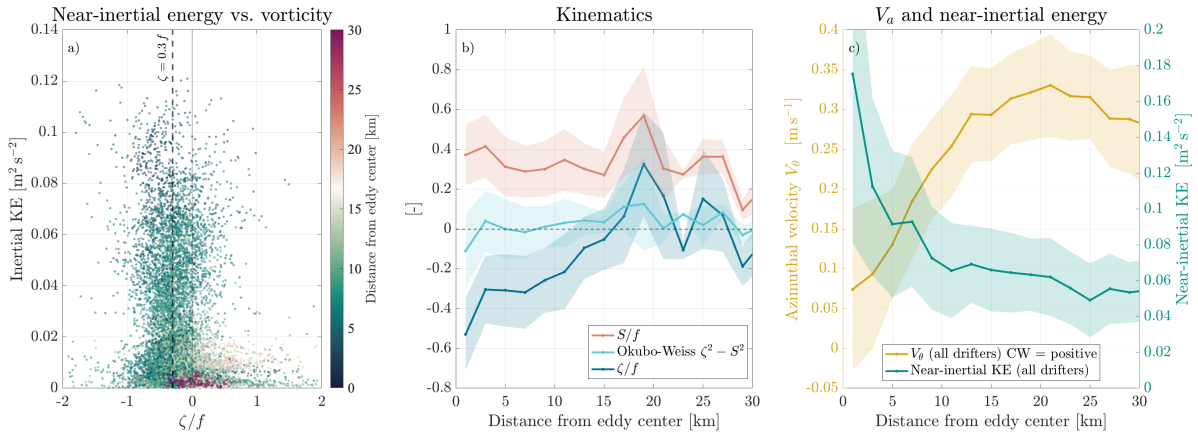


Figure 2.2. a) Triplet near-inertial kinetic energy (average value over three drifters in a triplet) versus vorticity, color is the distance from eddy center to the centroid of the triplet. b) The kinematics derived from the triplet analysis, strain, vorticity and the Okubo-Weiss parameter $\zeta^2 - S^2$. c) Azimuthal velocity V_a (positive clockwise) and near-inertial kinetic energy for all drifters. Shaded regions indicate the mean absolute deviation.

20 km radial distance of the eddy center, and that for points where the radial distance exceeds this the vorticity is predominantly positive. We take this to indicate the presence of cyclonic filaments surrounding the LBE. Further evidence for this can be found in the radial average of the kinematic properties estimated by the triplets. Figure 2.2b show the strain, relative vorticity and the Okubo-Weiss parameter OW $= \zeta^2 - S^2$ in 2km radial bins all normalized by local f. Three indicators converge on a kinematic eddy radius of ∼15-20 km as expressed at the surface: the vorticity is negative in the interior and turns positive near ∼20 km, the strain is elevated over the same band, and the azimuthal velocity V_a (Figure 2.2c, a per-drifter radial average that does not account for drifters exiting the LBE) increases out to ∼15-20 km before declining. Together these delineate a region of enhanced strain and positive vorticity, the cyclonic filaments, surrounding the anticyclonic core. V_a does not increase linearly with radius r, suggesting that the LBE is not strictly in solid-body rotation which requires a constant V_a/r relationship. The near-inertial kinetic energy is clearly elevated in the core of the LBE, but does not drop to zero at the edge of it which suggests there is some background level of inertial energy present. We will return to this point.

2.4.3 Decomposition and instantaneous frequency

The resulting components from the gridded stream function decomposition using the drifter array is shown in Figure 2.3. Both the array-coherent and submesoscale components have near-inertial signals as seen in Figure 2.3e. We compare the instantaneous frequencies ω/f of the inertially filtered raw drifter velocities and of the submesoscale component of the decomposition. Figure 2.4a–b show ω/f versus distance from the eddy center, with weighted density shading and the binned mean with bootstrap confidence intervals. Both are sub-inertial ($\omega/f < 1$) for $r < 20$ km. The raw drifter frequency has a clear radial structure, dipping to $\omega/f \approx 0.85$ in the core and rising toward f near the eddy edge, crossing above f (super-inertial) beyond $\sim$20 km. The submesoscale frequency, by contrast, is sub-inertial throughout ($\omega/f \approx 0.95$) with little radial variation. We confirmed that this sub-inertial submesoscale level is not an artifact of the wavelet estimator: an independent multitaper rotary spectrum of the raw submesoscale velocity (no wavelet, following the method used for Figure 2.1b) places the anticyclonic near-inertial peak at $\omega/f \approx 0.95$, consistent with the envelope-smoothed instantaneous frequency. The submesoscale near-inertial motion is therefore genuinely slightly sub-inertial rather than pinned to f.

Figure 2.4c-e show the instantaneous frequency shift $\Delta\omega/f$ plotted against normalized relative vorticity ζ/f, using three independent vorticity estimates. In each panel the solid grey line marks the Kunze (1985) relation ($\Delta\omega = \frac{1}{2}\zeta$) and the dash-dotted line the global approximate $0.4\,\zeta$ slope of Conn and Callies (2026), both pivoting through the origin at the f null. Panel 2.4c pairs the drifter near-inertial frequency with the total vorticity from the GPR velocity field interpolated onto drifter locations; the binned mean and weighted fit rise gently across the axis (slope $+0.12$, $r = +0.31$ at the 7 km coarse-graining scale used for the fit; see Section 2.5.2), lying well below the Kunze and Conn slopes. Panel 2.4d pairs the submesoscale decomposition instantaneous frequency with the mesoscale vorticity from the stream function fit and is flat (slope -0.02, $r = -0.07$), with sparse, wide-error bins at high ζ. Panel 2.4e uses the drifter

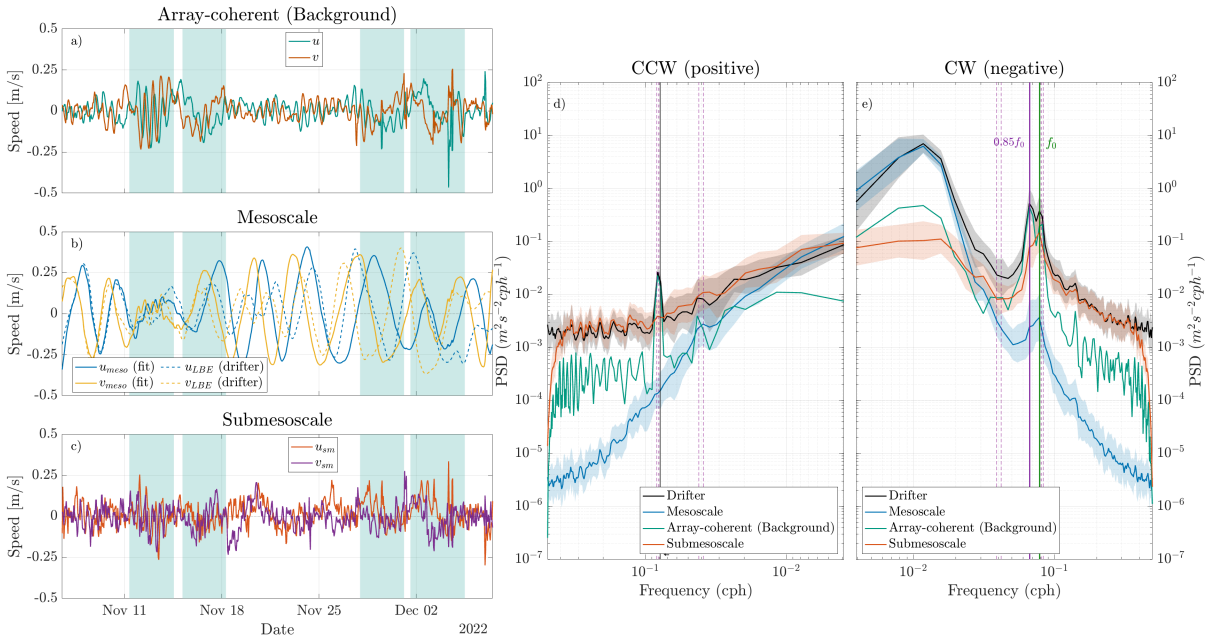


Figure 2.3. Results of the decomposition, a) array-coherent *u* and *v* velocity (same for whole array), b) mesoscale *u* and *v* velocity and low passed velocity for drifter number 16, the same drifter as shown in Figure 2.1, c) submesoscale *u* and *v* velocity for the same drifter. d) and e) rotary decomposed spectra for the components shown in a-c). The shaded error bars show the mean and range for all drifters in the array, the array-coherent component is lacking an average error shading since it is a single time series for the whole array.

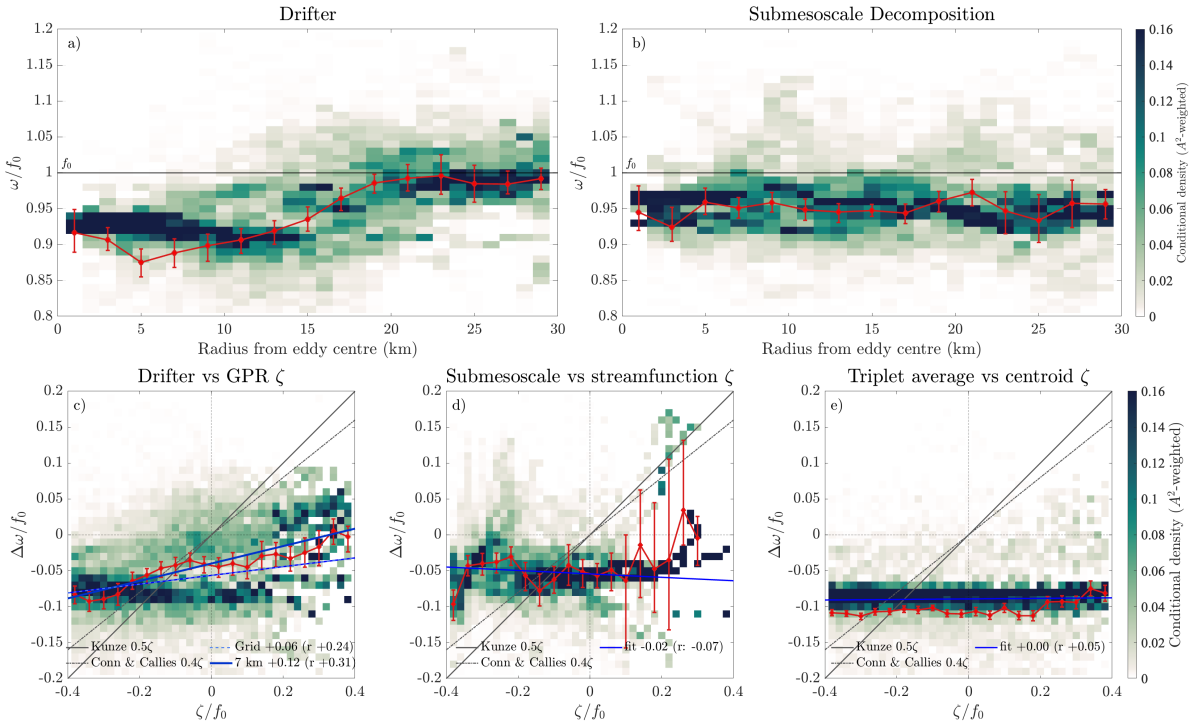


Figure 2.4. Instantaneous near-inertial (NI) frequency. In all panels the shading is an amplitude-squared-weighted conditional density, normalized within each column of the horizontal axis; the red curve is the binned mean with a 90% confidence interval. a) ω/f against radius from the eddy center for NI-filtered drifter velocities; the horizontal line marks $\omega = f$. b) As in a), but for the submesoscale component from the stream function decomposition. c–e) Frequency shift $\Delta\omega/f = \omega/f - 1$ against normalized relative vorticity ζ/f, with all reference lines pivoting through the origin at the f null. The solid grey line is the Kunze relation ($\Delta\omega = \frac{1}{2}\zeta$, slope 0.5) and the dash-dotted line the global slope of 0.4ζ reported by Conn and Callies (2026). c) Raw NI frequency paired with the total vorticity from the GPR velocity field; annotations give the amplitude-squared-weighted least-squares slope and correlation for the native grid and for the field coarse-grained to 7 km, the scale used for the blue fit. d) Submesoscale NI frequency paired with the mesoscale vorticity from the stream function fit. e) Mean NI frequency of the three members of each drifter triplet paired with the triplet's centroid vorticity, a decomposition-free estimate. In c) and d) the binned means and confidence intervals are obtained by bootstrapping over the ensemble of drifters (resampling whole trajectories); in e) they are obtained by bootstrapping over the ensemble of triplet realizations. The blue line in the bottom row is the amplitude-squared-weighted least-squares fit.

triplets and pairs the triplet-mean frequency with the triplet centroid vorticity; it is likewise flat (slope $+0.00$, $r = +0.05$) and sits near $\omega/f \approx 0.95$.

2.4.4 Gaussian Process Regression

Snapshots of vorticity from the Gaussian Process Regression for a few time points are shown with the associated posterior variance in Figure 2.5 which also shows the location of the drifters used in the reconstruction at that time. The reconstruction is most reliable in the interior and close to drifters but the error threshold of 0.075 m/s (solid contour in the bottom row of Figure 2.5) encloses the eddy center at all times. The vorticity reconstruction is not homogeneous in the eddy. Instead the reconstruction suggests there are vorticity "patches" of both stronger and weaker vorticity present in the LBE. There are also areas of cyclonic vorticity at various distances from the eddy center at different times. Figure 2.5b and d show cyclonic patches at approximately 20 km distance from the eddy center that also appear slightly stretched. These are consistent with the cyclonic filaments surrounding the eddy discussed in Section 2.5.1. In Figure 2.5a and c there are small cyclonic patches at about 10 km distance from the eddy center.

To assess how much of the vorticity structure depends on the estimation method, we compare the GPR field with our kinematics from drifter triplets and the gridded stream function fit. Figure 2.6 show the vorticity estimated by each method for three different times and zoomed in on particular patches of alternating vorticity. The GPR reconstruction and drifter triplets, which make no smoothness assumption beyond their respective fits, both resolve coherent small-scale features, including localized patches of enhanced and reversed vorticity across the three times. The gridded streamfunction, constrained to a smooth, non-divergent representation, recovers a consistent overall vorticity gradient but only hints at these smaller features. That two independent estimators agree on the presence and location of fine-scale structure indicates that it is a genuine feature of the flow within the eddy rather than a product of any single method.

Figure 2.7a show the distribution of tracked vorticity patches. Anticyclonic patches cluster near the eddy core, whereas cyclonic patches are predominantly found closer to the

eddy edge, with the exception of a few short lived cyclonic patches at 10-15 km radius. The median life time of either kind of vorticity patch is about 5 hours and only a few patches exist longer than one inertial period indicating that the fine-scale vorticity field is continually reorganized on sub-inertial timescales. The time-mean radial structure of the eddy derived from the GPR reconstruction is show in Figure 2.7b and looks broadly similar to what the drifter triplet equivalent in Figure 2.2b-c suggests. The GPR reconstruction captures the elevated near-inertial kinetic energy in the eddy center and a normalized relative vorticity at the eddy core of about -0.4. However, where the triplet analysis suggests the presence of cyclonic vorticity and elevated strain at the edge of the eddy at $\sim$20km, the GPR suggests smooth ζ and S profiles with the GPR derived eddy edge sitting at about 35 km which is where the normalized ζ profile goes from negative to positive.

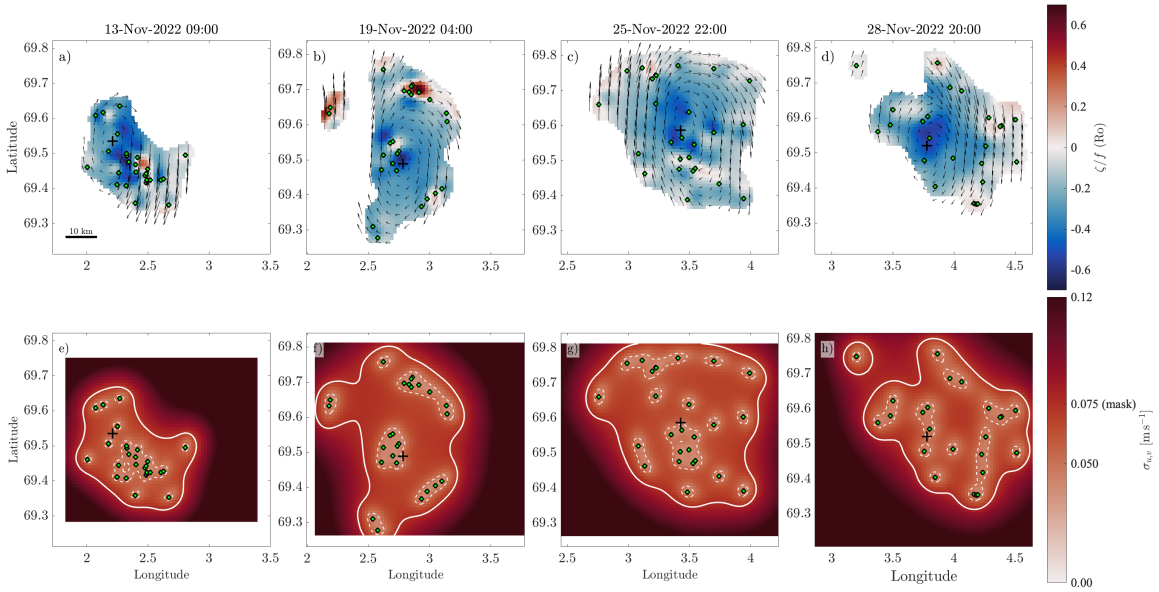


Figure 2.5. Top row a-d) Snapshots of reconstructed velocity fields (arrows) with computed normalized relative vorticity (Ro) and drifter locations (green dots), black + marks the center of the eddy as defined by the minimum value of the stream function. Bottom row e-h), corresponding GPR posterior predictive uncertainty, shown as the mean velocity standard deviation $\sigma_{u,v}$ m/s. White contours mark the $\sigma_{u,v}$ = 0.06 m.s level, where verification coverage saturates (dashed), and the $\sigma_{u,v}$ = 0.075 m/s masking level used throughout (solid). Color bars are shared per row.

2.5 Discussion

2.5.1 Fine-scale vorticity structures

None of the three methods used here, drifter triplets, a Gaussian Process Regression and the gridded stream function fit, describe the Lofoten Basin Eddy as a smoothly rotating, azimuthally symmetric vortex. Instead both the drifter triplets and the GPR reconstruction independently resolve fine-scale patches of enhanced and reversed relative vorticity embedded within the anticyclonic core flow. As these two methods in particular share no smoothness assumption beyond their respective fits, and taking into account the fact that the smooth non-divergent stream-function representation also hints at the same features, we interpret the sub-eddy vorticity patches as being a genuine property of the flow rather than an artifact of a single mapping choice. This adds to a growing recognition that mesoscale eddies are not laterally homogeneous but are permeated by submesoscale vorticity, strain, and divergence anomalies, particularly around their peripheries (McWilliams, 2016; Ernst et al., 2023; Nardelli, 2013).

The vorticity patches are also radially organized with cyclonic features being more common near the edge of the eddy. Cyclonic filaments encircling an anticyclonic core is a commonly observed feature sometimes referred to as a "shielded" vortex (Valcke and Verron, 1997; Carton, 2001) and has been described in the LBE before by Bosse et al. (2019). The shield is not merely a passive kinematic feature: the peripheral cyclonic vorticity arises to balance the potential vorticity of the anticyclonic core, and both idealized experiments and LBE-specific studies indicate that such opposite-signed rings can influence eddy stability and interactions with neighboring vortices (Valcke and Verron, 1997; Gordeeva et al., 2021). More recently, glider observations from the Lofoten Basin suggest that these peripheral regions can be sites of enhanced submesoscale vertical exchange, expressed as narrow warm rings around mesoscale eddies that can raise the sea surface temperature up to 0.4°C, and that such submesoscale heat transport could represent the primary mechanism for substantial heat loss from Atlantic Water in the Lofoten Basin (Dong et al., 2025b).

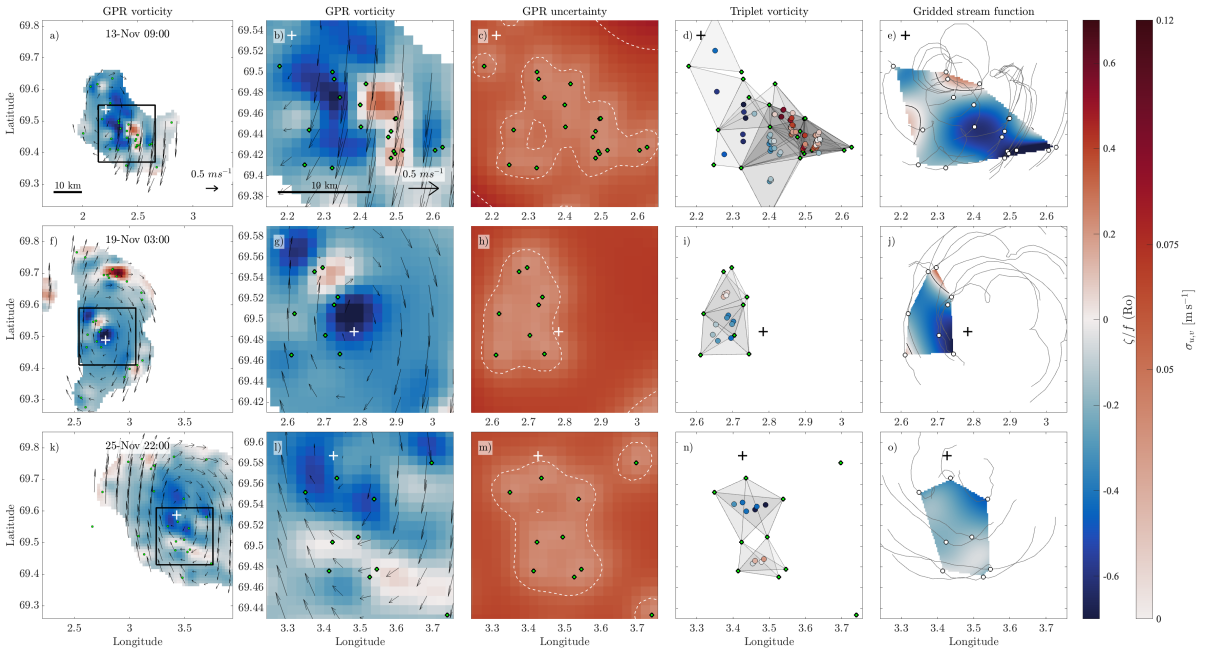


Figure 2.6. Comparison of three vorticity estimators within the Lofoten Basin Eddy at three representative times (rows: 13 Nov 09:00, 19 Nov 03:00, 25 Nov 22:00 2022). a, f, k) Full-domain GPR relative vorticity ζ/f with velocity vectors; the black box marks the zoomed region shown in the remaining columns. b, g, l) GPR vorticity within the zoom window. c, h, m) GPR velocity uncertainty $\sigma_{u,v}$ over the same window; the dashed white contour marks $\sigma_{u,v}$ = 0.05 m/s, and green markers show drifter positions. d, i, n) Vorticity from drifter triplets, with triangles indicating the drifter triplets used and centroids colored by their estimated ζ/f. e, j, o) Relative vorticity from a gridded stream function fit to the drifter cluster, with grey lines showing drifter trajectories over the fit window and white markers their positions at the snapshot time. Vorticity in all panels shares the color bar at right ζ/f; the black/white cross marks the eddy center.

A defining characteristic of the features we observe here is that they are short-lived. The median lifetime of an observed patch is about 5 hours and only a small subset of the observed patches survive longer than an inertial period ($T_i = 12.7$ hours). The fine-scale field within the LBE is thus continually reorganized on sub-inertial timescales. We emphasize that these lifetimes are relative to our detection choices of a per-timestep strength percentile threshold and the $\sigma_{u,v}$ = 0.075 m/s uncertainty mask, and should thus be read as a scale of persistence rather than absolute measurements. Still, the qualitative result is robust across methods: the small-scale structure exists, is spatially organized relative to the eddy, and evolves rapidly.

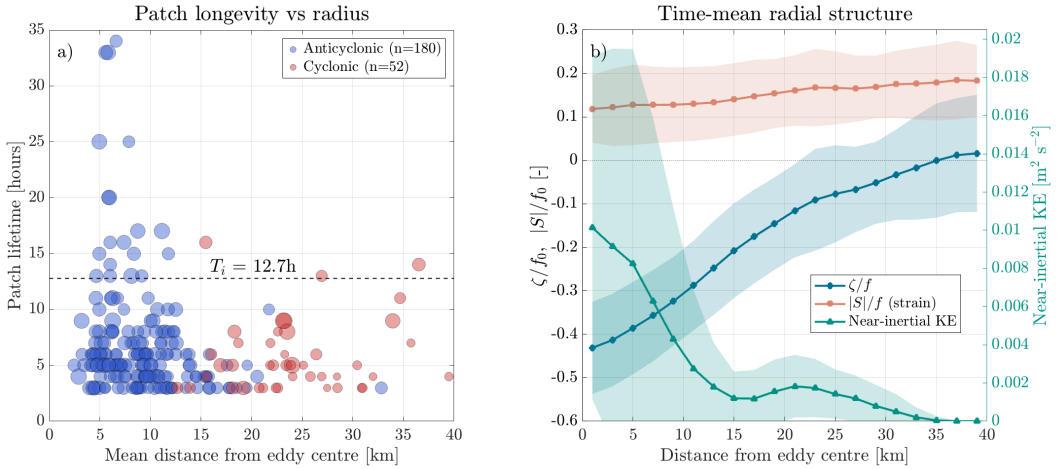


Figure 2.7. a) Vorticity patches tracked in the GPR reconstruction mapped by longevity (y-axis) and mean distance from the eddy center (x-axis), blue/red signifies anticyclonic/cyclonic patches. The size of the marker is proportional to the maximum strength of ζ/f of the patch. b) Time-mean radial profiles of strain, relative vorticity ζ and near-inertial kinetic energy as derived from the GPR reconstruction.

2.5.2 Near-inertial trapping

The near-inertial motions observed inside the LBE bear the signature of trapping in an anticyclone. Kunze (1985) showed using ray tracing that in the presence of a geostrophic flow the inertial frequency is shifted to the effective Coriolis frequency $f_{\text{eff}} = f + \zeta/2$, such that near-inertial waves in regions of anticyclonic (negative) vorticity oscillate below f and become horizontally trapped where $f_{\text{eff}} < f$. Such sub-inertial trapping in anticyclones has been documented repeatedly in observations and models (Thomas et al., 2024).

Figure 2.1b shows the rotary spectrum of an individual drifter having a distinct f_{eff} peak near $0.85f$, a clear indication of trapping in an anticyclone with $Ro \approx 0.3$. The array-coherent "background" part of the gridded stream function decomposition in Figure 2.3e, similarly shows a bi-modal near-inertial peak at f and $0.85f$ which we interpret as the frequency of the near-inertial oscillations of the background slab that contains all drifters and suggests the trapping. The instantaneous frequency of the drifters versus distance from the eddy center carries the same signal: the radius-binned, time-mean frequency is sub-inertial throughout the eddy interior

($\omega/f < 1$ for $r < 20$ km), dipping to $\omega/f \approx 0.9$ in the core and relaxing toward f near the eddy edge before approaching f beyond $\sim$20 km (Figure 2.4a-b). The lower envelope of the ensemble reaches $\omega/f \approx 0.85$ at $r < 15$km, comparable to the spectral f_{eff} line. The frequency shift toward f_{eff} in the core is therefore expressed not only in the individual-drifter spectrum but in the radial mean itself, and its relaxation toward f at the eddy edge ties the shift directly to the presence of the coherent eddy.

Figure 2.4b shows that if the coherent eddy (the mesoscale part of the stream function decomposition) is removed, the submesoscale instantaneous frequency loses the radial structure seen in the raw drifter frequency and settles at a nearly uniform sub-inertial value ($\omega/f \approx 0.95$). We read this to be consistent with trapping of internal waves and nonlinear dynamics at play. First, the radial organization of the frequency shift, sub-inertial in the core, relaxing toward f at the edge, lives in the raw and mesoscale-containing signal, which is what one expects if the coherent swirl of the eddy is what imposes the f_{eff} shift in a bulk sense and traps waves. Second, and importantly, removing the mesoscale does not return the submesoscale to f: the residual near-inertial field remains sub-inertial at $\approx 0.95f$. We do not interpret this as a failed separation. Rather, it is consistent with the moderate mesoscale-submesoscale coherence (0.3-0.5; Section 2.3.2, Appendix section 2.7) reflecting a real physical overlap: a near-inertial field that lives inside a trapping anticyclone is not expected to be spectrally independent of it, and so carries part of the f_{eff} character of its "host eddy" even after the smooth mesoscale flow is subtracted. Another way to consider this is that the processes here described are inherently nonlinear and so performing a linear decomposition can never fully represent the complete dynamics. The submesoscale frequency does not track the local eddy: it is invariant to radius, to the timing of high-energy events, and to which drifters are energetically peaking (all within the $0.023, f$ spectral resolution). The eddy imprints the f_{eff} shift on the raw, mesoscale-containing field as a radially organized depression of f; once the mesoscale is removed, the residual retains a slightly sub-inertial value ($\approx 0.95f$) but loses that radial organization, indicating its frequency is set largely independently of the local eddy vorticity rather than by in-core trapping.

Aware of the limitations of each of our vorticity estimates, from the GPR, from the gridded stream function fit and from drifter triplets, we attempt to quantify the magnitude of the f_{eff} shift by plotting the instantaneous frequency against the relative vorticity. Figure 2.4c show the instantaneous frequency of the near-inertially filtered drifter velocities against the GPR derived vorticity. After careful consideration of noise floors and scales tests, we choose to interpret the GPR field only at scales coarser than its native 1km grid because the reconstruction is a smooth, dynamically constrained fit whose fine-scale structure is unconstrained by the drifter sampling. Both the slope and correlation rise coherently with coarse-graining length up to $\sim$7-10 km before the correlation collapses at larger scales, the signature of a genuine signal rather than an artifact. Regressing ω/f on the coarse-grained GPR vorticity (7km) yields a positive slope of $0.10\,\zeta$ (Figure 2.4c). The near-zero and cyclonic side of the panel is flatter and more sparsely sampled, so that the density of points can give the impression of two horizontal bands; a regression restricted to the anticyclonic core, however, confirms that the slope there is real and is not merely an artifact of connecting two clusters. This eddy-scale slope is below the $0.5\,\zeta$ of Kunze (1985), and also below other more recent estimates of this shift as reported in Conn and Callies (2026) ($\approx 0.4\,\zeta$) or Elipot et al. (2010) ($\approx 0.39\,\zeta/f$). With the inherent uncertainty in the vorticity estimate we are however cautious in our interpretation of exact numbers and stress that Figure 2.4c is not an independent confirmation of the Kunze (1985) relation but a re-expression of the same bulk-radial trapping seen in Figure 2.4a on a vorticity axis.

The instantaneous local field tells a different story than the full drifter velocities do. The mesoscale stream function vorticity, the smooth large-scale part removed to isolate the submesoscale residual, is essentially flat ($-0.02\,\zeta$, $r \approx 0.07$; Figure 2.4d), as expected for a field with little dynamic range. More tellingly, using the drifter triplet estimate of instantaneous local vorticity for triplets where drifters are at most 7.5 km apart and averaging the three drifters instantaneous frequency reveals essentially no relationship between ω and ζ ($0.00\,\zeta$, $r = 0.05$). Notably ω/f stays sub-inertial even for triplets suggesting $\zeta > 0$, likely due to these triplets sampling cyclonic patches inside the anticyclonic field rather than cyclonic features at the

eddy edge. Because panels c and e of Figure 2.4 sample the same physical scale but differ only in operator - panel c coarse-grains the coherent reconstruction while panel e differences instantaneous positions to estimate ζ - their disagreement cannot be a resolution effect. We interpret this as the near-inertial frequency tracking the coherent, time-integrated eddy but being indifferent to the instantaneous local vorticity at the same scale.

This division is consistent with the statistical properties of the vorticity patches. They are intense but short-lived, with a median lifetime of ~ 5 h, far shorter than the local inertial period $T_i = 12.7$ h. A patch that reorganizes faster than a wave completes one inertial oscillation cannot durably shift its frequency, so the near-inertial field integrates over the coherent eddy while averaging out the fluctuating local field. The eddy imprints its frequency as a bulk container, not through the transient vorticity extrema we've shown are embedded within it.

2.5.3 Patterns of near-inertial kinetic energy

As seen in Chapter 1 of this thesis the near-inertial kinetic energy within the LBE is neither steady nor spatially uniform. Figure 2.1d-e shows several discrete energy events during which the near-inertial field intensifies across the array, but two features of these events diverge from simple wind-driven interpretation. First, the inertial wind work associated with each event varies considerably and the largest bursts of near-inertial kinetic energy do not consistently coincide with the largest wind work. Second, during any single event the drifters register very different levels of near-inertial kinetic energy, despite sampling the same eddy over separations of only a few to tens of kilometers. Local wind forcing alone, which is smooth on the scale of the drifter array (the ERA5 field and the in situ Minimet winds agree to within 10%), cannot by itself produce this drifter-to-drifter spread.

Part of the explanation is that several distinct near-inertial signals coexist within the eddy, superimposed across a range of scales. In this work we have applied three different methods to disentangle these signals in space and time, each with their individual advantages and disadvantages. The gridded stream function decomposition affords a first pass att separating

the spatial scales. At the largest scale is the near-inertial motion of the eddy as a whole seen in the array-coherent flow in Figure 2.3a and e, including the oscillation of the eddy center that we linked in Chapter 1 to a pressure-work energy source near the eddy center. At the mesoscale is the coherent anticyclonic swirl, which we discussed in section 2.5.2 in a bulk sense traps and retains near-inertial energy and depresses the frequency toward f_{eff}. From our drifter triplet and GPR analysis we identify cyclonic filaments at the eddy edge as part of this mesoscale structure. Superimposed on these is the more chaotic submesoscale field, which the decomposition shows also carries a near-inertial signal (Figure 2.3e) and which we speculate might be tied to the submesoscale transient vorticity patches seen in the GPR reconstruction and discussed in section 2.5.1. If so, the elevated near-inertial energy in the core (Figure 2.2c, 2.7b), its preference for anticyclonic vorticity, and its non-zero background level at the eddy edge are all consistent with this layered picture in which energy delivered to the core is retained by the trapping swirl while the submesoscale field redistributes it on smaller scales.

We reiterate the point made in Chapter 1 that a coherent eddy is a dynamically rich environment capable of a wide range of behaviors beyond steady, axisymmetric rotation. From eddy modes (Young, 1986) to vortex Rossby waves (Nardelli, 2013; Kar et al., 2025), eddies are rarely steady. Recent modeling work suggest that anticyclones can support trapped near-inertial eigenmodes whose spatial structure and slow modulation are intrinsic to the vortex rather than imposed by the wind (Kafiabad et al., 2021). It has also been shown that submesoscale vorticity filaments and features can refract near-inertial waves and set the length scales that control their vertical radiation (Hilditch et al., 2025).

We do not attempt to isolate these individual mechanisms from surface drifters alone, but their collective relevance reinforces the central interpretation and conclusion of this work: the near-inertial energy signature we observe reflects the eddy acting as a structured, dynamically active energy reservoir across scales, not a passive recipient of wind forcing.

2.5.4 Limitations and future work

A clear limitation of the surface drifter approach to understanding eddy dynamics is that it resolves the horizontal near-inertial velocity field but says nothing directly about vertical velocity or the fate of trapped energy at depth. This matters because the vertical dimension is where much of the dynamical significance of near-inertial-eddy interaction resides: once trapped, a near-inertial wave propagates downward toward a critical layer near the base of the anticyclone, where its vertical group velocity vanishes, its shear intensifies, and its energy is ultimately dissipated (Kunze, 1985). Our observations capture the surface signature of trapping but not this downward radiation. That the two are linked at fine scales comparable to the LBE was demonstrated recently by Rolland et al. (2026), who used in situ profiling inside a 12.8 km radius Mediterranean anticyclone (Rossby number ≈ 0.5) to show that such a fine scale eddy traps near-inertial waves and drives a downward near-inertial kinetic energy flux of up to 5.1 mW m^{-2} below the pycnocline - roughly 20% of the wind power input into inertial motions - while elevating turbulent dissipation to several $\times 10^{-8}$ Wkg^{-1}. Although that eddy sits at a lower latitude (f is some 30% smaller than at the LBE) and in a basin with a smaller deformation radius, the trapping it documents is governed by the relative vorticity ζ/f rather than by f itself, and its host anticyclone occupies the same fine-scale, moderately nonlinear regime ($Ro \sim 0.5$) as the LBE core. The magnitude of any vertical flux in the LBE would depend on its own stratification and wind history, but the mechanism carries over. If the trapping we infer from drifters at the surface behaves similarly at depth to the eddy Rolland et al. describes, the LBE could represent a comparable conduit for near-inertial energy into the stratified interior, with the associated turbulence and vertical exchange carrying potential consequences for the vertical redistribution of nutrients and tracers. Preliminary fastCTD sections collected near the time of deployment show mixed-layer-depth undulations with horizontal scales of a few kilometers, broadly consistent with the submesoscale variability inferred here, though their wave nature and any Doppler shift remain to be quantified.

Ultimately, confirming the downward radiation and dissipation inferred here would require sustained subsurface sampling with co-located microstructure profiles and subsurface velocity/shear measurements capable of tracking near-inertial energy from the mixed layer to the critical layer near the eddy base. Such measurements are logistically demanding and, crucially, difficult to keep referenced to a fine-scale eddy that is itself translating and evolving. Mapping out the vertical dimension is the natural next step, but the Lagrangian surface perspective employed here is still a powerful tool for characterizing wave-eddy interaction.

2.6 Conclusion

Using an array of 28 surface drifters deployed in the Lofoten Basin Eddy and three complementary analysis methods - drifter-triplet kinematics, a gridded stream function decomposition, and a Gaussian Process Regression reconstruction - we characterized the fine-scale vorticity structure of a long-lived anticyclone and how its near-inertial field is organized across scales. The eddy is not a smoothly rotating, axisymmetric vortex but is permeated by intense but short-lived ($\sim$ 5 h) sub-eddy scale vorticity patches, radially organized with cyclonic filaments encircling the anticyclonic core. Its near-inertial motions bear a clear signature of trapping, oscillating below f throughout the interior and relaxing toward f at the eddy edge. Crucially, this frequency shift tracks the coherent, time-integrated eddy but is indifferent to the instantaneous local vorticity at the same scale: patches that reorganize faster than an inertial period cannot durably shift the wave frequency, thus the eddy traps near-inertial energy as a bulk container rather than through its transient extrema. The near-inertial energy we observe is correspondingly multi-scale and not a passive response to wind forcing. Resolving the vertical structure and fate of this trapped energy is the natural next step, but the eddy-following surface perspective already isolates which scales of vorticity control near-inertial trapping in a real, filamented anticyclone.

Acknowledgments

This material is in part a reprint of a manuscript being prepared for publication as Sub-Inertial Trapping and Sub-Eddy Vorticity in an Anticyclone: A Multi-Method Drifter Analysis of the Lofoten Basin Eddy. Bergentz, Kerstin A.; Early, Jeffrey, MacKinnon, Jennifer A., Centurioni, Luca R. The dissertation author was the primary investigator and author of this material. The author wishes to thank Jonathan Lilly for many helpful discussions about eddies and analysis methods.

2.7 Appendix A: Choice of decomposition model

The mesoscale stream function is represented by a tensor-product B-spline of spatial orders S_q, S_r and temporal order S_t, denoted $\psi_S = [S_q\ S_r\ S_t]$. Increasing these orders adds degrees of freedom (DOF) to the fit, allowing the mesoscale to absorb progressively finer structure. To choose an appropriate complexity we tried 57 different ψ_S under the unconstrained (free vorticity and strain) fit, and for each candidate evaluated the mesoscale-submesoscale coherence, κ, number of degrees of freedom and the coherence between the submesoscale and array-coherent components in the eddy band and the inertial band. In the latter case we want to be sure there is no leakage of the background into the submesoscale or vice versa and note that the coherence is below significance with a 95% confidence interval at all times and we thus trust the separation. The full results of the model sweep can be found in Table 2.2 and visualized in Figure 2.8. The coherence is largest at the coarsest fits and decreases as spatial order is increased (≈ 0.51 at 4×4 and ≈ 0.50 at 5×5). We adopt $\psi_S = [4\ 4\ 7]$ (DOF $= 192$, full-fit coherence $= 0.424$).

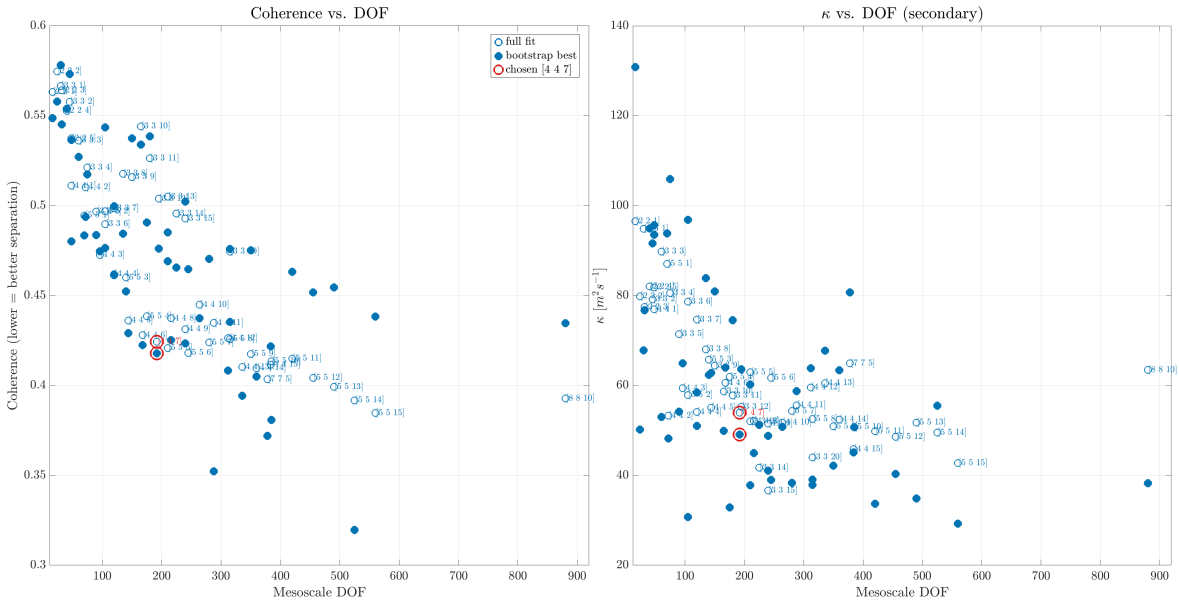


Figure 2.8. Gridded stream function model selection. Left: mesoscale-submesoscale coherence vs degrees of freedom, right: submesoscale diffusivity κ vs degrees of freedom. The final model choice is highlighted in red.

2.8 Appendix B: Gaussian Process Regression evaluation

The Gaussian Process Regression reconstruction performance was assessed against the 25% of drifter observations withheld from the fit. The withheld velocities were compared against the GPR posterior mean interpolated (linearly in t, y, x) to the withheld observation locations, after applying the posterior-uncertainty mask.

For each velocity component we report the bias $\overline{\Delta u} = \overline{u^{\mathrm{GPR}} - u^{\mathrm{obs}}}$, the root-mean-square error $\mathrm{RMSE} = \left[\overline{(u^{\mathrm{GPR}} - u^{\mathrm{obs}})^2}\right]^{1/2}$, the Pearson correlation coefficient r between reconstructed and observed values, and the skill score

$$\mathrm{SS} = 1 - \frac{\overline{(u^{\mathrm{GPR}} - u^{\mathrm{obs}})^2}}{\mathrm{Var}(u^{\mathrm{obs}})}, \tag{2.15}$$

where overbars denote averages over the withheld set (Murphy, 1988). The skill score compares the reconstruction against a reference prediction equal to the mean of the observations: $\mathrm{SS} = 1$ indicates a perfect reconstruction, $\mathrm{SS} = 0$ indicates performance no better than predicting

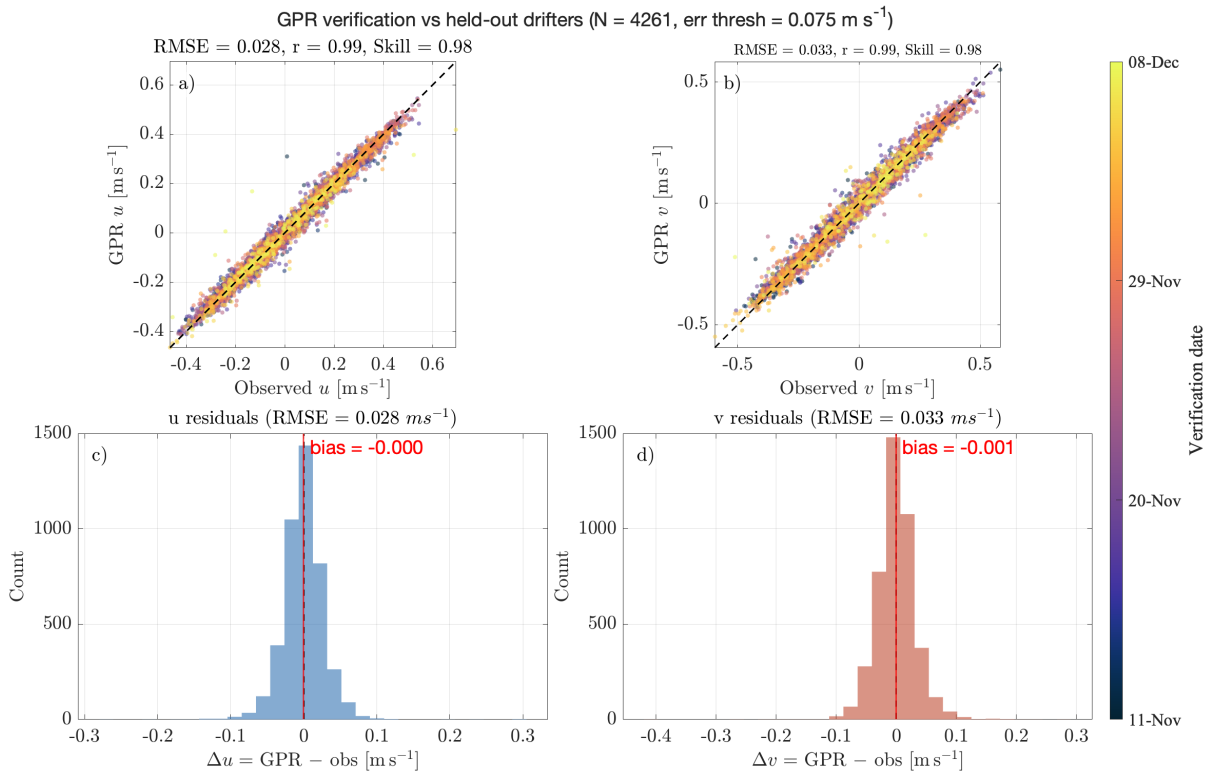


Figure 2.9. Verification of the GPR velocity reconstruction against the 25% of drifter observations withheld from the fit, pooled across all three reconstruction periods ($N = 4261$). (a, b) Reconstructed versus observed (a) zonal u and (b) meridional v velocity, colored by verification date; the dashed line is the 1:1 relationship. Panel titles report the root-mean-square error, correlation r, and skill score [Eq. (2.15)]. (c, d) Distributions of the residuals $\Delta u, \Delta v = u^{\mathrm{GPR}} - u^{\mathrm{obs}}$; the black dashed line marks zero and the red line marks the mean (bias). All quantities use the posterior-uncertainty mask ($\sigma \leq 0.075$ m s^{-1}) applied in the main analysis. The near-zero bias, RMSE well below the eddy swirl speed, and skill scores of ≈ 0.98 indicate that the reconstruction reproduces the observed velocity field with high fidelity.

the mean flow everywhere, and SS < 0 indicates a reconstruction worse than the mean. Unlike r, which measures only the linear association between predicted and observed values, the skill score additionally penalizes errors in bias and amplitude, so a value of SS close to r^2 together with negligible bias indicates that the reconstruction reproduces both the spatial pattern and the magnitude of the observed field.

The statistics ($N = 4261$) are $\overline{\Delta u} = -0.0005$ m s^{-1}, $\overline{\Delta v} = -0.0005$ m s^{-1}; $\mathrm{RMSE}_u = 0.028$ m s^{-1}, $\mathrm{RMSE}_v = 0.033$ m s^{-1}; $r_u = 0.991$, $r_v = 0.988$; and $\mathrm{SS}_u = 0.982$, $\mathrm{SS}_v = 0.977$. Relative to the eddy speeds of $O(0.2 - 0.4$ m s$^{-1})$, the RMSE is roughly 7-15% of the signal

amplitude, the near-zero bias confirms the absence of a systematic offset, and the skill scores indicate that the reconstruction explains $\gtrsim 98\%$ of the error variance of a mean-flow reference. The residual distributions (Figure 2.9c,d) are symmetric and centered on zero, consistent with random rather than systematic error.

The posterior standard deviation σ has a lower bound of ≈ 0.045 m s^{-1}, set by the prescribed observational noise and the fitted kernel; masking below this floor removes the entire field. This floor exceeds the validated RMSE (0.028–0.033 m s^{-1}), indicating that the GPR posterior uncertainty is conservative relative to the reconstruction's actual out-of-sample error. Above the floor, all withheld verification points fall within the retained region, so RMSE and skill are essentially constant across masking thresholds of 0.05-0.15 m/s (RMSE ≈ 0.03 m s^{-1}, SS > 0.97). Thresholds above the saturation value (≈ 0.06 m s^{-1}) extend the displayed field into more sparsely observed regions without altering the validated statistics; the value of 0.075 m s^{-1} used in the main text was chosen to preserve the coherent eddy structure while remaining a modest ($\approx 1.7\times$) multiple of the uncertainty floor.

2.9 Appendix C: Choice of wavelet center frequency

The raw anticyclonic drifter spectra contain two near-inertial lines of comparable amplitude: the local inertial peak at f and the trapping peak at $f_{\text{eff}} \approx 0.85f$ (Figure 2.1b). Because we estimate a single instantaneous frequency from a single-scale Morse wavelet, the choice of center frequency sets the relative weight the filter gives either of these two lines. Figure 2.10 shows the normalized gain of the one-sided ($\gamma = 3$, $\beta = 25$) Morse wavelet on the clockwise (anticyclonic) side for several center frequencies. A wavelet centered on f (blue) passes the $f_{\text{eff}} = 0.85f$ line at only ≈ 0.44 of its f gain, so it systematically under-weights the trapping line and biases the recovered instantaneous frequency toward f. Shifting the center to $0.93f$ (yellow), the midpoint between the two known lines, roughly equalizes the gain at $0.85f$ and at f, so neither line is preferentially suppressed. We therefore center the wavelet at $0.93f$ throughout.

This choice does not manufacture a sub-inertial result: it only removes a known f-ward bias, and the resulting instantaneous frequencies agree with the wavelet-free multitaper spectral peaks of the same series (Section 2.4.3). We keep $\beta = 25$ rather than widening the wavelet because a broader filter admits the M2 tidal line at $1.06f$ without meaningfully improving recovery of the f_{eff} line; on the anticyclonic side the M2 contribution is more than an order of magnitude below the near-inertial peak (Figure 2.1b) and is not a concern here.

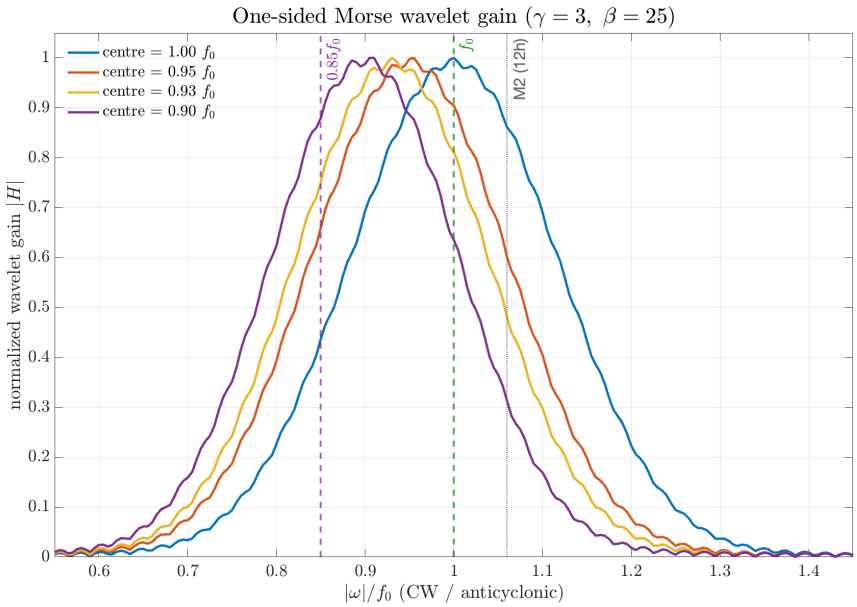


Figure 2.10. Normalized clockwise (anticyclonic) gain of the single-scale Morse wavelet ($\gamma = 3,\ \beta = 25$) as a function of $|\omega|/f$, for four center frequencies. Vertical dashed lines mark $f_{\text{eff}} = 0.85f$ (purple) and f (green); the dotted line marks the M2 tidal frequency ($1.06f$). Centering on f (blue) down-weights the f_{eff} line, whereas centering on $0.93f$ (yellow) balances the gain across the two known near-inertial lines. The wavelet center of $0.93f$ is used throughout this work.

Table 2.1. Mesoscale model-selection sweep under the unconstrained fit.

ψ_S	DOF	FullCoh	FullKappa	BestCoh	BestKappa	BgSm_eddy	BgSm_f_0
[2 2 1]	16	0.563	96.533	0.549	130.805	0.188	0.297
[2 2 2]	24	0.575	79.820	0.558	50.202	0.190	0.297
[2 2 3]	32	0.564	77.450	0.545	76.699	0.200	0.297
[2 2 4]	40	0.553	82.025	0.554	94.934	0.209	0.297
[2 2 5]	48	0.537	81.831	0.536	95.675	0.188	0.295
[3 3 1]	30	0.567	94.859	0.578	67.816	0.190	0.297
[3 3 2]	45	0.558	79.154	0.573	91.574	0.186	0.297
[3 3 3]	60	0.536	89.788	0.527	52.964	0.196	0.297
[3 3 4]	75	0.521	80.553	0.517	105.883	0.202	0.297
[3 3 5]	90	0.497	71.418	0.484	54.139	0.199	0.296
[3 3 6]	105	0.490	78.619	0.476	96.860	0.194	0.295
[3 3 7]	120	0.498	74.640	0.500	58.408	0.211	0.296
[3 3 8]	135	0.518	68.030	0.484	83.876	0.215	0.296
[3 3 9]	150	0.516	64.397	0.537	80.898	0.214	0.296
[3 3 10]	165	0.544	58.672	0.534	49.862	0.209	0.295
[3 3 11]	180	0.526	57.766	0.539	74.482	0.214	0.295
[3 3 12]	195	0.504	55.267	0.476	63.597	0.226	0.295
[3 3 13]	210	0.505	52.009	0.485	60.198	0.226	0.296
[3 3 14]	225	0.496	41.700	0.466	51.247	0.214	0.296
[3 3 15]	240	0.493	36.610	0.502	41.017	0.214	0.296
[3 3 20]	315	0.474	44.026	0.435	37.910	0.215	0.296
[4 4 1]	48	0.511	76.926	0.480	93.503	0.210	0.294
[4 4 2]	72	0.510	53.272	0.494	48.167	0.228	0.295
[4 4 3]	96	0.473	59.390	0.475	64.925	0.238	0.296
[4 4 4]	120	0.462	54.060	0.461	50.979	0.238	0.296
[4 4 5]	144	0.436	55.059	0.429	62.809	0.220	0.296
[4 4 6]	168	0.428	60.563	0.422	63.986	0.235	0.296
[4 4 7]	192	**0.424**	**53.934**	**0.418**	**49.066**	**0.258**	**0.296**
[4 4 8]	216	0.437	52.083	0.425	44.924	0.264	0.296
[4 4 9]	240	0.431	51.516	0.423	48.766	0.264	0.295
[4 4 10]	264	0.445	51.766	0.437	50.793	0.260	0.294
[4 4 11]	288	0.435	55.584	0.352	58.745	0.261	0.294
[4 4 12]	312	0.426	59.564	0.408	63.807	0.265	0.293
[4 4 13]	336	0.410	60.532	0.394	67.716	0.264	0.294
[4 4 14]	360	0.410	52.422	0.405	63.362	0.255	0.293
[4 4 15]	384	0.412	45.821	0.422	45.124	0.272	0.294

Table 2.2. Mesoscale model-selection sweep under the unconstrained fit - continued

ψ_S	DOF	FullCoh	FullKappa	BestCoh	BestKappa	BgSm_eddy	BgSm_f_0
[5 5 1]	70	0.495	87.062	0.483	93.789	0.219	0.294
[5 5 2]	105	0.497	57.865	0.543	30.759	0.238	0.295
[5 5 3]	140	0.460	65.738	0.452	62.335	0.245	0.296
[5 5 4]	175	0.438	61.894	0.491	32.868	0.237	0.296
[5 5 5]	210	0.421	62.910	0.469	37.778	0.238	0.296
[5 5 6]	245	0.418	61.702	0.465	39.000	0.255	0.297
[5 5 7]	280	0.424	54.302	0.470	38.292	0.279	0.298
[5 5 8]	315	0.426	52.532	0.476	39.024	0.277	0.298
[5 5 9]	350	0.418	50.913	0.475	42.134	0.273	0.297
[5 5 10]	385	0.413	50.703	0.381	58.559	0.278	0.296
[5 5 11]	420	0.415	49.799	0.463	33.681	0.277	0.296
[5 5 12]	455	0.404	48.554	0.452	40.278	0.282	0.296
[5 5 13]	490	0.399	51.747	0.455	34.840	0.267	0.296
[5 5 14]	525	0.392	49.497	0.320	55.463	0.285	0.297
[5 5 15]	560	0.385	42.726	0.438	29.239	0.257	0.296
[7 7 5]	378	0.403	64.898	0.372	80.683	0.245	0.295
[8 8 10]	880	0.393	63.419	0.435	38.253	0.302	0.299

Chapter 3

Stratified and stormy in the Bay of Bengal - internal waves and turbulence before and after cyclone Remal

3.1 Introduction

The Bay of Bengal is among the most stratified ocean basins on Earth (Sengupta et al., 2016; Chaudhuri et al., 2024). Strong freshwater influx from rivers and monsoon precipitation creates complex frontal structures and a shallow, buoyancy-driven mixed layer that is often capped by barrier layers: thin, highly stratified layers of low-salinity water that strongly inhibit vertical heat exchange. This strong stratification is a crucial factor for the many processes that connect the ocean to the overlying atmosphere by regulating sea surface temperatures, modulating heat fluxes, and ultimately influencing the timing, intensity and spatial structure of the Indian summer monsoon (Lucas et al., 2016; Luecke et al., 2021; Sheehan et al., 2023; McKie et al., 2024; Wijesekera et al., 2026). Nearly two billion people living across South and Southeast Asia depend on monsoon rains for agriculture, freshwater, and economic stability, making accurate prediction of monsoon variability an important and consequential challenge (Kar et al., 2021).

While coupled ocean-atmosphere models have improved substantially over the past two decades, significant gaps remain in our ability to forecast monsoon onset and intra-seasonal variability, gaps that can in part be traced back to poorly constrained ocean mixing processes in the Bay of Bengal (Cherian et al., 2020; Wijesekera et al., 2026). Central to those mixing processes are near-inertial internal waves (NIWs) and the turbulence they generate. As internal waves propagate, refract, and break, they drive diapycnal mixing that erodes stratification, entrains cooler subsurface water, and modulates mixed layer depth on time scales relevant to air-sea heat exchange (Chaudhuri et al., 2024). Because this subsurface turbulence regulates how much heat is entrained downward or returned to the surface, it exerts control on sea surface temperature and by extension on the air-sea heat and moisture fluxes that couple the ocean to the atmosphere. Thus subsurface turbulent heat flux can account for a substantial fraction of monsoonal upper-ocean cooling (Girishkumar et al., 2017; Shroyer et al., 2016).

Characterizing this turbulence is however complicated by strong stratification: the vertical

buoyancy structure that supports internal waves simultaneously suppresses turbulent dissipation. In this regime of strongly stratified turbulence, classical parameterizations may fail as they were developed for energetic, nearly isotropic flows in which a constant fraction of turbulent kinetic energy is assumed to be converted into irreversible mixing. When stratification is strong and turbulence is weak, buoyancy can suppress overturns before they fully develop, so that the mixing fraction depends on the turbulence–stratification balance rather than remaining constant (Caulfield, 2021; Gregg et al., 2018; Pham et al., 2023; Cherian et al., 2020). What sets this mixing fraction - the efficiency with which turbulent energy is converted into irreversible mixing - in strongly stratified, weakly turbulent regimes remains an open question.

Over the last decade, a series of multinational programs have progressively advanced our understanding of critical oceanic and atmospheric processes in Bay of Bengal. The Air-Sea Interactions in the Northern Indian Ocean (ASIRI) program established foundational observations of mixing and stratification in the northern Bay of Bengal (Wijesekera et al., 2016), while the Oceanic Control of Monsoon Intra-seasonal Oscillations in the Tropical Indian Ocean and the Bay of Bengal (MISO-BoB) campaign extended those insights with process-focused measurements targeting intra-seasonal variability and the monsoon mixed layer (Shroyer et al., 2021). Together, these efforts have revealed the critical role of salinity stratification in barrier layer formation, near-inertial wave generation, and the suppression of wind-driven mixing, but also highlighted the need for observations that capture multiscale processes and the full range of forcing conditions, including extreme events.

The Enhancing Knowledge of the Arabian Sea Marine environment through Science and Advanced Training (EKAMSAT) project builds on ASIRI and MISO-BoB and is specifically targeted at improving our understanding and parameterization of critical, unresolved small-scale processes that will improve monsoon prediction (Johnson et al., 2025). Figure 3.1 displays some of the relevant processes and highlights the interconnectedness of the atmosphere and ocean in the Bay of Bengal.

This work presents observations from the 2024 EKAMSAT field campaign aboard the

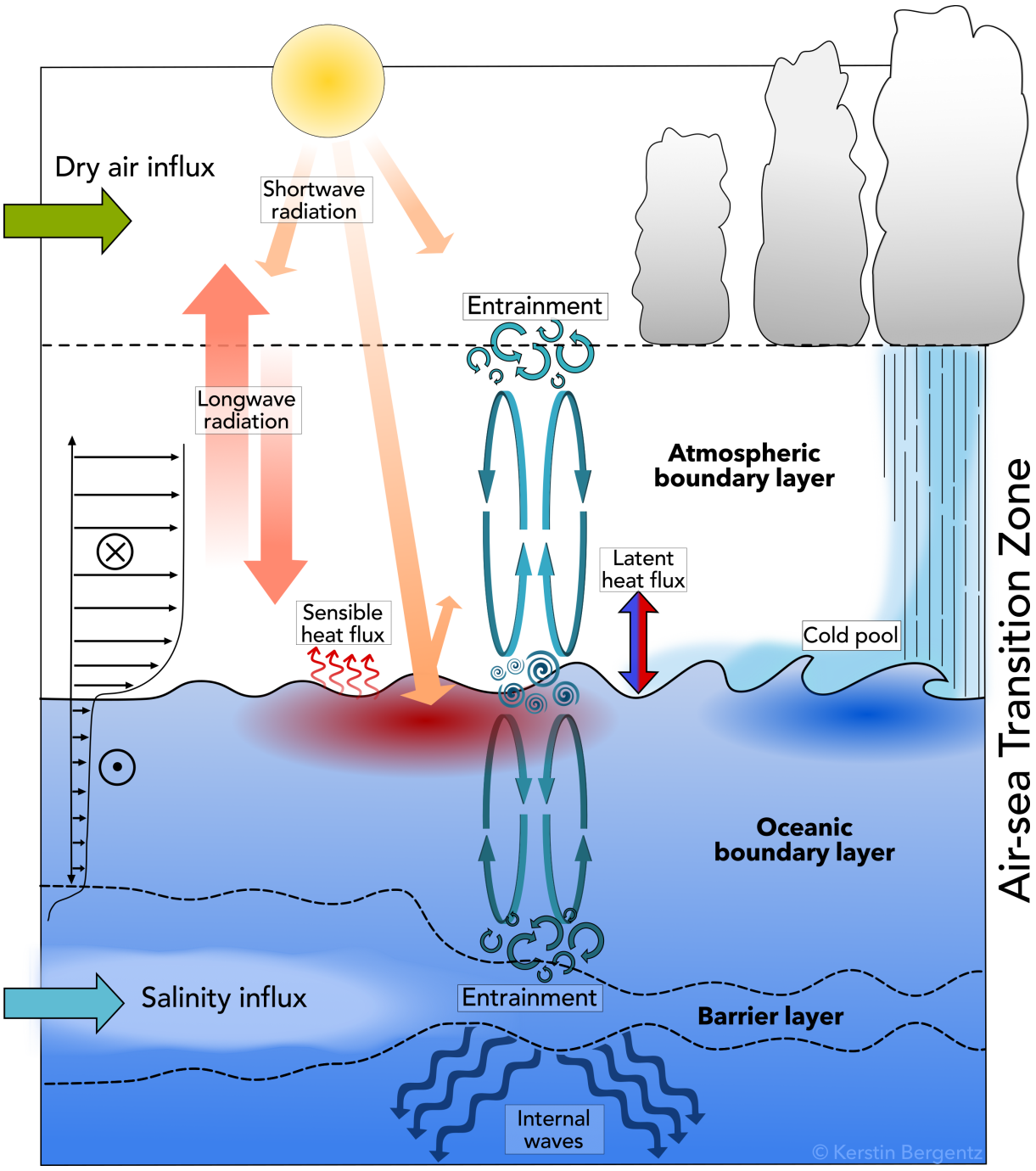


Figure 3.1. Overview graphic showing some of the focus areas of the Enhancing Knowledge of the Arabian Sea Marine environment through Science and Advanced Training (EKAMSAT) project and how the atmosphere and ocean are connected.

R/V *Thomas G. Thompson*, which took place in the Bay of Bengal during April 26thth-June 14th 2024 in two separate legs (26thth to May 14th and May 17th to June 14th 2024). Here we will only show data from the second leg of the cruise or from autonomous assets that were in the water for the duration for the field campaign. The timing of the cruise was chosen to sample the oceanic and atmospheric conditions just before and after the monsoon onset. A low pressure system that developed into severe cyclonic storm Remal formed midway through the campaign in the central Bay of Bengal and moved north to make landfall in Bangladesh on May 26th (NOAA National Centers for Environmental Information, 2024). The official onset of the Indian Summer Monsoon in the South Indian state of Kerala was declared shortly thereafter on May 30th (India Meteorological Department, 2024).

Before Remal and the monsoon onset there was very little wind forcing in the Bay of Bengal and our observations thus provide a before-and-after picture of the ocean's response to strong forcing. By analyzing microstructure, velocity, and density data collected on both sides of this transition, we document how the internal wave field evolved, how turbulent dissipation responded, and what the broader implications are for mixing parameterizations in the strongly stratified Bay of Bengal.

This paper is structured as follows, in section 3.2 we discuss the data and methods used. Section 3.3 presents the results showing the response of the upper ocean to the forcing associated with cyclone Remal. We discuss these results in section 3.4.

3.2 Methods

3.2.1 Instruments and data

Here we use data from three kinds of platforms deployed during the EKAMSAT 2024 field campaign that took place in the Bay of Bengal in May and June 2024.

The Wirewalker (WW) is a quasi-Lagrangian wave powered vertical profiler(Pinkel et al., 2011). Two Wirewalker systems were deployed, WW1 reaching 100 m, and WW2 consisting

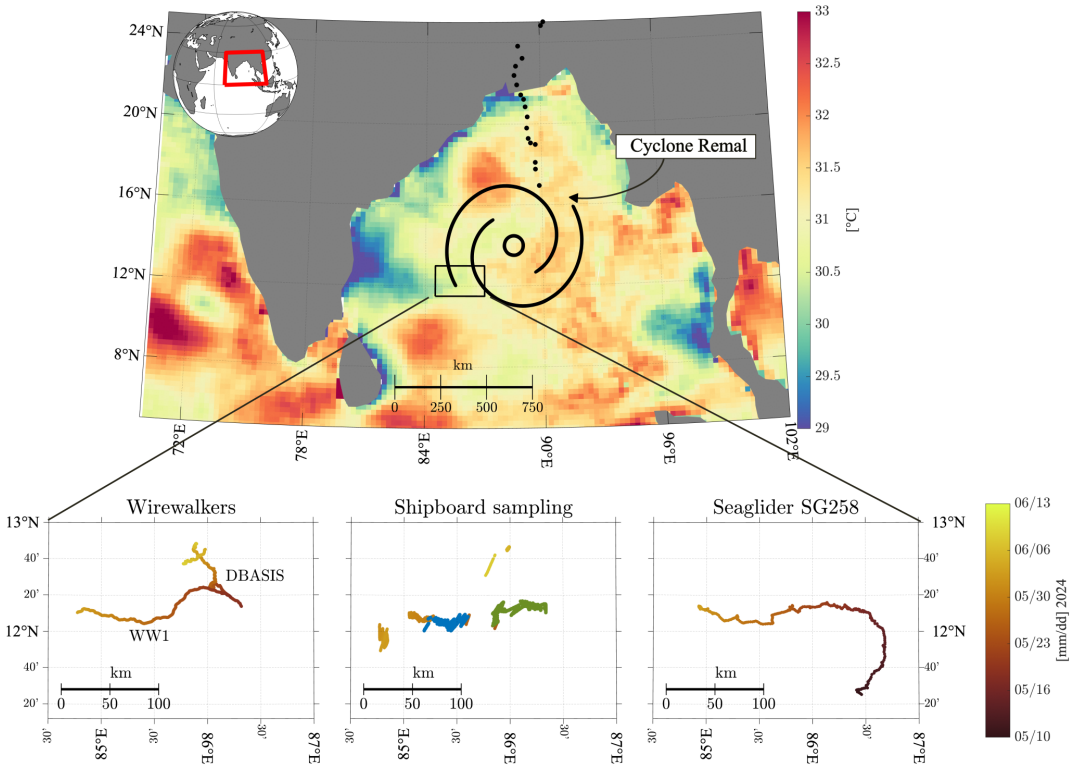


Figure 3.2. Map view of the Bay of Bengal with the approximate track of severe tropical cyclone Remal and a bounding box highlighting the sampling region for the 2024 EKAMSAT cruise and the drift tracks/sampling locations of each of the three main instruments used in this work. The green/blue segments of the shipboard sampling marks the before and after Remal time periods described in section 3.3.2. The units of time is day/month. The background color of the map is E.U. Copernicus Marine Services multi observation derived sea surface temperature on May 22nd 2024 (E.U. Copernicus Marine Service Information (CMEMS), 2024)

of two individual profilers, one covering the upper 100 m and one covering 100-500 m depth. This second system was a Drogued Buoy Air-Sea Interaction System (DBASIS) instrument, combining a Wirewalker with surface buoy equipped with meteorological sensors (Kachelein et al., 2025; Kerhalkar et al., 2026; Schlosser et al., 2026). We will refer to this instrument either as DBASIS or WW2. Both WW profilers were equipped with Nortek Signature 1000 Acoustic Current Doppler Profilers (ADCPs), RBR CTDs and biogeochemical sensors.

A Seaglider (SG) equipped with a Seabird CTD, Nortek signature 1000 ADCP, 4 beam radiometer, a wetlabs eco triplet, an Aanderra oxygen optode, and an in-house microstructure sensor and fast thermistor measured the top 500 m of the water column. Velocity data were binned to 5 m, and CTD data to 1 m. The Seaglider was piloted to stay near the freely drifting WW1 (following the average upper 100 m currents) during the time they were both deployed. We thus interpret the Seaglider track as "quasi-Lagrangian". The average time and distance between profiles was two hours and 1.3 km.

The third platform is a free-falling microstructure profiling system called the "epsilometer" or "epsi" developed by the Multiscale Ocean Dynamics Lab at Scripps Institution of Oceanography at UC San Diego (Le Boyer et al., 2021), including a custom made winch that was set up on the back deck of the R/V *Thomas G. Thompson*. The epsi has both airfoil shear probes and fast-response thermistors allowing for measurements of turbulent kinetic energy dissipation, ε, and the rate of thermal variance dissipation, χ. In addition, a SBE49 FastCAT from Sea-Bird Electronics mounted on the same vessel provides concurrent measurements of temperature and salinity. The vertical resolution of the final microstructure product after processing is 1 m and the horizontal resolution between profiles depends on profiling depth, vessel speed and currents, but is for most of the record presented here 360 m (around every 6 minutes).

Concurrent with the epsi sampling, we also use shipboard data from the 300 kHz RDI Mariner Workhorse ADCP aboard R/V *Thomas G. Thompson* which was processed using UHDAS (Hummon et al., 2023) at a 2 m vertical resolution and 2 minute intervals.

We also use several datasets from EU Copernicus Marine Service in the form of multi-

platform sea surface temperature and salinity observations (E.U. Copernicus Marine Service Information (CMEMS), 2024) (1/8°x 1/8°spatial and daily temporal resolution) to contextualize our data in Figure 3.2, and GLORYS12 model velocities (E.U. Copernicus Marine Service Information (CMEMS), 2023; Jean-Michel et al., 2021) (1/12°x 1/12°spatial and daily temporal resolution) to estimate the background vorticity along the drift tracks of the profiling instruments. Lastly, ERA5 reanalysis winds (Copernicus Climate Change Service, Climate Data Store, 2023; Hersbach et al., 2020) (1/4°x 1/4°spatial and hourly temporal resolution) were used to estimate wind work as $\vec{\tau} \cdot \vec{u}$ using $\vec{\tau} = \rho_a C_d |\vec{u}_a - \vec{u}_s|(\vec{u}_a - \vec{u}_s)$ where ρ_a is the surface air density and C_d is the drag coefficient here assumed to be nonlinear following Large and Pond (1981) and corrected for low winds according to Trenberth et al. (1989). $\vec{u}_a$ is the 10 m wind and $\vec{u}_s$ is the surface currents of the ocean from the GLORYS12 model. The ERA5 winds were validated against the available in-situ observations from the ship and DBASIS buoy and found to agree within 5-10%. Since not all platforms have wind sensors we use ERA5 winds interpolated onto all platform locations for consistency.

3.2.2 WKB scaling and spectral decomposition

To account for the effect of varying stratification with depth Wentzel-Kramers-Brillouin (WKB) stretching and scaling was applied to the WW and Seaglider ADCP velocities and vertical shear ($\partial u/\partial z$, $\partial v/\partial z$) Leaman and Sanford (1975); Gregg (1989) below the mixed layer. We use the same canonical background stratification value N_0 value of 0.0098 s^{-1}, based on WW2, for the buoyancy frequency between all instruments with an average N^2 profile based on the SG and WW2 where $N^2 = -(g/\rho_0)(\partial\rho/\partial z)$, g being the gravitational acceleration of 9.8 m/s^2 and $\rho_0 = 1025 \mathrm{kg/m^3}$. The WKB-stretched depth coordinate is

$$dz^*_{wkb} = \int N_0^{-1} N(z,t) dz \tag{3.1}$$

and the WKB scaled velocity is

$$U_{WKB} = U\left(\frac{N_0}{N(z,t)}\right)^{1/2} \tag{3.2}$$

whereas the shear scales as

$$U_{z,WKB} = \partial U_{WKB}/\partial z^*_{wkb} \propto \left(\frac{N(z,t)}{N_0}\right)^{3/2} U_z \tag{3.3}$$

as differentiating the WKB-scaled velocity with respect to z^*_{wkb} brings in an extra factor of N/N_0. $N(z,t)$ is the buoyancy frequency $N = \sqrt{-\frac{g}{\rho}\frac{d\rho}{dz}}$, here slightly smoothed in depth (2 m moving mean) and time (24 h moving mean). The $N^{3/2}$ shear scaling in (3.3) applies to an individual propagating internal wave; for a finite-bandwidth internal wave spectrum the observed shear amplitude scales more nearly with N than with $N^{3/2}$. As in (Leaman and Sanford, 1975; Gregg, 1989), this WKB treatment is formally valid when the vertical scales of the waves are much smaller than the vertical scales over which the background stratification varies, so that $N(z,t)$ can be viewed as locally slowly varying. Here we use the scaling as a practical normalization for comparing shear and velocity across instruments in a strongly stratified environment, with the caveat that some observed waves approach the limit of this assumption.

The velocity fields of all drifting platforms were first binned to a 5 m vertical grid (matching the Seaglider native vertical resolution) and decomposed in the vertical wavenumber domain by applying a fast Fourier transform (FFT) along the depth coordinate at each time step independently, with a Hanning window applied prior to the transform to reduce spectral leakage. The spectrum was partitioned by the sign of the vertical wavenumber k_z using a smooth hyperbolic tangent filter. The inverse FFT recovered the upward phase ($k_z > 0$) and downward phase ($k_z < 0$) velocity components separately, corresponding to downward and upward energy propagation respectively. Both components were then mapped onto isopycnal coordinates using a time-mean density profile, and WKB-scaled following equations 3.1-3.3. Vertical shear was

computed from the decomposed, scaled velocity components by finite differencing over the 5 m grid.

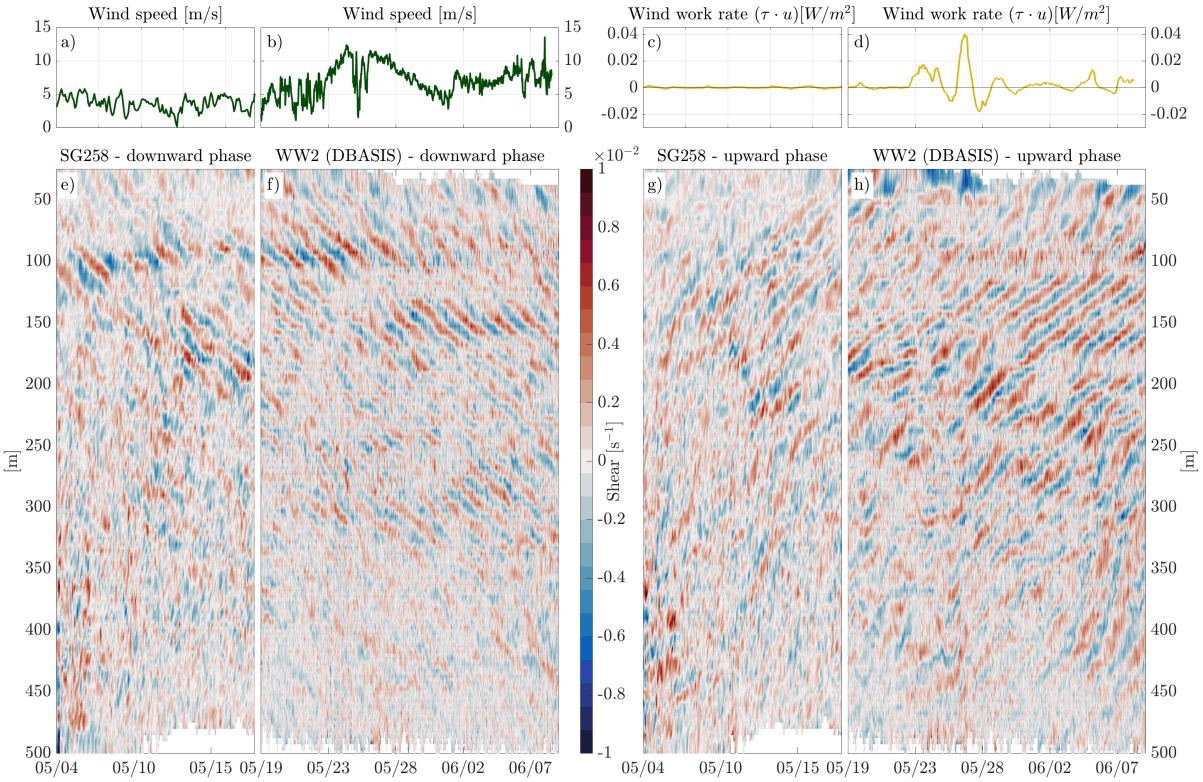


Figure 3.3. Wind and internal wave shear at the Seaglider (SG) and Wirewalker2 (WW2/DBASIS) locations. Panel a-b) show ERA5 wind speed at the SG and WW2 locations respectively, c-d) the same but wind work. Panel e-f) show the downward phase of the rotary decomposed, Wentzel, Kramers, and Brillouin (WKB) scaled and stretched vertical shear from the SG and WW2 respectively, and panel g-h) the same but upward going phase. x-axis time units are month/day 2024.

3.2.3 Wave characteristics and ray tracing

Near-inertial internal wave properties for select wave packets were estimated following (Alford and Gregg, 2001). Velocity shear profiles were WKB-scaled, rotary decomposed and band pass filtered to 0.7-1.5 f_0 using a second-order Butterworth filter and where f_0 is the Coriolis parameter at latitude 12.5° N, the mean latitude of the Seaglider drift track. The horizontal propagation direction θ of the wave was estimated by two methods: (1) the phase of

the cross-spectrum between isopycnal strain ξ_z and the horizontal shear components, and (2) the orientation of the major axis of the velocity shear ellipse. We take the mean of the two as the reported bearing θ. The intrinsic frequency ratio $r_I \equiv \omega_I / f_{\text{eff}}$ between the wave intrinsic frequency ω_I and the effective Coriolis frequency $f_{\text{eff}} = f_0 + \zeta/2$ was estimated from the kinetic to potential energy ratio R via $r_1 = \sqrt{(R+1)/(R-1)}$ (Fofonoff, 1969) and from the shear ellipticity $r_2 = a/b$ where a/b is the ratio of the major and minor axes. Per-instrument estimates of r_1 and r_2 were averaged to estimate r_I. In principle the effective Coriolis frequency f_{eff} can be determined self-consistently following Alford and Gregg (2001) eq.19, using the observed wave frequency ω_o, instrument drift velocity $\mathbf{U}$, propagation direction θ, and dominant vertical wavenumber $m_0 = 2\pi/\lambda_z$ where in our case $\lambda_z = 42 - 45$ m based on wavenumber spectra from the Seaglider and DBASIS instruments (appendix Figure 3.9) from which the background relative vorticity follows as $\zeta = 2(f_{\text{eff}} - f_0)$ (Kunze, 1985). Here however, we set $f_{\text{eff}} = f_0$, as the modeled background vorticity along the glider track is small ($|\zeta/f| < 0.1$ for most of the record, rendering the vorticity and Doppler corrections to f_{eff} second order. The intrinsic frequency $\omega_I = r_I f_{\text{eff}}$ and the internal wave dispersion relation then yield the horizontal wavenumber K_h and vertical group velocity c_{gz}. Backward ray tracing was performed from the observed wave depth using the WKB ray equations, with f_{eff} updated at each latitude step and $m(z)$ scaled as $m_0 N(z)/N_{\text{site}}$. Downward propagating rays were integrated backward until reaching the base of the mixed layer, providing estimates of wave generation location and time.

3.2.4 Microstructure data analysis and stratification relative coordinates

To investigate the bulk properties and vertical structure of turbulence before versus after Remal we use various descriptive ratios and non-dimensional numbers. First, the temperature and salinity data obtained with the epsi system was used to estimate the mixed layer (ML) depth for each epsi profile using a density threshold criterion of $\Delta\rho = 0.20$ kg/m^3 referenced to 10m depth, and all observations shallower than the ML base and deeper than 85 m were masked prior to analysis (this lower limit is due to quality issues with the shipboard ADCP

data below this depth). Data quality filtering excluded observations with $N^2 < 10^{-7}$ s^{-2} and $\varepsilon > 10^{-5}$ W/kg identified as spurious outliers in the otherwise strongly stratified and weakly turbulent regime. Velocity shear was computed from the shipboard 300 kHz ADCP velocities on their native 2 m vertical grid resolution and then interpolated in time onto the microstructure profiler grid. The microstructure data were subsampled to match this vertical resolution and the gradient Richardson number $Ri = N^2/S^2$, where $S^2 = (\partial u/\partial z)^2 + (\partial v/\partial z)^2$, was computed at each depth-time point below the MLD. Sample points were classified as dynamically unstable ($Ri < 0.25$), marginally stable ($0.25 \leq Ri \leq 1$), and stable ($Ri > 1$). Because a finite-difference shear estimate acts as a low-pass filter, attenuating shear variance at vertical scales smaller than roughly twice the grid spacing, S^2 computed on the 2 m ADCP grid underestimates the true shear variance; the gradient Richardson number is therefore biased high and our reported frequencies of low-Ri conditions are conservative lower bounds. As both periods are processed on the identical grid with the same differencing, this resolution effect is common to both and does not affect the before-versus-after comparison.

Several non-dimensional parameters characterize the influence of stratification on turbulence, including the gradient Richardson number, turbulent Froude number $Fr_t \sim (\varepsilon/N^3L^2)^{1/2}$, and buoyancy Reynolds number $Re_b = \varepsilon/\nu N^2$ (Mater and Venayagamoorthy, 2014; Ivey et al., 2008). While Fr_t has been argued to be a more fundamental regime parameter because it more directly captures whether turbulent eddies are dynamically influenced by stratification (Mater and Venayagamoorthy, 2014), it requires an independent turbulent velocity or length scale that is not directly accessible from microstructure profiler data alone. We therefore use Re_b, which is computable directly from co-located ε and N^2 measurements.

The buoyancy Reynolds number Re_b, where $\nu \approx 10^{-6}$ m^2/s is the kinematic viscosity, provides a non-dimensional measure of the intensity of turbulence relative to the stabilizing effect of stratification (Smyth and Moum, 2000; Ivey and Imberger, 1991). In the weakly turbulent regime ($Re_b \lesssim 1$) molecular diffusion dominates and turbulence is effectively suppressed; for $1 \lesssim Re_b \lesssim 100$ turbulence is present but strongly influenced by stratification, and for $Re_b \gtrsim 100$

turbulence is sufficiently energetic to be considered in the classical, nearly isotropic limit (Smyth and Moum, 2000). We additionally estimate the Ozmidov scale $L_O = (\varepsilon/N^3)^{1/2}$, the largest vertical scale not suppressed by buoyancy, as a scale-based complement to Re_b; these are related by $L_O/\eta_K \sim Re_b^{3/4}$ where $\eta_K = (\nu^3/\varepsilon)^{1/4}$ is the Kolmogorov scale. These estimates were done by averaging over three hand picked boxes around patches of increased dissipation before versus after cyclone Remal.

Here we use $Re_b \geq 20$ as a criterion for "active turbulence" (Smyth and Moum, 2000; Ivey and Imberger, 1991). The thickness of an active turbulence layer was estimated as the average vertical extent over which 50% of total turbulent dissipation is located, and the number of active turbulence layers per profile was defined as the count of contiguous depth segments satisfying $Re_b \geq 20$, both serving as metrics of vertical coherence. As the ML deepened by approximately 18 m post-Remal (29 m $\rightarrow$ 44 m) we define a stratification-relative coordinate to compare the vertical structure of turbulence in the thermocline between periods as discussed in section 3.4.2. Specifically, $z^* = (z - z_{\mathrm{MLD}})/(z_{\mathrm{pycno}} - z_{\mathrm{MLD}})$, where z_{pycno} is the depth of maximum N^2, so that $z^* = 0$ corresponds to the base of the mixed layer and $z^* = 1$ to the pycnocline. It is over this range that all our bulk properties are estimated.

With co-located measurements of ε and χ we estimate the mixing efficiency as

$$\Gamma = \frac{\chi N^2}{2\varepsilon \left(\partial \overline{T}/\partial z\right)^2}, \tag{3.4}$$

which follows from setting the Osborn (1980) diffusivity estimate $K_\rho = \Gamma\varepsilon/N^2$ equal to the Osborn and Cox (1972) temperature-based estimate $K_T = \chi/\left[2\left(\partial \overline{T}/\partial z\right)^2\right]$ and solving for Γ (Oakey, 1982). Here $\partial \overline{T}/\partial z$ is the per before/after time period (about 6 days each) average temperature profile and the buoyancy frequency N^2 has been smoothed with a 5 m moving median filter. Because both Osborn (1980) and Osborn and Cox (1972) use Reynolds-averaged turbulent kinetic energy and temperature variance budgets under assumptions of stationarity and spatial homogeneity, it follows that the appropriate bulk estimator of Γ is a ratio of means:

$\hat{\Gamma} = \langle\chi\rangle\langle N^2\rangle / \left(2\langle\varepsilon\rangle \left(\partial\overline{T}/\partial z\right)^2\right)$, where angle brackets denote averages in time and/or space. While Winters and D'Asaro (1996) and Alford et al. (2025) compute Γ by averaging on isothermal surfaces tracked through time, requiring densely repeated profiles at a fixed location, here we estimate vertical profiles of Γ by averaging in our normalized thermocline depth coordinate z^*, since with a moving-ship geometry it is difficult to continuously track individual isothermal surfaces and the Bay of Bengal is strongly salinity stratified rendering temperature more of a passive tracer. We note that although Γ is only clearly defined as an average over a "mixing event", such an "event" is in itself not always a straightforward thing to define, especially as the properties of turbulence varies in time from onset to the final decay phase (Mashayek et al., 2021). Here we are specifically interested in the patterns and phenomenology of how Γ varies in depth and time and thus we also compute pointwise estimates of Γ as a diagnostic of spatial and temporal variability - in particular the dependence of Γ on Re_b - but we stress that these values should not be interpreted as bulk mixing efficiencies.

There are many things to take into consideration when estimating Γ. For example, in the energetic turbulence limit ($Re_b \gtrsim 100$), Shih et al. (2005) proposed a revised parameterization $\Gamma \sim 2\,Re_b^{-1/2}$ based on direct numerical simulations, departing from the canonical constant value of $\Gamma = 0.2$ (Osborn, 1980). Further, in environments susceptible to double-diffusive instabilities, such as very salinity stratified regions like polar regions or the Bay of Bengal (George et al., 2021), differential diffusion of heat and salt can drive buoyancy fluxes independently of mechanical turbulence, potentially biasing estimates of Γ (Monismith et al., 2018). Following Monismith et al. (2018), we therefore restrict our analysis of Γ as a function of Re_b to observations where the density ratio $R_\rho = \alpha|\partial T/\partial z|/\beta|\partial S/\partial z|$ satisfies $0.5 < R_\rho < 2$, a range in which neither salt fingering nor diffusive convection is expected to be active. Finally, we note a resolution caveat on the interpretation of Γ. The temperature-gradient spectra used to estimate χ are integrated over varying length scales of approximately 0.5-20 cpm, and in a weakly turbulent regime such as this the Ozmidov scale falls to $\mathcal{O}(0.1\ \mathrm{m})$ which is at the very edge of the resolved band. Under these

conditions we don't expect the turbulence to be fully isotropic, thus the isotrophy assumption underlying equation (3.4) is only approximately satisfied and individual Γ values should not be read as exact mixing efficiencies. However, because both time periods before and after Remal are identically sampled and processed, any bias is common to both periods and does not affect the before versus after comparison that is central to this study.

To compare distributions of oceanographic quantities between periods we use two-sample Kolmogorov-Smirnov (KS) tests, which assess whether two samples are drawn from the same underlying distribution without assuming a particular distributional form. Since statistical significance alone can be misleading at large sample sizes, we additionally report Cliff's δ as a non-parametric effect size measure. For two groups X and Y of sizes m and n, Cliff's δ is defined as:

$$\delta = \frac{1}{mn} \sum_{i=1}^{m} \sum_{j=1}^{n} sgn(x_i - y_j), \tag{3.5}$$

where $sgn(\cdot)$ is the sign function, so that $\delta \in [-1, 1]$ represents the probability that a randomly drawn observation from X exceeds one from Y, minus the reverse probability (Cliff, 1993). We use effect size thresholds following Romano et al. (2006) where $|\delta| < 0.147$ is considered negligible, 0.147-0.33 small, 0.33-0.474 medium, and $|\delta| > 0.474$ large.

3.3 Results

This section describes our observations of the Bay of Bengal internal wave environment in section 3.3.1 and the data collected by the epsilometer in section 3.3.2.

3.3.1 Internal waves and ray tracing

The Bay of Bengal displayed a rich internal wave environment well before any wind forcing associated with cyclone Remal. Figure 3.3 shows the rotary decomposed, WKB scaled and stretched vertical shear from the Seaglider and WW2. The unfiltered shear is shown in

appendix Figure 3.9. Wind work was negligible before cyclone Remal followed by a strong impulse, (Figure 3.3 subpanels c-d). The subsurface wave field contained substantial energy with signs of both upward and downward propagating wave packets in the form of coherent phase lines well before any storm forcing (Figure 3.3e-h). We also note the small vertical scales of many of the wave packets; in the upper 100-150 m, several waves have vertical wavelengths on the order of 20 m (appendix Figure 3.10). Estimating the vertical phase speeds as the slope of phase lines over time suggests $c_{pz} \approx$ 5-10 m/day, which, combined with the observed vertical wavelengths and a local buoyancy frequency of $N \approx 0.0045 s^{-1}$ for the waves, yields horizontal wavelengths of $\lambda_h = \lambda_z \sqrt{(N^2 - \omega^2)/(\omega^2 - f^2)} \approx$ 5-10 km via the internal wave dispersion relation.

Using the Seaglider velocity data, which provide the longest continuous sampling record, we perform ray tracing as outlined in Section 3.2.3 on a subset of the wave packets visible in Figure 3.3 to identify if any of these waves might have been generated by Remal. We begin by inertially bandpass filtering (0.8-1.2f_0) the Seaglider shear and then identify wave packets as strong, coherent phase-line patches in Figure 3.4b,c. We select a few that either coincide with enhanced shear variance (Figure 3.4d) or exhibit particularly clear phase-line patterns. Some packets display unambiguous upward or downward propagating phase; others show strong phase lines in both directions and are thus traced both upward and downward accordingly. The ray paths in Figure 3.4h indicate that only one of the observed packets (ray 6) exits the mixed layer at a time consistent with its origin being wind forcing from cyclone Remal; we return to this attribution in Section 3.4.1. The two independent estimates of the horizontal propagation directions θ provide a measure of confidence in the traced bearings seen in 3.4f. For a well defined, single-wave packet the cross-spectrum and shear ellipse method results should coincide. If they diverge that is an indication of contamination by neighboring waves, that the wave packet is weak, or subject to the inherent 180° ambiguity of a direction inferred from a single platform. The two methods agree most closely for ray 6 (within 10°), the ray whose mixed layer exit aligns with Remal and lends independent support to that attribution. In contrast, θ estimates for

the other waves differ by 50-120°which we interpret as directional uncertainty from a single glider track rather than competing solutions. The horizontal origins of the traced waves shown in Figure 3.4f should therefore be read as indicative of a propagation corridor, here predominantly west/northwestward moving, rather than precise source locations. However, the vertical timing of each ray is set by the observed group velocity and more tightly constrained.

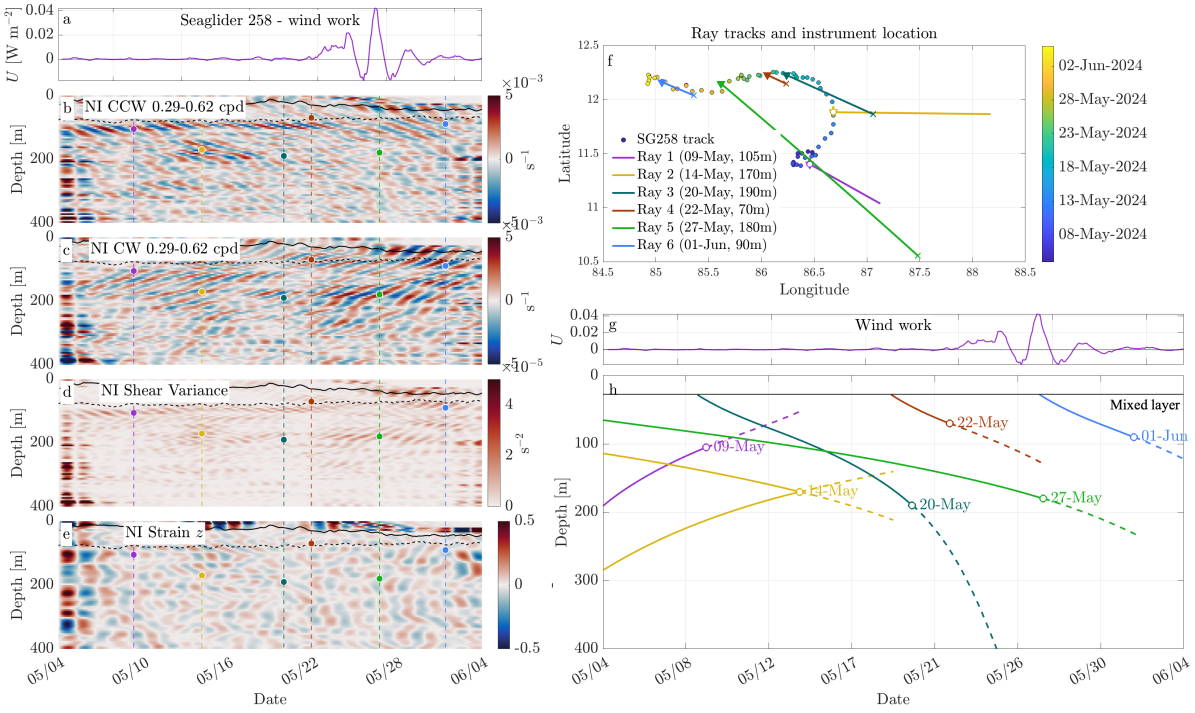


Figure 3.4. Seaglider a) windwork (from ERA5), near-inertially filtered shear decomposed into b) downward propagating phase, c) upward propagating phase, d) total shear variance, e) near-inertially filtered stain. Solid black line indicate the mixed layer and dashed black line the pycnocline (maximum N^2). Panel f) Seaglider track and paths of the traced rays where stars mark the below the mixed layer entry of downward rays, and ray paths without stars mark the horizontal direction of upward going rays with unknown vertical origin. Panel g) same as panel a) used to contextualize panel h) showing the depth/time paths of rays marked in panel b-e) and associated directions of the energy contained in the identified wave packets.

3.3.2 Turbulence environment and mixing efficiency

Using data from the epsi and the shipboard ADCP we estimate characteristics of the subsurface microstructure environment in the thermocline before and after cyclone Remal. The

water column underwent clear structural changes in response to Remal. Temperature and salinity gradients in the surface mixed layer were erased, the mixed layer deepened, and isopycnals below the mixed layer compressed as stratification increased (Figure 3.5). Visually, the turbulent dissipation ε (Figure 3.5g-h) and shear in the thermocline (Figure 3.5k-l) appear more layered. A subsurface salinity minimum appeared near 60!m depth around May 23$^{\text{rd}}$-24$^{\text{th}}$ (Figure 3.5a) and lasted for about 2 days. The pointwise estimates of Γ have a coherent vertical structure with regions of low Γ broadly aligning with regions of elevated ε (Figure 3.5m,n).

Figure 3.6 summarizes how the bulk shear-stratification environment and the vertical structure of dissipation changed between the pre- and post Remal periods using the same profiles shown in Figure 3.5. First, the median value and distribution shape of the dissipation ε and Richardson number in the thermocline only changed marginally after the storm (Figure 3.6a and d). However, the vertical structure of dissipation ε did change: both the turbulent layer thickness and number of layers of active dissipation decreased after the storm (Figure 3.6b,c). Bulk shear and stratification values increased by 90% and 45% respectively and their vertical structure also changed (Figure 3.6e and f) after cyclone Remal. Two-sample Kolmogorov-Smirnov tests confirm that all distributions differ significantly between periods ($p < 0.01$); Cliff's δ effect sizes indicate that the stratification increase is large and spatially coherent ($\delta = 0.51$) whereas the shear increase, while significant, is more variable across observations ($\delta = 0.27$), consistent with the intermittent nature of shear-driven turbulence.

Although the absolute depth of "peak dissipation", defined as the 20% strongest ε values, shifted 5 m deeper after Remal in absolute depth, in the normalized depth coordinate z^* the peak dissipation depth shifted closer to the base of the mixed layer and that portion of the water column now has a higher occurrence of $Ri < 1$ (Figure 3.6g). Lastly, for the active turbulence (defined as $Re_b \geq 20$) the median gradient Richardson number decreased from 1.28 to 0.84 (Figure 3.6h). The associated bulk stratification N^2 increased by 45% ($\delta = +0.44$, medium) and the associated shear variance S^2 increasing by 112% ($\delta = +0.36$, medium). This indicates that post-storm active turbulence occurs preferentially in regions of elevated shear rather than

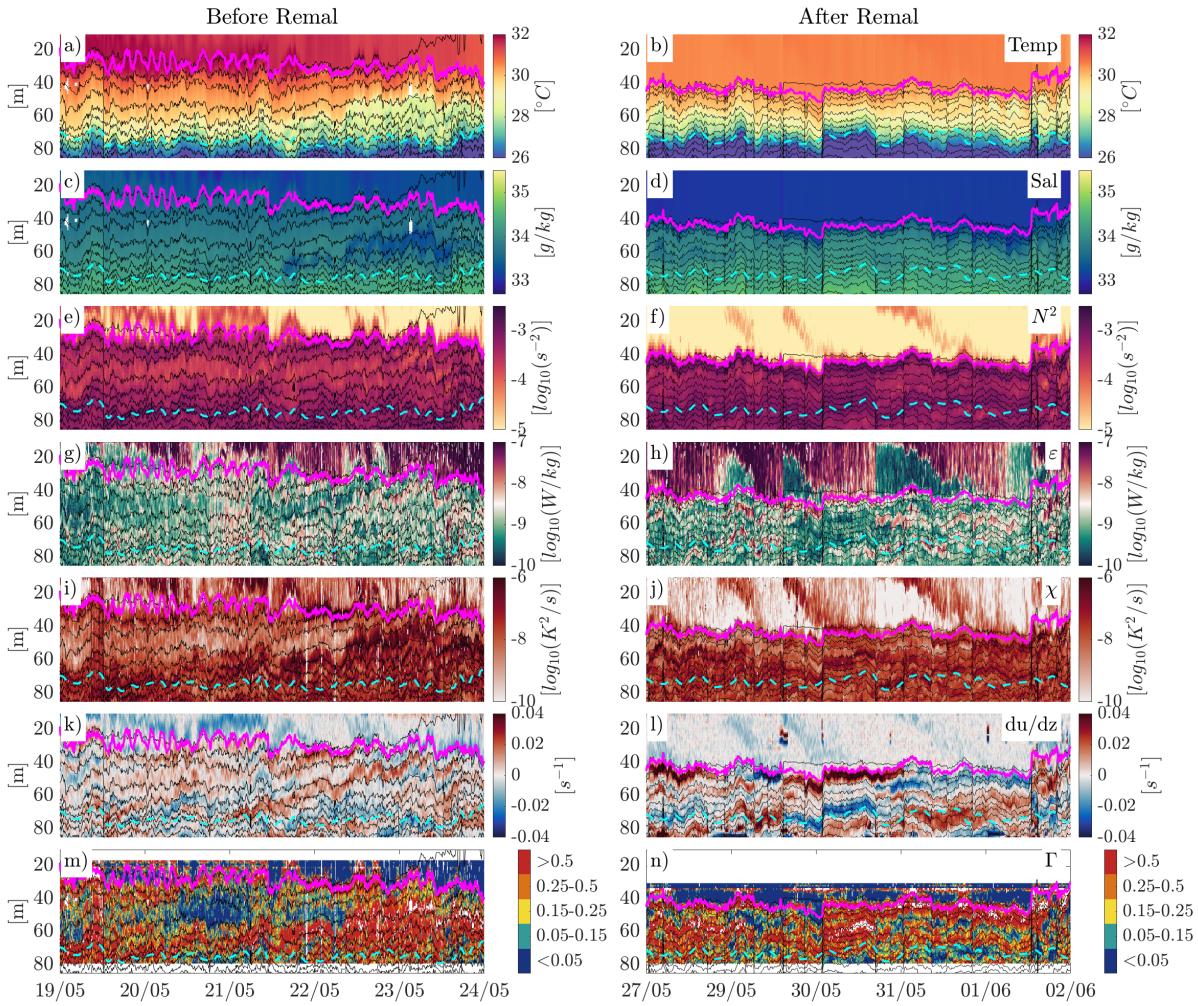


Figure 3.5. Section plots from the epsi before (left) and after (right) cyclone Remal showing a-b) conservative temperature, c-d) absolute salinity, e-f) buoyancy frequency N^2, g-h) ε, i-j) χ, k-l) zonal shear from the shipboard Acoustic Doppler Current Profiler (ADCP), m-n) estimates of mixing efficiency Γ (equation 3.4). Pink line shows the mixed layer depth and dashed cyan line the pycnocline (maximum N^2).

being spatially random. We also note that the mean pycnocline depth shoaled slightly after the storm, from 75 m to 69 m depth, likely a signature of entrainment during mixed-layer deepening, though isopycnal heave may contribute.

Figure 3.7 summarizes changes to the mixing efficiency Γ and its dependence on turbulence intensity before and after cyclone Remal. The vertical structure of ε, χ and Γ in z^* coordinates (Figure3.7a,b) shows that both periods have broadly similar vertical profiles, but

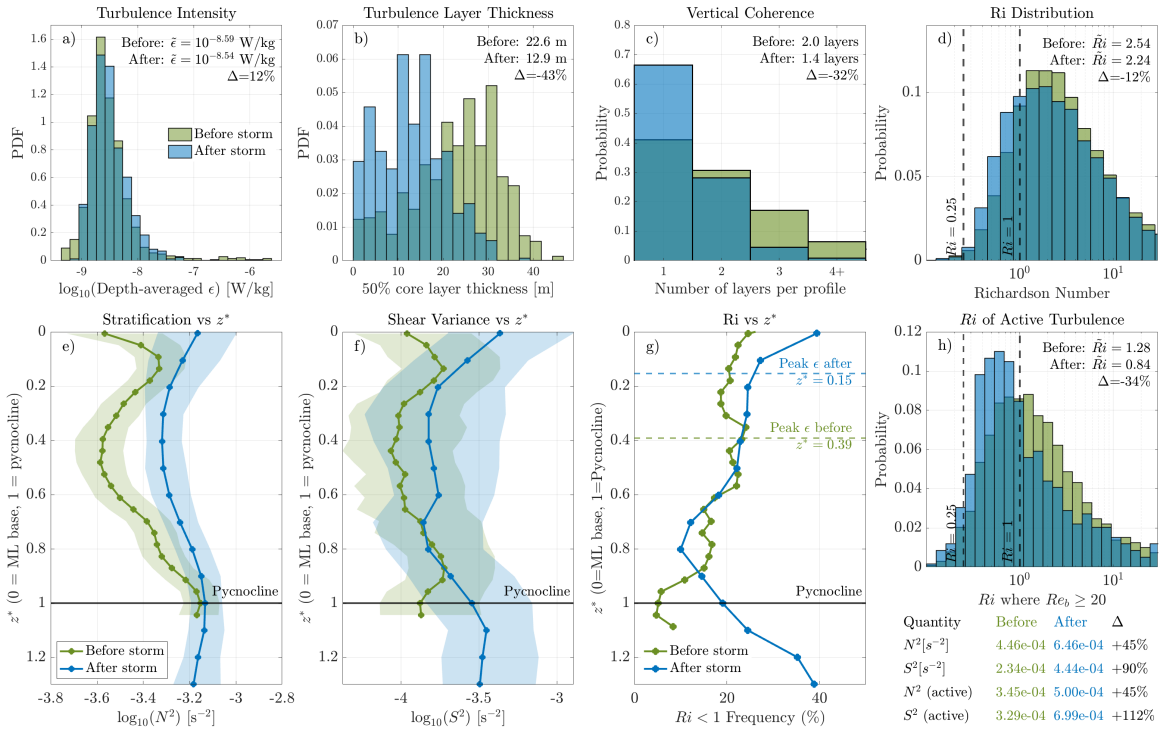


Figure 3.6. Bulk properties of the water column in the thermocline before and after Remal using the data shown in Figure 3.5. Sub panel a) depth average ε and median values, b) turbulent layer thickness, c) number of turbulent layers per profile, d) gradient Richardson number ($Ri = N^2/S^2$) and median values, e) stratification and f) shear variance and g) fraction of water column with $Ri < 1$ and location of the strongest 20% of ε values in the normalized depth coordinate, h) gradient Richardson number of active turbulence ($Re_b \geq 20$). All differences are significant by two-sample Kolmogorov-Smirnov test $p < 0.01$, and the shading in panels e-f are inter-quartile ranges.

the after-storm profile sits systematically at lower values of Γ across most of the water column. Separating by turbulence activity level (Figure 3.7c) and estimating bulk Γ for the thermocline ($z^* = 0$ to $z^* = 1$) as the ratio of means of all points that fall into each category active/inactive and before/after Remal, the inactive turbulence ($Re_b < 20$) dominates the record in both periods ($\sim$89-92% of valid observations) and shows a downward shift in Γ ($\delta = +0.43$, medium effect size). Active turbulence events also show a small but significant -47% decrease in Γ after the storm ($\delta = -0.49$, large). Since Γ reflects how much of the turbulent energy goes into mixing buoyancy rather than being lost to viscous heating, this decrease indicates that a larger share of the post-storm turbulent kinetic energy was dissipated as heat rather than spent mixing: the

storm-forced turbulence is more energetically intense but not proportionally more efficient at mixing buoyancy.

The distribution of the buoyancy Reynolds number Re_b (Figure 3.7d) suggests that the majority of observations fall in a weakly turbulent regime, with geometric medians of 3 and 2 before and after the storm respectively. This small shift toward lower Re_b after the storm, despite the increase in ε seen in Figure 3.5, is consistent with the observed increase in N^2 outpacing the dissipation increase. The KS test is significant ($p < 10^{-4}$) but the effect size is small ($\delta = -0.22$), again reflecting distribution overlap. For the Γ-Re_b relationship specifically (Figure 3.7e), we show pointwise estimated restricted to a double-diffusion-safe subset (density ratio $0.5 < R_\rho < 2$, Monismith et al. (2018)) so that the low-Re_b, high-Γ points cannot be an artifact of salt-finger enhancement of χ; all other panels and statistics use the full dataset. This criterion retains 33% of valid (Γ, Re_b) pairs before the storm and 24% after, the decrease reflecting a post-storm shift toward more double-diffusive favorable density ratios as the salinity structure sharpened. Within this subset, both periods follow the expected pattern of elevated Γ at low Re_b. Very few of our data points fall in the $Re_b > 100$ range where Shih et al. (2005) proposed a scaling $\Gamma \sim 2\,Re_b^{-1/2}$, but we note the approximately similar slope here seen for $Re_b < 100$. There is also no clear trend toward the canonical $\Gamma = 0.2$ at intermediate Re_b, but we again note that bulk Γ should be correctly estimated as ratio of means and that for the data points in the active turbulence before Remal category, the bulk Γ value is exactly 0.2. The binned means from before and after the storm largely overlap within uncertainty (Cliff's $\delta = +0.11$, negligible), indicating that the Γ-Re_b relationship was not fundamentally altered by the storm; the same conclusion holds for the full, unrestricted dataset where double-diffusive points have not been excluded (Cliff's $\delta = +0.04$, negligible).

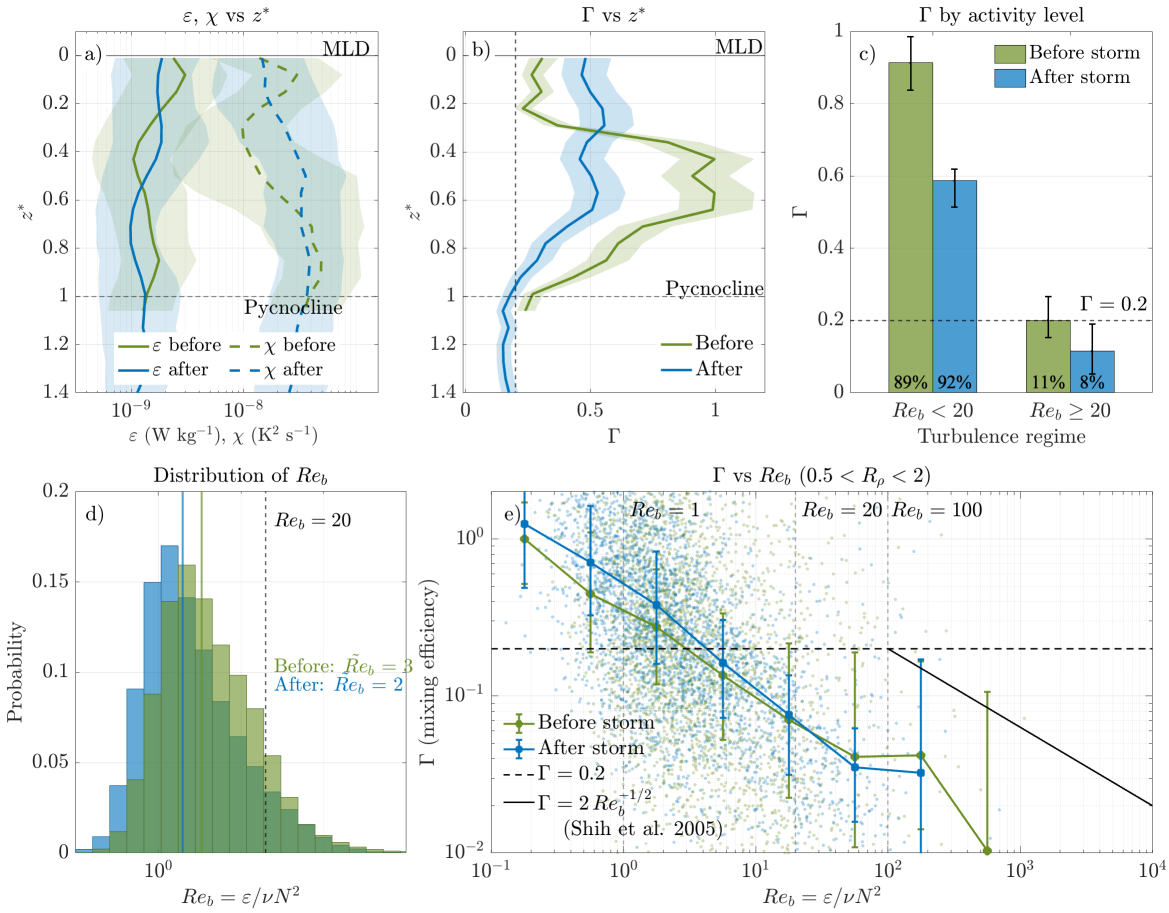


Figure 3.7. Bulk characteristics of the mixing efficiency Γ (3.4)before and after cyclone Remal. a) Mean vertical profiles of χ and ε with shaded inter-quartile ranges and b) Γ with confidence intervals computed as in Gregg et al. (1993), all relative the normalized depth coordinate z^* c) Mean Γ per dissipation activity level and the percentages of all data points these subsets represent d) distribution of buoyancy Reynolds number Re_b, e) Γ vs Re_b for the subset of data where $0.5 < R_\rho < 2$, error bars show inter-quartile ranges and with a horizontal line for $\Gamma = 0.2$ and a line for the $\Gamma(Re_b)$ dependence for $Re_b > 100$ described in Shih et al. (2005). Panels c-e use data from $z^* = 0$ to $z^* = 1$.

3.4 Discussion

In this section we shall first comment on the potential origin of the many wave packets seen in Figure 3.4 and then discuss the implications of this wave environment for the subsurface mixing environment before and after cyclone Remal.

3.4.1 The origin of internal waves in the Bay of Bengal

The rich near-inertial wave field observed before Remal raises a fundamental question: if wind forcing was negligible during this period, what drove it?

Beyond direct wind forcing, near-inertial internal waves can be generated through a variety of mechanisms: spontaneous emission from unbalanced geostrophic flows (Alford et al., 2013; Vanneste, 2013), loss of balance at submesoscale fronts (Whitt and Thomas, 2015), from radiative instabilities in eddies (Kar et al., 2025), and the so-called "stimulated generation" whereby existing NIWs extract energy from mesoscale eddies through wave-mean flow interaction (Xie and Vanneste, 2015; Wagner and Young, 2016). In each case, the eddy field acts not merely as a passive waveguide that focuses or disperses waves, but as an active participant in wave generation and energy exchange. Recent observational work has also highlighted how meso- and submesoscale background flows can act both as a sink and a source of NIWs depending on the relative strength and phasing of these motions. For example Savage et al. (2025) highlight the bidirectional transfer of energy between background and near-inertial flows in the North Atlantic that show a seasonal dependence. Lastly, Waterhouse et al. (2022) reports that globally about 40% of the near-inertial shear in the upper ocean (above 600m depth) has up-going energy which is inconsistent with direct surface generation from wind forcing.

To identify potential mesoscale sources, we apply a 3-day low-pass filter to the raw Seaglider velocity data, comparable to the local inertial period of 2.3 days. Although the Seaglider is moving through the water rather than freely drifting, and this low passed velocity is thus an along-track representation, we view it as an approximate but nonetheless useful basis for discussing potential origins of the traced rays. The low passed velocities and GLORYS12 relative vorticity reveal several features along the Seaglider track: a shallow submesoscale eddy, a larger-scale eddy, and strong transitions between cyclonic and anticyclonic vorticity. Figure 3.8 overlays rays 1–6 from Figure 3.4h on this velocity field together with the GLORYS12 relative vorticity from Figure 3.4d, and we label the rays in order of appearance in Figure 3.8b. Ray

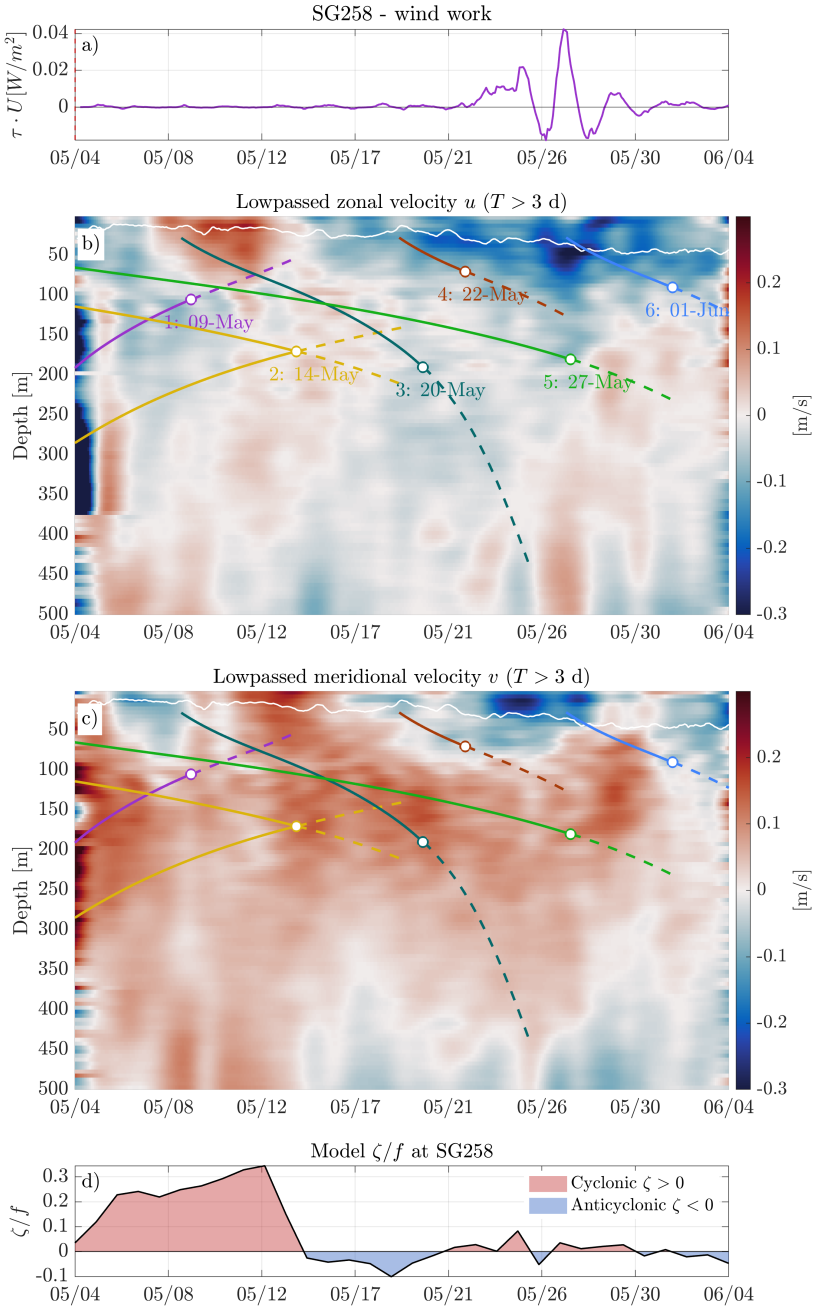


Figure 3.8. a) wind work along the Seaglider track from ERA5 reanalysis winds, lowpassed zonal b) and meridional c) velocities and rays from Figure 3.4h, d) GLORYS12 model relative vorticity along the Seaglider track.

6 represents the only wave packet that could plausibly be associated with cyclone Remal's wind forcing leaving the mixed layer around the time of the forcing impulse. Ray 3 (teal)

traces back to what we hypothesize is a shallow submesoscale eddy based on bowl-shaped, alternating-sign velocities in the upper 100 m. The observation point for ray 2 (yellow) lies on the edge of a depth-uniform, positive meridional (northward) velocity region, broadly consistent with the presence of a larger-scale eddy, and the GLORYS12 vorticity indicates that the Seaglider traverses strong cyclonic and anticyclonic vorticity there. In this region the internal-wave field displays distinct upward- and downward-propagating phase lines, so the vertical propagation direction of this packet is not uniquely constrained.

The origins of the remainder of the rays (1,4,5 in Figure 3.8b) are less clear. Ray 4 (red color) propagates downward from the base of the mixed layer at a time when there is no apparent wind forcing but the sharp gradient in meridional velocity (Figure 3.8c) in the upper 50m of the ocean is perhaps suggesting the presence of a submesoscale front or filament at the edge of the bigger eddy. Ray 5 (green color) has a comparatively slow vertical group velocity (about 5 m/day) and we cannot identify when it left the mixed layer. Ray 1 (purple color) has upward propagating energy and similarly its origin is unclear. There are however a range of wave-wave interactions (Müller et al., 1986) that could also contribute to the total wave environment we observe here. Our observations are only for one month and do not resolve seasonal variability in the internal wave field, though Zhang et al. (2021) report that near-inertial shear on average makes up 50-80% of the total shear in the Bay of Bengal, and that tidal contributions to shear are secondary to those of inertial and sub-inertial motions. Whatever their origin, these wave packets together make up an energetic near-inertial field that conditions the mixing environment during the quiescent pre-storm period. It is against this baseline which we in the following section examine the imprint of cyclone Remal.

3.4.2 Dissipation environment before and after Remal

Cyclone Remal left a selective imprint on the subsurface mixing environment. The overall distributions of ε and Γ only changed marginally before and after the storm (Figures 3.6a and 3.7a). A level of background dissipation, likely sustained by the pre-storm internal

wave field, is present throughout the record. For the active turbulence in particular, stratification increased by about 45% while shear variance more than doubled (figure 3.6), indicating strongly shear driven dissipation, and the associated mixing efficiency lowered slightly (Figure 3.7c).

This is the expected behavior of shear-driven turbulence in a strongly stratified environment. Direct numerical simulations (DNS) show that Kelvin-Helmholtz billows remain geometrically confined to the shear layer, dissipating most of their kinetic energy locally before it can drive irreversible diapycnal mixing, so that Γ falls as shear intensity rises and depends on the geometry of the forcing rather than its intensity alone (Mashayek and Peltier, 2013; Salehipour et al., 2015; Yi and Koseff, 2023). Our observations are consistent with this picture: a doubling of shear variance resulted in a 47% decrease in the bulk estimate of Γ for the active turbulence, suggesting that the post-storm turbulence, while mechanically more intense, remained confined to thin, highly stratified layers where buoyancy suppressed the turbulent cascade and limited irreversible mixing. Since we sampled in the same region but not the exact same location, we cannot track a specific parcel of water or layer to understand what might precondition a specific layer or isopycnal to become an "active layer" after the storm. Natural variability in stratification resulting from freshwater influx, eddy-stirring and previous forcing likely plays a role.

Although the bulk properties of turbulent dissipation ε remained very similar after the storm, the vertical structure changed markedly. The increase in stratification below the mixed layer, that resulted from wind forcing by cyclone Remal deepening the mixed layer by about 18 m, compressed the upper ocean into fewer and thinner layers of active turbulence (Figure 3.6b,c) where the shear variance was strong enough to overcome the local stratification. The Ozmidov scales estimated from median ε and N^2 over three manually identified active turbulence patches in each period yields $L_O \approx 5$ cm in both periods and the equivalent Kolmogorov scales are $\sim 2-5\times10^{-3}$ m. At these scales, where $L_O/\eta_K \sim \mathcal{O}(10)$, buoyancy and viscosity act nearly simultaneously to arrest the turbulent cascade, leaving little room for an inertial subrange. This is the hallmark of the viscosity-affected stratified regime (Smyth and Moum, 2000), and is consistent with the low median Re_b values of 2-3 observed in both periods (Figure 3.7d).

The reorganization of dissipation into fewer, thinner layers after Remal has implications for how that mixing translates into vertical tracer fluxes. In layered stratified turbulence, the effective diapycnal transport depends not only on total dissipation but also on vertical arrangement and thickness of active layers relative to the Ozmidov scale (Caulfield, 2021; Mashayek et al., 2017), a dependence that bulk diffusivity parameterizations typically cannot capture. Most observational evidence for this comes from the abyssal ocean, where the geometry of turbulent patches has been linked to differences in water mass transformation and overturning (Ijichi et al., 2020; Cimoli et al., 2019; De Lavergne et al., 2016); our upper-ocean thermocline observations suggest an analogous sensitivity in that the same total dissipation, reorganized into a more layered structure, need not produce the same buoyancy flux. How large this effect is in the strongly salinity stratified thermocline of the Bay of Bengal, where double diffusion and sharp density interfaces may further modulate the flux-gradient relationship, remains to be established. This layering of the buoyancy flux could carry ecological as well as physical consequences: turbulent nutrient fluxes across the pycnocline sustain productivity in the otherwise oligotrophic Bay of Bengal (Prasanna Kumar et al., 2002; Bhattacharya et al., 2025; Sarma et al., 2016), such that storm forcing that concentrates dissipation into thin, discrete layers may likewise concentrate nutrient supply at specific density surfaces rather than spreading it through the water column.

The results presented here paint a coherent picture of how a strongly stratified basin like the Bay of Bengal responds to episodic forcing. Prior to Remal, an energetic near-inertial wave field - likely stemming from mesoscale and submesoscale flows rather than wind forcing - maintained a background of low-intensity, viscosity-affected turbulence distributed throughout the water column. The storm did not fundamentally alter the turbulent regime: Re_b, L_O, and the Γ-Re_b relationship all remained consistent with a weakly turbulent, stratification-dominated state. What changed was the *geometry* of dissipation: fewer, thinner, more shear-concentrated layers replacing a spatially diffuse background. This distinction matters because it is the vertical structure of dissipation, not just its bulk magnitude, that models must ultimately capture to accurately describe fluxes. The pre-storm wave environment also suggests that the internal

wave energy budget in the Bay of Bengal may be substantially supplied by sources absent from wind-forced parameterization schemes, underscoring the need for models that explicitly resolve mesoscale-wave interactions.

3.5 Conclusion

The 2024 EKAMSAT field campaign provided an opportunity to study the ocean's response to episodic forcing, captured through concurrent microstructure, velocity, and density observations before and after severe cyclonic storm Remal in the Bay of Bengal. Prior to any storm forcing, we observed an energetic near-inertial internal wave field whose ray-traced origins implicate mesoscale and submesoscale flows, suggesting that the internal wave energy budget in the pre-monsoon Bay of Bengal is at least in part supplied by sources absent from wind-only parameterization schemes. The storm itself reorganized the subsurface dissipation field into fewer, thinner, more shear-concentrated layers with low Γ values but without substantially altering bulk dissipation rates or the Γ–Re_b relationship. Ozmidov scales of $\sim$5 cm and median Re_b of 2–3 in both periods confirm that turbulence remained in the viscosity-affected, strongly stratified regime throughout. These findings suggest that in the Bay of Bengal, storm forcing reshapes the geometry of turbulence more than its bulk magnitude which is a distinction with potential consequences for barrier layer erosion, SST evolution, and monsoon heat flux. Current mixing parameterizations that capture column-integrated dissipation but not its vertical coherence will misplace where in the water column mixing actually occurs. Closing this gap, along with better representation of non-wind internal wave generation in models, and alongside better representation of mesoscale-driven NIW generation, would represent a meaningful step toward improved predictions of phenomena where air-sea interactions play a key role, such as the monsoon.

Acknowledgments

This material is in full a reprint of a manuscript being prepared for publication as Bergentz, K., MacKinnon, J., Lucas, A. J., Rainville, L., Kannad, A., Pereira, F., Alford, M. H., Le Boyer, A. 2026, Stratified and Stormy in the Bay of Bengal – Internal Waves and Turbulence Before and After Cyclone Remal, Journal of Geophysical Research: Oceans 2026. The dissertation author was the primary investigator and author of this paper. We wish to thank the captain and crew aboard the R/V Thomas G. Thompson as well as the entire EKAMSAT project team at sea and on land who helped with the collection of the data presented.

Appendix A: raw shear

Here we present Figures showing the unfiltered shear used to make Figures 3.3-3.4. We compute shear by differencing the velocity in depth, and plot the sum of the two component spectra, $\Phi[u_z] + \Phi[v_z]$, whose integral is the total shear variance $\langle u_z^2 + v_z^2 \rangle$ and which is therefore invariant under rotation of the horizontal coordinate frame. the native resolution of the Seaglider is 2 h and 5 m, and the DBASIS 0.5 h and 1 m which we bin to 5 m to facilitate comparison with the Seaglider. Frequency spectra were computed for all 5 m bins using Hann windowed 7.2 day segments with 50% overlap, and then averaged. Wavenumber spectra (Figure 3.10b) were computed by Fourier transforming each shear profile over 50-500 m and averaging over the full record. Spectra have been corrected for the $\mathrm{sinc}^2(m\,dz)$ attenuation of the first-difference operator so that platforms with different bin thicknesses are directly comparable. Shaded bands are 95% confidence intervals on the ensemble mean. The raw Seaglider and WW2 data both suggest the presence of a strong, across depth and time, near-inertial signal (Figure 3.9a), which is further clarified in Figure 3.3. The Seaglider and WW2 instruments have peaks at a wavelength of 45 m (used in the ray tracing of the Seaglider described in section 3.2.2) and 20 m (identified as a common wavelength in Figure 3.3) respectively.

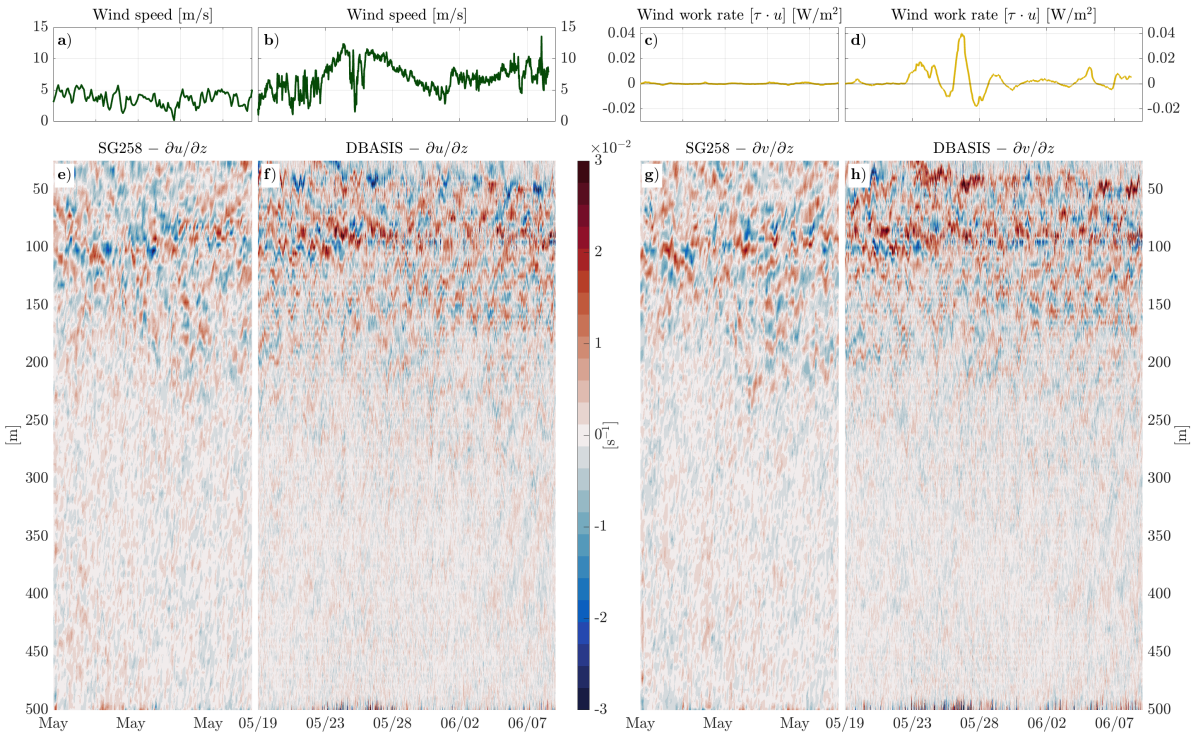


Figure 3.9. Same as Figure 3.3 but showing the unfiltered shear from the Seaglider and WW2. Panel a-b) show ERA5 wind speed at the SG and WW2 locations respectively, c-d) the same but wind work. Panel e-f) zonal shear du/dz SG and WW2 respectively, and panel g-h) the meridional shear dv/dz.

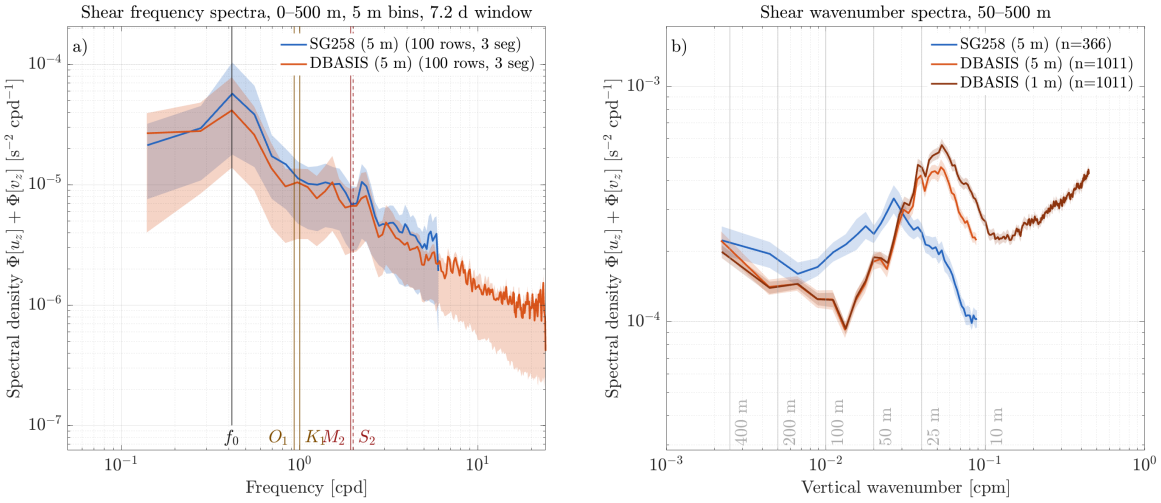


Figure 3.10. a) Frequency spectra from DBASIS and the Seaglider 0-500m averaged over 5m vertical bins, b) wavenumber spectra for the Seaglider and DBASIS native vertical resolution of 1m and binned to 5m.

Bibliography

Alford, M. H. (2001). Internal swell generation: The spatial distribution of energy flux from the wind to mixed layer near-inertial motions. *Journal of Physical Oceanography*, 31(8):2359 – 2368.

Alford, M. H. (2003). Improved global maps and 54-year history of wind-work on ocean inertial motions. *Geophysical Research Letters*, 30(8).

Alford, M. H. (2020). Revisiting near-inertial wind work: Slab models, relative stress, and mixed layer deepening. *Journal of Physical Oceanography*, 50(11):3141 – 3156.

Alford, M. H., Cronin, M. F., and Klymak, J. M. (2012). Annual Cycle and Depth Penetration of Wind-Generated Near-Inertial Internal Waves at Ocean Station Papa in the Northeast Pacific. *Journal of Physical Oceanography*, 42(6):889–909.

Alford, M. H. and Gregg, M. C. (2001). Near-inertial mixing: Modulation of shear, strain and microstructure at low latitude. *Journal of Geophysical Research: Oceans*, 106:16947–16968.

Alford, M. H., MacKinnon, J. A., Simmons, H. L., and Nash, J. D. (2016). Near-Inertial Internal Gravity Waves in the Ocean. *Annual Review of Marine Science*, 8(1):95–123.

Alford, M. H., Shcherbina, A. Y., and Gregg, M. C. (2013). Observations of near-inertial internal gravity waves radiating from a frontal jet. *Journal of physical oceanography*, 43(6):1225–1239.

Alford, M. H., Wynne-Cattanach, B., Le Boyer, A., Couto, N., Voet, G., Spingys, C. P., Fernandez Castro, B., Forryan, A., Naveira Garabato, A. C., and Van Haren, H. (2025). Buoyancy Flux and Mixing Efficiency from Direct, Near-Bottom Turbulence Measurements in a Submarine Canyon. *Journal of Physical Oceanography*, 55(2):97–118.

Aravind, H. M., Ozgokmen, T., and Allshouse, M. (2024). Lagrangian analysis of submesoscale flows from sparse data using Gaussian Process Regression for field reconstruction.

Asselin, O. and Young, W. R. (2020). Penetration of wind-generated near-inertial waves into a turbulent ocean. *Journal of Physical Oceanography*, 50(6):1699–1716.

Ballarotta, M., Ubelmann, C., Pujol, M.-I., Taburet, G., Fournier, F., Legeais, J.-F., Faugère, Y., Delepoulle, A., Chelton, D., Dibarboure, G., and Picot, N. (2019). On the resolutions of ocean altimetry maps. *Ocean Science*, 15(4):1091–1109.

Barkan, R., Srinivasan, K., and McWilliams, J. C. (2024). Eddy–internal wave interactions: Stimulated cascades in cross-scale kinetic energy and enstrophy fluxes. *Journal of Physical Oceanography*, 54(6):1309–1326.

Barkan, R., Winters, K. B., and McWilliams, J. C. (2017). Stimulated imbalance and the enhancement of eddy kinetic energy dissipation by internal waves. *Journal of Physical Oceanography*, 47(1):181–198.

Bashmachnikov, I., Sokolovskiy, M., Belonenko, T., Volkov, D., Isachsen, P., and Carton, X. (2017). On the vertical structure and stability of the lofoten vortex in the norwegian sea. *Deep Sea Research Part I: Oceanographic Research Papers*, 128:1–27.

Batchelor, G. K. (1967). *An Introduction to Fluid Dynamics*. Cambridge University Press, Cambridge, UK.

Berta, M., Griffa, A., Haza, A. C., Horstmann, J., Huntley, H. S., Ibrahim, R., Lund, B., Özgökmen, T. M., and Poje, A. C. (2020). Submesoscale kinematic properties in summer and winter surface flows in the northern gulf of mexico. *Journal of Geophysical Research: Oceans*, 125(10):e2020JC016085.

Berta, M., Griffa, A., Özgökmen, T. M., and Poje, A. C. (2016). Submesoscale evolution of surface drifter triads in the gulf of mexico. *Geophysical Research Letters*, 43(22):11,751–11,759.

Bhattacharya, T., Ghosal, P. K., and Chakraborty, K. (2025). Biogeochemical Response to Tropical Cyclones in the Northern Indian Ocean: Understanding and Gray Areas. *Journal of Geophysical Research: Oceans*, 130(8):e2025JC022540.

Bian, C., Jing, Z., Wang, H., Wu, L., Chen, Z., Gan, B., and Yang, H. (2023). Oceanic mesoscale eddies as crucial drivers of global marine heatwaves. *Nature Communications*, 14(1):2970.

Bigg, G. R., Jickells, T. D., Liss, P. S., and Osborn, T. J. (2003). The role of the oceans in climate. *International Journal of Climatology*, 23(10):1127–1159.

Bosse, A., Fer, I., Lilly, J. M., and Søiland, H. (2019). Dynamical controls on the longevity of a non-linear vortex : The case of the Lofoten Basin Eddy. *Scientific Reports*, 9(1):13448.

Byrd, R. H., Lu, P., Nocedal, J., and Zhu, C. (1995). A limited memory algorithm for bound constrained optimization. *SIAM Journal on Scientific Computing*, 16(5):1190–1208.

Carton, X. (2001). Hydrodynamical Modeling Of Oceanic Vortices. *Surveys in Geophysics*, 22(3):179–263.

Caulfield, C. (2021). Layering, Instabilities, and Mixing in Turbulent Stratified Flows. *Annual Review of Fluid Mechanics*, 53(1):113–145.

Centurioni, L. (2018). *Drifter Technology and Impacts for Sea Surface Temperature, Sea-Level Pressure, and Ocean Circulation Studies*, pages 37–57. Springer.

Chaudhuri, D., Sengupta, D., D'Asaro, E., Farrar, J. T., Mathur, M., and Ranganathan, S. (2024). Near-Inertial Response of a Salinity-Stratified Ocean. *Journal of Physical Oceanography*, 54(9):1841–1855.

Chelton, D. B., Schlax, M. G., Samelson, R. M., and De Szoeke, R. A. (2007). Global observations of large oceanic eddies. *Geophysical Research Letters*, 34(15):2007GL030812.

Cherian, D. A., Shroyer, E. L., Wijesekera, H. W., and Moum, J. N. (2020). The Seasonal Cycle of Upper-Ocean Mixing at 8°N in the Bay of Bengal. *Journal of Physical Oceanography*, 50(2):323–342.

Cimoli, L., Caulfield, C. P., Johnson, H. L., Marshall, D. P., Mashayek, A., Naveira Garabato, A. C., and Vic, C. (2019). Sensitivity of Deep Ocean Mixing to Local Internal Tide Breaking and Mixing Efficiency. *Geophysical Research Letters*, 46(24):14622–14633.

Cimoli, L., Mashayek, A., Naveira Garabato, A. C., Caulfield, C.-c. P., Alford, M. H., Baker, L., Cael, B. B., Fernández Castro, B., De Lavergne, C., Ellison, E., Gebbie, G., Gula, J., Heimbach, P., Lanham, J., Le Boyer, A., Oglethorpe, K., Peltier, W. R., Pillar, H. R., Piotrowski, A. M., Purkey, S. G., Reynard, N., Shuckburgh, E., Siegert, M. J., Silvano, A., Skinner, L. C., Spingys, C. P., Talley, L. D., Taylor, J. R., Voet, G., Williams, R. G., Wilson, C., and Wynne-Cattanach, B. L. (2026). Climatic reach of small-scale turbulence in the ocean interior. *Nature Communications*, 17(1):5212.

Cliff, N. (1993). Dominance statistics: Ordinal analyses to answer ordinal questions. *Psychological Bulletin*, 114(3):494–509.

Conn, S. and Callies, J. (2026). Global Near-Inertial Wave Spectra Shaped by Mesoscale Eddies. *Journal of Physical Oceanography*, 56(3):707–724.

Conn, S., Fitzgerald, J., and Callies, J. (2024). Interpreting Observed Interactions between Near-Inertial Waves and Mesoscale Eddies. *Journal of Physical Oceanography*, 54(2):485–502.

Copernicus Climate Change Service, Climate Data Store (2023). ERA5 hourly data on single levels from 1940 to present.

Cushman-Roisin, B. (1987). Exact analytical solutions for elliptical vortices of the shallow-water equations. *Tellus A*, 39(3):235–244.

Cuypers, Y., Bouruet-Aubertot, P., Marec, C., and Fuda, J.-L. (2012). Characterization of turbulence from a fine-scale parameterization and microstructure measurements in the Mediterranean Sea during the BOUM experiment. *Biogeosciences*, 9(8):3131–3149.

D'Asaro, E. A. (1985). The energy flux from the wind to near-inertial motions in the surface mixed layer. *Journal of Physical Oceanography*, 15(8):1043 – 1059.

D'Asaro, E. A. (1995). Upper-ocean inertial currents forced by a strong storm. part iii: Interaction of inertial currents and mesoscale eddies. *Journal of Physical Oceanography*, 25(11):2953 – 2958.

De Lavergne, C., Madec, G., Le Sommer, J., Nurser, A. J. G., and Naveira Garabato, A. C. (2016). The Impact of a Variable Mixing Efficiency on the Abyssal Overturning. *Journal of Physical Oceanography*, 46(2):663–681.

De Marez, C. (2025). Synoptic observation of a full mesoscale eddy lifetime and its secondary instabilities in the Gulf of Mexico. *Ocean Science*, 21(5):1933–1942.

De Marez, C., Le Corre, M., and Gula, J. (2021). The influence of merger and convection on an anticyclonic eddy trapped in a bowl. *Ocean Modelling*.

Delpech, A., Barkan, R., Srinivasan, K., McWilliams, J. C., Arbic, B. K., Siyanbola, O. Q., and Buijsman, M. C. (2024). Eddy–Internal Wave Interactions and Their Contribution to Cross-Scale Energy Fluxes: A Case Study in the California Current. *Journal of Physical Oceanography*, 54(3):741–754.

Dommenget, D. (2010). The slab ocean el niño. *Geophysical Research Letters*, 37(20).

Dong, C., You, Z., Dong, J., Ji, J., Sun, W., Xu, G., Lu, X., Xie, H., Teng, F., Liu, Y., Xu, A., Wang, Q., Xia, Q., Lin, X., Fu, M., Wang, J., Cao, Y., and Han, G. (2025a). Oceanic Mesoscale Eddies. *Ocean-Land-Atmosphere Research*, 4:0081.

Dong, H., Zhou, M., McWilliams, J. C., Raj, R. P., d'Ovidio, F., Fer, I., Qu, L., Qiu, B., Siegelman, L., Zhang, Z., Smith, W. O., and Sperrevik, A. K. (2025b). Warm rings in mesoscale eddies in a cold straining ocean. *Nature Communications*, 16(1):9252.

Dove, L. and Freilich, M. (2026). Biophysical Dynamics of Mesoscale Eddies: Coincident Observations from SWOT and PACE. *Oceanography*, 39(1).

Du, T., Zhang, Y., Su, W., Jing, Z., Chen, Z., Qiu, Y., Zhang, H., Yang, S., and Ma, W. (2025). Three-Dimensional Observations of a Mesoscale Eddy in the Kuroshio Extension Based on

Multiple Platforms. *Scientific Data*, 12(1):2013.

Elipot, S., Lumpkin, R., and Prieto, G. (2010). Modification of inertial oscillations by the mesoscale eddy field. *Journal of Geophysical Research: Oceans*, 115(C9):2009JC005679.

Ernst, P. A., Subrahmanyam, B., Trott, C. B., and Chaigneau, A. (2023). Characteristics of submesoscale eddy structures within mesoscale eddies in the Gulf of Mexico from 1/48° ECCO estimates. *Frontiers in Marine Science*, 10:1181676.

Esposito, G., Berta, M., Centurioni, L., Johnston, T. S., Lodise, J., Özgökmen, T., Poulain, P.-M., and Griffa, A. (2021). Submesoscale vorticity and divergence in the alboran sea: Scale and depth dependence. *Frontiers in Marine Science*, 8.

Essink, S., Hormann, V., Centurioni, L. R., and Mahadevan, A. (2022). On Characterizing Ocean Kinematics from Surface Drifters. *Journal of Atmospheric and Oceanic Technology*, 39(8):1183–1198.

E.U. Copernicus Marine Service Information (CMEMS) (2023). Global ocean physics reanalysis (GLORYS12V1).

E.U. Copernicus Marine Service Information (CMEMS) (2024). Multi observation global ocean 3D temperature salinity height geostrophic current and MLD.

Fer, I., Bosse, A., Ferron, B., and Bouruet-Aubertot, P. (2018). The dissipation of kinetic energy in the lofoten basin eddy. *Journal of Physical Oceanography*, 48(6):1299 – 1316.

Ferrari, R. and Wunsch, C. (2009). Ocean circulation kinetic energy: Reservoirs, sources, and sinks. *Annual Review of Fluid Mechanics*, 41:253–282.

Flexas, M. M., Thompson, A. F., Torres, H. S., Klein, P., Farrar, J. T., Zhang, H., and Menemenlis, D. (2019). Global estimates of the energy transfer from the wind to the ocean, with emphasis on near-inertial oscillations. *Journal of Geophysical Research: Oceans*, 124(8):5723–5746.

Fofonoff, N. (1969). Spectral characteristics of internal waves in the ocean. *Deep-Sea Res.*, 16:58–71.

Fu, L., Pavelsky, T., Cretaux, J., Morrow, R., Farrar, J. T., Vaze, P., Sengenes, P., Vinogradova-Shiffer, N., Sylvestre-Baron, A., Picot, N., and Dibarboure, G. (2024). The Surface Water and Ocean Topography Mission: A Breakthrough in Radar Remote Sensing of the Ocean and Land Surface Water. *Geophysical Research Letters*, 51(4):e2023GL107652.

Furuichi, N., Hibiya, T., and Niwa, Y. (2008). Model-predicted distribution of wind-induced internal wave energy in the world's oceans. *Journal of Geophysical Research: Oceans*, 113(C9):2008JC004768.

Gandin, L. (1966). Objective analysis of meteorological fields. By L. S. Gandin. Translated from the Russian. Jerusalem (Israel Program for Scientific Translations), 1965. Pp. vi, 242: 53 Figures; 28 Tables. £4 1s. 0d. *Quarterly Journal of the Royal Meteorological Society*, 92(393):447–447.

Gent, P. R. and Mcwilliams, J. C. (1990). Isopycnal Mixing in Ocean Circulation Models. *Journal of Physical Oceanography*, 20(1):150–155.

George, J. V., Vinayachandran, P. N., and Nayak, A. A. (2021). Enhanced Double-Diffusive Salt Flux from the High-Salinity Core of Arabian Sea Origin Waters to the Bay of Bengal. *Journal of Physical Oceanography*, 51(2):505–518.

Girishkumar, M. S., Joseph, J., Thangaprakash, V. P., Pottapinjara, V., and McPhaden, M. J. (2017). Mixed Layer Temperature Budget for the Northward Propagating Summer Monsoon Intraseasonal Oscillation (MISO) in the Central Bay of Bengal. *Journal of Geophysical Research: Oceans*, 122(11):8841–8854.

Gonçalves, R. C., Iskandarani, M., Özgökmen, T., and Thacker, W. C. (2019). Reconstruction of Submesoscale Velocity Field from Surface Drifters. *Journal of Physical Oceanography*, 49(4):941–958.

Gordeeva, S., Zinchenko, V., Koldunov, A., Raj, R. P., and Belonenko, T. (2021). Statistical analysis of long-lived mesoscale eddies in the Lofoten basin from satellite altimetry. *Advances in Space Research*, 68(2):364–377.

GPy (2012). GPy: A gaussian process framework in python. http://github.com/SheffieldML/GPy. Sheffield Machine Learning Group.

Gregg, M. C. (1989). Scaling turbulent dissipation in the thermocline. *Journal of Geophysical Research: Oceans*, 94(C7):9686–9698.

Gregg, M. C., D'Asaro, E. A., Riley, J. J., and Kunze, E. (2018). Mixing Efficiency in the Ocean. *Annual Review of Marine Science*, 10(Volume 10, 2018):443–473.

Gregg, M. C., Seim, H. E., and Percival, D. B. (1993). Statistics of Shear and Turbulent Dissipation Profiles in Random Internal Wave Fields. *Journal of Physical Oceanography*, 23(8):1777–1799.

Grisolía, D. and Martínez-Marrero, A. (2026). A Lagrangian Description of Pulsation, Tilting, Axisymmetrization, and Meandering Trajectory in an Anticyclonic Eddy. *Journal of Geophysical Research: Oceans*, 131(2):e2025JC022878.

Gupta, M., Williams, R. G., Lauderdale, J. M., Jahn, O., Hill, C., Dutkiewicz, S., and Follows, M. J. (2022). A nutrient relay sustains subtropical ocean productivity. *Proceedings of the*

National Academy of Sciences, 119(41):e2206504119.

Hersbach, H., Cobb, A., Kaandorp, M., Poli, P., Bell, B., Berrisford, P., Biavati, G., Horányi, A., Muñoz Sabater, J., Nicolas, J., Peubey, C., Radu, R., Rozum, I., Schepers, D., Simmons, A., Soci, C., Dee, D., and Thépaut, J.-N. (2025). Era5 hourly time-series data on single levels from 1940 to present. Copernicus Climate Change Service (C3S) Climate Data Store (CDS). Reanalysis dataset.

Hersbach, H. et al. (2020). ERA5 global reanalysis. *Quarterly Journal of the Royal Meteorological Society*, 146(730):1999–2049.

Hewitt, H. T., Roberts, M., Mathiot, P., Biastoch, A., Blockley, E., Chassignet, E. P., Fox-Kemper, B., Hyder, P., Marshall, D. P., Popova, E., Treguier, A.-M., Zanna, L., Yool, A., Yu, Y., Beadling, R., Bell, M., Kuhlbrodt, T., Arsouze, T., Bellucci, A., Castruccio, F., Gan, B., Putrasahan, D., Roberts, C. D., Van Roekel, L., and Zhang, Q. (2020). Resolving and Parameterising the Ocean Mesoscale in Earth System Models. *Current Climate Change Reports*, 6(4):137–152.

Hilditch, J. P., Taylor, J. R., and Thomas, L. N. (2025). Refraction of near-inertial waves by submesoscale vorticity filaments. *Journal of Fluid Mechanics*, 1020:A9.

Holte, J., Talley, L. D., Gilson, J., and Roemmich, D. (2017). An argo mixed layer climatology and database. *Geophysical Research Letters*, 44(11):5618–5626.

Hummon, J. M., Firing, E., Gum, J., de Pinho, U., Roc, T., Vadnais, D., Ash, J., Frambach, D., Goulart, A., and Martin, T. (2023). Codas+uhdas documentation.

Ijichi, T., St. Laurent, L., Polzin, K. L., and Toole, J. M. (2020). How Variable Is Mixing Efficiency in the Abyss? *Geophysical Research Letters*, 47(7):e2019GL086813.

India Meteorological Department (2024). Southwest monsoon 2024: Southern peninsular india. Technical report, India Meteorological Department, Regional Meteorological Centre, Chennai, India.

Ivey, G., Winters, K., and Koseff, J. (2008). Density Stratification, Turbulence, but How Much Mixing? *Annual Review of Fluid Mechanics*, 40(1):169–184.

Ivey, G. N. and Imberger, J. (1991). On the nature of turbulence in a stratified fluid. Part I: The energetics of mixing. *Journal of Physical Oceanography*, 21(5):650–658.

Jean-Michel, L., Eric, G., Romain, B.-B., Gilles, G., Angélique, M., Marie, D., Clément, B., Mathieu, H., Olivier, L. G., Charly, R., Tony, C., Charles-Emmanuel, T., Florent, G., Giovanni, R., Mounir, B., Yann, D., and Pierre-Yves, L. T. (2021). The Copernicus Global 1/12° Oceanic and Sea Ice GLORYS12 Reanalysis. *Frontiers in Earth Science*, 9:698876.

Jiang, J., Lu, Y., and Perrie, W. (2005). Estimating the energy flux from the wind to ocean inertial motions: The sensitivity to surface wind fields. *Geophysical Research Letters*, 32(15):2005GL023289.

Jing, Z., Wu, L., and Ma, X. (2017). Energy exchange between the mesoscale oceanic eddies and wind-forced near-inertial oscillations. *Journal of Physical Oceanography*, 47(3):721 – 733.

Jochum, M., Briegleb, B. P., Danabasoglu, G., Large, W. G., Norton, N. J., Jayne, S. R., Alford, M. H., and Bryan, F. O. (2013). The impact of oceanic near-inertial waves on climate. *Journal of Climate*, 26(9):2833–2844.

Johnson, L., Tandon, A., Lee, C., Kumar, T. S., Mohapatra, M., Rao, S. A., Chen, S., Fernando, H. J. S., and Goes, J. (2025). A Collaborative Effort toward Understanding the Air–Sea Transition Zone during the Indian Summer Monsoon. *Bulletin of the American Meteorological Society*, 106(12):E2509–E2518.

Kachelein, L., Wang, J., Lucas, A. J., Delpech, A., Farrar, J. T., Archer, M., Lankhorst, M., Tchonang, B. C., Send, U., Stalin, S., et al. (2025). Sub-100 km ocean processes revealed by structure functions of swot sea surface height and in situ observing network. *Journal of Geophysical Research: Oceans*, 130(11):e2025JC022639.

Kafiabad, H. A., Vanneste, J., and Young, W. R. (2021). Interaction of near-inertial waves with an anticyclonic vortex. *Journal of Physical Oceanography*.

Kar, M., Mukhopadhyay, J., and Deb Sarkar, M. (2021). South Asia and Climate Change: Unravelling the Conundrum.

Kar, S., Barkan, R., McWilliams, J. C., and Molemaker, M. J. (2025). Spontaneous Emission of Internal Waves by a Radiative Instability. *Journal of Physical Oceanography*, 55(5):525–542.

Kerhalkar, S., Tandon, A., Farrar, J. T., MacKinnon, J. A., Schlosser, T. L., Johnson, L., Lucas, A. J., Hormann, V., and Centurioni, L. R. (2026). Modulation of diurnal sst and diurnal warm layer variability by salinity-driven stratification in the bay of bengal. *Journal of physical oceanography*, 56(1):245–266.

Klein, P., Lapeyre, G., and Large, W. G. (2004). Wind ringing of the ocean in presence of mesoscale eddies. *Geophysical Research Letters*, 31(15).

Klenz, T., Simmons, H. L., Centurioni, L., Lilly, J. M., Early, J. J., and Hormann, V. (2022). Estimates of near-inertial wind power input using novel in situ wind measurements from minimet surface drifters in the iceland basin. *Journal of Physical Oceanography*, 52(10):2417 – 2430.

Köhl, A. (2007). Generation and stability of a quasi-permanent vortex in the lofoten basin.

Journal of Physical Oceanography, 37(11):2637 – 2651.

Kunze, E. (1985). Near-Inertial Wave Propagation In Geostrophic Shear. *Journal of Physical Oceanography*, 15(5):544–565.

Kunze, E., Schmitt, R. W., and Toole, J. M. (1995). The energy balance in a warm-core ring's near-inertial critical layer. *Journal of Physical Oceanography*, 25(5):942 – 957.

Large, W. G. and Pond, S. (1981). Open ocean momentum flux measurements in moderate to strong winds. *Journal of Physical Oceanography*, 11(3):324 – 336.

Le Boyer, A., Alford, M. H., Couto, N., Goldin, M., Lastuka, S., Goheen, S., Nguyen, S., Lucas, A. J., and Hennon, T. D. (2021). Modular, Flexible, Low-Cost Microstructure Measurements: The Epsilometer. *Journal of Atmospheric and Oceanic Technology*, 38(3):657–668.

Leaman, K. D. and Sanford, T. B. (1975). Vertical energy propagation of inertial waves: A vector spectral analysis of velocity profiles. *Journal of Geophysical Research*, 80(15):1975–1978.

Lee, D.-K. and Niiler, P. P. (1998). The inertial chimney: The near-inertial energy drainage from the ocean surface to the deep layer. *Journal of Geophysical Research: Oceans*, 103(C4):7579–7591.

Lilly, J. and Olhede, S. (2010). Bivariate Instantaneous Frequency and Bandwidth. *IEEE Transactions on Signal Processing*, 58(2):591–603.

Lilly, J. M. (2021). jlab: A data analysis package for matlab, v.1.7.1.

Lilly, J. M. (2024). jlab: A data analysis package for matlab.

Lilly, J. M. and Olhede, S. C. (2009). Wavelet ridge estimation of jointly modulated multivariate oscillations. In *2009 Conference Record of the Forty-Third Asilomar Conference on Signals, Systems and Computers*, page 452–456, Pacific Grove, CA. IEEE. http://www.ieee.org/publications_standards/publications/rights/rights_policies.html.

Lilly, J. M. and Olhede, S. C. (2012). Analysis of modulated multivariate oscillations. *Signal Processing, IEEE Transactions on*, 60:600–612.

Lilly, J. M. and Pérez-Brunius, P. (2021). Extracting statistically significant eddy signals from large lagrangian datasets using wavelet ridge analysis, with application to the gulf of mexico. *Nonlinear Processes in Geophysics*, 28(2):181–212.

Liu, Y., Jing, Z., and Wu, L. (2019). Wind power on oceanic near-inertial oscillations in the global ocean estimated from surface drifters. *Geophysical Research Letters*, 46(5):2647–2653.

Lodise, J., Özgökmen, T., Gonçalves, R. C., Iskandarani, M., Lund, B., Horstmann, J., Poulain, P.-M., Klymak, J., Ryan, E. H., and Guigand, C. (2020). Investigating the Formation of Submesoscale Structures along Mesoscale Fronts and Estimating Kinematic Quantities Using Lagrangian Drifters. *Fluids*, 5(3):159.

Lucas, A., Nash, J., Pinkel, R., MacKinnon, J., Tandon, A., Mahadevan, A., Omand, M., Freilich, M., Sengupta, D., Ravichandran, M., and Le Boyer, A. (2016). Adrift Upon a Salinity-Stratified Sea: A View of Upper-Ocean Processes in the Bay of Bengal During the Southwest Monsoon. *Oceanography*, 29(2):134–145.

Luecke, C. A., Wijesekera, H. W., Jarosz, E., Wang, D. W., Wesson, J. C., Jinadasa, S., Fernando, H. J. S., and Teague, W. J. (2021). Observations of Eddy-Modulated Turbulent Mixing in the Southern Bay of Bengal. *Journal of Physical Oceanography*.

MacKinnon, J. A., Zhao, Z., Whalen, C. B., Waterhouse, A. F., Trossman, D. S., Sun, O. M., Laurent, L. C. S., Simmons, H. L., Polzin, K., Pinkel, R., et al. (2017). Climate process team on internal wave–driven ocean mixing. *Bulletin of the American Meteorological Society*, 98(11):2429–2454.

Marques, G. M., Loose, N., Yankovsky, E., Steinberg, J. M., Chang, C.-Y., Bhamidipati, N., Adcroft, A., Fox-Kemper, B., Griffies, S. M., Hallberg, R. W., Jansen, M. F., Khatri, H., and Zanna, L. (2022). NeverWorld2: an idealized model hierarchy to investigate ocean mesoscale eddies across resolutions. *Geoscientific Model Development*, 15(17):6567–6579.

Mashayek, A., Caulfield, C., and Alford, M. (2021). Goldilocks mixing in oceanic shear-induced turbulent overturns. *Journal of Fluid Mechanics*, 928:A1.

Mashayek, A. and Peltier, W. R. (2013). Shear-induced mixing in geophysical flows: does the route to turbulence matter to its efficiency? *Journal of Fluid Mechanics*, 725:216–261.

Mashayek, A., Salehipour, H., Bouffard, D., Caulfield, C. P., Ferrari, R., Nikurashin, M., Peltier, W. R., and Smyth, W. D. (2017). Efficiency of turbulent mixing in the abyssal ocean circulation. *Geophysical Research Letters*, 44(12):6296–6306.

Mater, B. D. and Venayagamoorthy, S. K. (2014). A unifying framework for parameterizing stably stratified shear-flow turbulence. *Physics of Fluids*, 26(3):036601.

McKie, T., Lucas, A. J., and MacKinnon, J. (2024). Submesoscale Dynamics in the Bay of Bengal: Inversions and Instabilities. *Journal of Geophysical Research: Oceans*, 129(3):e2023JC020563.

McWilliams, J. C. (2016). Submesoscale currents in the ocean. *Proceedings of the Royal Society A: Mathematical, Physical and Engineering Sciences*, 472(2189):20160117.

Molinari, R. and Kirwan, A. D. (1975). Calculations of differential kinematic properties from lagrangian observations in the western caribbean sea. *Journal of Physical Oceanography*, 5(3):483 – 491.

Monismith, S. G., Koseff, J. R., and White, B. L. (2018). Mixing Efficiency in the Presence of Stratification: When Is It Constant? *Geophysical Research Letters*, 45(11):5627–5634.

Müller, P., Holloway, G., Henyey, F., and Pomphrey, N. (1986). Nonlinear interactions among internal gravity waves. *Reviews of Geophysics*, 24(3):493–536.

Murphy, A. H. (1988). Skill Scores Based on the Mean Square Error and Their Relationships to the Correlation Coefficient. *Monthly Weather Review*, 116(12):2417–2424.

Nardelli, B. B. (2013). Vortex waves and vertical motion in a mesoscale cyclonic eddy: Vortex Waves in a Mesoscale Eddy. *Journal of Geophysical Research: Oceans*, 118(10):5609–5624.

Niiler, P. P., Sybrandy, A. S., Bi, K., Poulain, P. M., and Bitterman, D. (1995). Measurements of the water-following capability of holey-sock and tristar drifters. *Deep Sea Research Part I: Oceanographic Research Papers*, 42(11):1951–1964.

NOAA National Centers for Environmental Information (2024). Monthly tropical cyclones report for May 2024.

Oakey, N. S. (1982). Determination of the rate of dissipation of turbulent energy from simultaneous temperature and velocity shear microstructure measurements. *Journal of Physical Oceanography*, 12(3):256–271.

Okubo, A. and Ebbesmeyer, C. C. (1976). Determination of vorticity, divergence, and deformation rates from analysis of drogue observations. *Deep Sea Research and Oceanographic Abstracts*, 23(4):349–352.

Olbers, D., Jurgenowski, P., and Eden, C. (2020). A wind-driven model of the ocean surface layer with wave radiation physics. *Ocean Dynamics*, 70(8):1067–1088.

Osborn, T. R. (1980). Estimates of the local rate of vertical diffusion from dissipation measurements. *Journal of Physical Oceanography*, 10(1):83–89.

Osborn, T. R. and Cox, C. S. (1972). Oceanic fine structure. *Geophysical Fluid Dynamics*, 3(4):321–345.

Oscroft, S., Sykulski, A. M., and Early, J. J. (2020). Separating Mesoscale and Submesoscale Flows from Clustered Drifter Trajectories. *Fluids*, 6(1):14.

Padman, L. and Erofeeva, S. (2004). A barotropic inverse tidal model for the arctic ocean.

Geophysical Research Letters, 31(2).

Park, J. and Watts, D. R. (2005). Near-inertial oscillations interacting with mesoscale circulation in the southwestern Japan/East Sea. *Geophysical Research Letters*, 32(10):2005GL022936.

Pearson, B., Fox-Kemper, B., Bachman, S., and Bryan, F. (2017). Evaluation of scale-aware subgrid mesoscale eddy models in a global eddy-rich model. *Ocean Modelling*, 115:42–58.

Pham, H. T., Sarkar, S., Johnson, L., Fox-Kemper, B., Sullivan, P. P., and Li, Q. (2023). Multi-Scale Temporal Variability of Turbulent Mixing During a Monsoon Intra-Seasonal Oscillation in the Bay of Bengal: An LES Study. *Journal of Geophysical Research: Oceans*, 128(1):e2022JC018959.

Pinkel, R., Goldin, M. A., Smith, J. A., Sun, O. M., Aja, A. A., Bui, M. N., and Hughen, T. (2011). The Wirewalker: A Vertically Profiling Instrument Carrier Powered by Ocean Waves. *Journal of Atmospheric and Oceanic Technology*, 28(3):426–435.

Plueddemann, A. and Farrar, J. (2006). Observations and models of the energy flux from the wind to mixed-layer inertial currents. *Deep Sea Research Part II: Topical Studies in Oceanography*, 53(1):5–30.

Pollard, R. and Millard, R. (1970). Comparison between observed and simulated wind-generated inertial oscillations. *Deep Sea Research and Oceanographic Abstracts*, 17(4):813–821.

Poulain, P.-M. and Centurioni, L. (2015). Direct measurements of world ocean tidal currents with surface drifters. *Journal of Geophysical Research: Oceans*, 120(10):6986–7003.

Poulain, P.-M., Menna, M., Mauri, E., Pirro, A., Hayes, D. R., and Gildor, H. (2023). Drifter observations of surface currents in the cyprus gyre. *Frontiers in Marine Science*, 10.

Prasanna Kumar, S., Muraleedharan, P. M., Prasad, T. G., Gauns, M., Ramaiah, N., De Souza, S. N., Sardesai, S., and Madhupratap, M. (2002). Why is the Bay of Bengal less productive during summer monsoon compared to the Arabian Sea? *Geophysical Research Letters*, 29(24).

Raja, K. J., Buijsman, M. C., Shriver, J. F., Arbic, B. K., and Siyanbola, O. (2022a). Near-Inertial Wave Energetics Modulated by Background Flows in a Global Model Simulation. *Journal of Physical Oceanography*, 52(5):823–840.

Raja, K. J., Buijsman, M. C., Shriver, J. F., Arbic, B. K., and Siyanbola, O. (2022b). Near-inertial wave energetics modulated by background flows in a global model simulation. *Journal of Physical Oceanography*, 52(5):823–840.

Ralph, E. A. and Niiler, P. P. (1999). Wind-driven currents in the tropical pacific. *Journal of Physical Oceanography*, 29(9):2121 – 2129.

Rasmussen, C. E. and Williams, C. K. I. (2006). *Gaussian Processes for Machine Learning*. MIT Press, Cambridge, MA.

Redi, M. H. (1982). Oceanic Isopycnal Mixing by Coordinate Rotation. *Journal of Physical Oceanography*, 12(10):1154–1158.

Renault, L., Masson, S., Arsouze, T., Madec, G., and McWilliams, J. C. (2020). Recipes for how to force oceanic model dynamics. *Journal of Advances in Modeling Earth Systems*, 12(2):e2019MS001715.

Rimac, A., Storch, J.-S., Eden, C., and Haak, H. (2013). The influence of high-resolution wind stress field on the power input to near-inertial motions in the ocean: The influence of high-resolution winds. *Geophysical Research Letters*, 40.

Rimac, A., Storch, J.-S. V., and Eden, C. (2016). The Total Energy Flux Leaving the Ocean's Mixed Layer. *Journal of Physical Oceanography*, 46(6):1885–1900.

Rogers, C. (1989). Elliptic warm-core theory: the pulsrodon. *Physics Letters A*, 138(6-7):267–273.

Rolland, R., Bouruet-Aubertot, P., Cuypers, Y., Bosse, A., Petrenko, A., Maytie, T., Ponte, A., Barrillon, S., Berta, M., Mourre, B., Pascual, A., Izard, L., Capet, X., Grégori, G., d'Ovidio, F., and Doglioli, A. (2026). Near-Inertial Wave Trapping Inside a Fine-Scale Anticyclonic Eddy During the BioSWOT-Med 2023 Cruise: Turbulence and Energy Flux. *Journal of Geophysical Research: Oceans*, 131(3):e2025JC022984.

Romano, J., Kromrey, J. D., Coraggio, J., and Skowronek, J. (2006). Appropriate statistics for ordinal level data: Should we really be using t-test and Cohen's d for evaluating group differences on the NSSE and other surveys? In *Annual Meeting of the Florida Association of Institutional Research*, Cocoa Beach, Florida.

Rubino, A., Androssov, A., and Dotsenko, S. (2007). Intrinsic dynamics and long-term evolution of a convectively generated oceanic vortex in the greenland sea. *Geophysical research letters*, 34(16).

Rubino, A. and Brandt, P. (2003). Warm-core eddies studied by laboratory experiments and numerical modeling. *Journal of physical oceanography*, 33(2):431–435.

Salehipour, H., Peltier, W., and Mashayek, A. (2015). Turbulent diapycnal mixing in stratified shear flows: the influence of Prandtl number on mixing efficiency and transition at high Reynolds number. *Journal of Fluid Mechanics*, 773:178–223.

Sarma, V., Rao, G., Viswanadham, R., Sherin, C., Salisbury, J., Omand, M., Mahedevan, A., Murty, V., Shroyer, E., Baumgartner, M., and Stafford, K. (2016). Effects of Freshwater

Stratification on Nutrients, Dissolved Oxygen, and Phytoplankton in the Bay of Bengal. *Oceanography*, 29(2):222–231.

Savage, A. C., Waterhouse, A. F., MacKinnon, J. A., Yu, X., Naveira Garabato, A. C., Evans, D. G., Frajka-Williams, E., and Thomas, L. N. (2025). Observations of upper-ocean kinetic energy transfers between near-inertial internal waves and low-frequency dynamics. *Journal of Physical Oceanography*, 55(10):1625–1643.

Schlosser, T. L., Lucas, A. J., Omand, M., and Farrar, J. T. (2026). Monsoons, plumes, and blooms: intraseasonal variability of subsurface primary productivity in the bay of bengal. *Ocean Science*, 22(1):443–458.

Schmitt, R. (2018). The Ocean's Role in Climate. *Oceanography*, 31(2).

Sengupta, D., Bharath Raj, G. N., Ravichandran, M., Sree Lekha, J., and Papa, F. (2016). Near-surface salinity and stratification in the north Bay of Bengal from moored observations. *Geophysical Research Letters*, 43(9):4448–4456.

Service, C. C. M. E. M. (2024). Global ocean gridded l4 sea surface heights and derived variables reprocessed (1993–ongoing) [dataset]. Copernicus Marine Environment Monitoring Service (CMEMS), Marine Data Store. Altimeter satellite gridded sea level anomalies, absolute dynamic topography, and geostrophic currents.

Shakespeare, C. (2016). Curved density fronts: Cyclogeostrophic adjustment and frontogenesis. *Journal of Physical Oceanography*, 46.

Shakespeare, C. J. (2023). Eddy Acceleration and Decay Driven by Internal Tides. *Journal of Physical Oceanography*, 53(12):2787–2796.

Sheehan, P. M. F., Matthews, A. J., Webber, B. G. M., Sanchez-Franks, A., Klingaman, N. P., and Vinayachandran, P. N. (2023). On the influence of the bay of bengal's sea surface temperature gradients on rainfall of the south asian monsoon. *Journal of Climate*, 36(18):6499 – 6513.

Shih, L. H., Koseff, J. R., Ivey, G. N., and Ferziger, J. H. (2005). Parameterization of turbulent fluxes and scales using homogeneous sheared stably stratified turbulence simulations. *Journal of Fluid Mechanics*, 525:193–214.

Shroyer, E., Rudnick, D., Farrar, J. T., Lim, B., Venayagamoorthy, S. K., St. Laurent, L., Garanaik, A., and Moum, J. (2016). Modification of Upper-Ocean Temperature Structure by Subsurface Mixing in the Presence of Strong Salinity Stratification. *Oceanography*, 29(2):62–71.

Shroyer, E., Tandon, A., Sengupta, D., Fernando, H. J. S., Lucas, A. J., Farrar, J. T., Chattopadhyay, R., De Szoeke, S., Flatau, M., Rydbeck, A., Wijesekera, H., McPhaden, M., Seo, H., Subramanian, A., Venkatesan, R., Joseph, J., Ramsundaram, S., Gordon, A. L., Bohman,

S. M., Pérez, J., Simoes-Sousa, I. T., Jayne, S. R., Todd, R. E., Bhat, G. S., Lankhorst, M., Schlosser, T., Adams, K., Jinadasa, S. U. P., Mathur, M., Mohapatra, M., Rama Rao, E. P., Sahai, A. K., Sharma, R., Lee, C., Rainville, L., Cherian, D., Cullen, K., Centurioni, L. R., Hormann, V., MacKinnon, J., Send, U., Anutaliya, A., Waterhouse, A., Black, G. S., Dehart, J. A., Woods, K. M., Creegan, E., Levy, G., Kantha, L. H., and Subrahmanyam, B. (2021). Bay of Bengal Intraseasonal Oscillations and the 2018 Monsoon Onset. *Bulletin of the American Meteorological Society*, 102(10):E1936–E1951.

Smyth, W. D. and Moum, J. N. (2000). Length scales of turbulence in stably stratified mixing layers. *Physics of Fluids*, 12(6):1327–1342.

Søiland, H. and Rossby, T. (2013). On the structure of the lofoten basin eddy. *Journal of Geophysical Research: Oceans*, 118(9):4201–4212.

SWOT (2024). Swot level 2 karin low rate sea surface height data product.

Tarry, D. R., Ruiz, S., Johnston, T. M. S., Poulain, P.-M., Özgökmen, T., Centurioni, L. R., Berta, M., Esposito, G., Farrar, J. T., Mahadevan, A., and Pascual, A. (2022). Drifter observations reveal intense vertical velocity in a surface ocean front. *Geophysical Research Letters*, 49(18):e2022GL098969.

Thomas, L., Moum, J., Qu, L., Hilditch, J., Kunze, E., Rainville, L., and Lee, C. (2024). Blocked Drainpipes and Smoking Chimneys: Discovery of New Near-Inertial Wave Phenomena in Anticyclones. *Oceanography*.

Thomas, L. N., Rainville, L., Asselin, O., Young, W. R., Girton, J., Whalen, C. B., Centurioni, L., and Hormann, V. (2020). Direct observations of near-inertial wave ζ-refraction in a dipole vortex. *Geophysical Research Letters*, 47(21):e2020GL090375.

Thomas, L. N. and Zhai, X. (2021). The lifecycle of surface-generated near-inertial waves. In Meredith, M. and Garabato, A. N., editors, *Ocean Mixing: Drivers, Mechanisms and Impacts*, chapter 5, pages 95–115. Elsevier.

Trenberth, K. E., Large, W. G., and Olson, J. G. (1989). The effective drag coefficient for evaluating wind stress over the oceans. *Journal of Climate*, 2(12):1507 – 1516.

Trodahl, M., Isachsen, P. E., Lilly, J. M., Nilsson, J., and Kristensen, N. M. (2020). The Regeneration of the Lofoten Vortex through Vertical Alignment. *Journal of Physical Oceanography*, 50(9):2689–2711.

Valcke, S. and Verron, J. (1997). Interactions of Baroclinic Isolated Vortices: The Dominant Effect of Shielding. *Journal of Physical Oceanography*, 27(4):524–541.

Vallis, G. K. (2006). *Atmospheric and Oceanic Fluid Dynamics: Fundamentals and Large-scale*

Circulation. Cambridge University Press.

Vanneste, J. (2013). Balance and Spontaneous Wave Generation in Geophysical Flows. *Annual Review of Fluid Mechanics*, 45(1):147–172.

Volkov, D. L., Kubryakov, A. A., and Lumpkin, R. (2015). Formation and variability of the lofoten basin vortex in a high-resolution ocean model. *Deep Sea Research Part I: Oceanographic Research Papers*, 105:142–157.

Von Storch, J. and Lüschow, V. (2023). Wind Power Input to Ocean Near-Inertial Waves Diagnosed From a 5-km Global Coupled Atmosphere-Ocean General Circulation Model. *Journal of Geophysical Research: Oceans*, 128(2):e2022JC019111.

Wagner, G. L. and Young, W. R. (2016). A three-component model for the coupled evolution of near-inertial waves, quasi-geostrophic flow and the near-inertial second harmonic. *Journal of Fluid Mechanics*, 802:806–837.

Wang, Z., Zhang, S., Jin, Y., Jia, Y., Yu, Y., Gao, Y., Yu, X., Li, M., Lin, X., and Wu, L. (2023). Monthly-scale extended predictions using the atmospheric model coupled with a slab ocean. *Geoscientific Model Development*, 16(2):705–717.

Watanabe, M. and Hibiya, T. (2002). Global estimates of the wind-induced energy flux to inertial motions in the surface mixed layer. *Geophysical Research Letters*, 29.

Waterhouse, A. F., Hennon, T., Kunze, E., MacKinnon, J. A., Alford, M. H., Pinkel, R., Simmons, H., Whalen, C. B., Fine, E. C., Klymak, J., and Hummon, J. M. (2022). Global Observations of Rotary-With-Depth Shear Spectra. *Journal of Physical Oceanography*.

Weller, R. A. (1982). The relation of near-inertial motions observed in the mixed layer during the jasin (1978) experiment to the local wind stress and to the quasi-geostrophic flow field. *Journal of Physical Oceanography*, 12(10):1122 – 1136.

Whalen, C. B., MacKinnon, J. A., and Talley, L. D. (2018). Large-scale impacts of the mesoscale environment on mixing from wind-driven internal waves. *Nature Geoscience*, 11(11):842–847.

Whitt, D. B. and Thomas, L. N. (2015). Resonant Generation and Energetics of Wind-Forced Near-Inertial Motions in a Geostrophic Flow. *Journal of Physical Oceanography*, 45(1):181–208.

Wijesekera, H. W., Shroyer, E., Tandon, A., Ravichandran, M., Sengupta, D., Jinadasa, S. U. P., Fernando, H. J. S., Agrawal, N., Arulananthan, K., Bhat, G. S., Baumgartner, M., Buckley, J., Centurioni, L., Conry, P., Farrar, J. T., Gordon, A. L., Hormann, V., Jarosz, E., Jensen, T. G., Johnston, S., Lankhorst, M., Lee, C. M., Leo, L. S., Lozovatsky, I., Lucas, A. J., Mackinnon, J., Mahadevan, A., Nash, J., Omand, M. M., Pham, H., Pinkel, R., Rainville, L., Ramachandran,

S., Rudnick, D. L., Sarkar, S., Send, U., Sharma, R., Simmons, H., Stafford, K. M., St. Laurent, L., Venayagamoorthy, K., Venkatesan, R., Teague, W. J., Wang, D. W., Waterhouse, A. F., Weller, R., and Whalen, C. B. (2016). ASIRI: An Ocean–Atmosphere Initiative for Bay of Bengal. *Bulletin of the American Meteorological Society*, 97(10):1859–1884.

Wijesekera, H. W., Teague, W. J., Hallock, Z. R., Wang, D. W., Luecke, C., Jarosz, E., Jensen, T., Fernando, H., and Jinadasa, S. (2026). Near-inertial wave observations in the Bay of Bengal. *Deep Sea Research Part I: Oceanographic Research Papers*, 229:104686.

Winters, K. B. and D'Asaro, E. A. (1996). Diascalar flux and the rate of fluid mixing. *Journal of Fluid Mechanics*, 317:179–193.

Wunsch, Carl; Ferrari, R. (2004). Vertical mixing, energy, and the general circulation of the oceans. *Annual Review of Fluid Mechanics*, 36(1):281–314.

Xie, J.-H. and Vanneste, J. (2015). A generalised-Lagrangian-mean model of the interactions between near-inertial waves and mean flow. *Journal of Fluid Mechanics*, 774:143–169.

Xu, Y. and Scott, R. B. (2008). Subtleties in forcing eddy resolving ocean models with satellite wind data. *Ocean Modelling*, 20(3):240–251.

Yan, X., Kang, D., Curchitser, E. N., and Pang, C. (2019). Energetics of Eddy–Mean Flow Interactions along the Western Boundary Currents in the North Pacific. *Journal of Physical Oceanography*, 49(3):789–810.

Yi, Y. R. and Koseff, J. R. (2023). Underlying physics of mixing efficiency for shear-forced, stratified turbulence. *Physical Review Fluids*, 8(8):084803.

Young, W. (1986). Elliptical vortices in shallow water. *Journal of Fluid Mechanics*, 171:101–119.

Young, W. and Jelloul, M. B. (1997). Through a geostrophic flow. *Journal of Marine Research*, 55:735–766.

Yu, L.-S., Bosse, A., Fer, I., Orvik, K. A., Bruvik, E. M., Hessevik, I., and Kvalsund, K. (2017). The lofoten basin eddy: Three years of evolution as observed by seagliders. *J. Geophys. Res. Oceans*, 122:6814–6834.

Yu, X., Naveira Garabato, A. C., Vic, C., Gula, J., Savage, A. C., Wang, J., Waterhouse, A. F., and MacKinnon, J. A. (2022). Observed equatorward propagation and chimney effect of near-inertial waves in the midlatitude ocean. *Geophysical Research Letters*, 49(13):e2022GL098522.

Yu, Z., Fan, Y., Metzger, E. J., and Smedstad, O. M. (2018). The wind work input into the global ocean revealed by a 17-year global HYbrid coordinate ocean model reanalysis. *Ocean*

Modelling, 130:29–39.

Zeiden, K. L., Rudnick, D. L., MacKinnon, J. A., Hormann, V., and Centurioni, L. (2022). Vorticity in the wake of palau from lagrangian surface drifters. *Journal of Physical Oceanography*, 52(9):2237 – 2255.

Zhang, S., Qiu, Y., Chen, H., Shen, J., Zhang, J., Cha, J., Qiu, F., and Jing, C. (2021). Estimate of contribution of near-inertial waves to the velocity shear in the Bay of Bengal based on mooring observations from 2013 to 2014. *Acta Oceanologica Sinica*, 40(11):1–10.

Zhang, Y., Gu, J., Chen, S., Hu, J., Sheng, J., and Xing, J. (2025). Sensitivity study of energy transfer between mesoscale eddies and wind-induced near-inertial oscillations. *Ocean Science*, 21(3):1047–1063.

Zhang, Z., Wang, G., Wang, H., and Liu, H. (2024). Three-Dimensional Structure of Oceanic Mesoscale Eddies. *Ocean-Land-Atmosphere Research*, 3:0051.

Zippel, S. F., Farrar, J. T., Zappa, C. J., and Plueddemann, A. J. (2022). Parsing the Kinetic Energy Budget of the Ocean Surface Mixed Layer. *Geophysical Research Letters*, 49(2):e2021GL095920.